



저작자표시-비영리-변경금지 2.0 대한민국

이용자는 아래의 조건을 따르는 경우에 한하여 자유롭게

- 이 저작물을 복제, 배포, 전송, 전시, 공연 및 방송할 수 있습니다.

다음과 같은 조건을 따라야 합니다:



저작자표시. 귀하는 원저작자를 표시하여야 합니다.



비영리. 귀하는 이 저작물을 영리 목적으로 이용할 수 없습니다.



변경금지. 귀하는 이 저작물을 개작, 변형 또는 가공할 수 없습니다.

- 귀하는, 이 저작물의 재이용이나 배포의 경우, 이 저작물에 적용된 이용허락조건을 명확하게 나타내어야 합니다.
- 저작권자로부터 별도의 허가를 받으면 이러한 조건들은 적용되지 않습니다.

저작권법에 따른 이용자의 권리는 위의 내용에 의하여 영향을 받지 않습니다.

이것은 [이용허락규약\(Legal Code\)](#)을 이해하기 쉽게 요약한 것입니다.

[Disclaimer](#)

DOCTOR OF PHILOSOPHY

**Phenomenological Aspects in Phase Transition from
Ferroelectric to Relaxor State in Ternary
 $\text{Bi}_{0.5}\text{Na}_{0.5}\text{TiO}_3\text{-SrTiO}_3\text{-ABO}_3$ Ceramics**

**The Graduate School
of the University of Ulsan
School of Materials Science and Engineering**

HOANG THIEN KHOI NGUYEN

**Phenomenological Aspects in Phase Transition from
Ferroelectric to Relaxor State in Ternary
 $\text{Bi}_{0.5}\text{Na}_{0.5}\text{TiO}_3\text{-SrTiO}_3\text{-ABO}_3$ Ceramics**

Supervisor: Prof. Jae-Shin Lee

A Dissertation

Submitted to

The Graduate School of University of Ulsan

In Partial Fulfillment of the Requirements

for the Degree of

Doctor of Philosophy

by

HOANG THIEN KHOI NGUYEN

School of Materials Science and Engineering

University of Ulsan, Korea

February 2021

**Phenomenological Aspects in Phase Transition from
Ferroelectric to Relaxor State in Ternary
 $\text{Bi}_{0.5}\text{Na}_{0.5}\text{TiO}_3\text{-SrTiO}_3\text{-ABO}_3$ Ceramics**

This certifies that the dissertation
of **Hoang Thien Khoi Nguyen** is approved



Committee Chair Professor **진정호**



Committee Member Professor **신건철**



Committee Member Professor **정순종**



Committee Member Professor **조욱**



Committee Member Professor **이재신**

School of Materials Science and Engineering

University of Ulsan, Korea

February 2021

Acknowledgements

A lot of people have in different ways been helping and supporting me through this research work. First of all, I would like to express my special appreciation and thanks to my supervisor, Prof. Jae-Shin Lee, for giving me the opportunity to work in his group. Thank you for your guidance throughout my research work with excellent advices and sharing your knowledge. Thank you for giving me full freedom to work in the field I was interested in. This research work would not be a success without your continuing guidance and support throughout these years.

Furthermore, I would like to express my gratitude to Dr. Hyung-Su Han for his valuation discussions and trainings, collaboration and supports in writing papers.

I appreciate all my lab members in the Smart Material Lab for their wisdom and encouragement during my stay. It has been a very enjoyable time working with a friendly and professional work environment.

Last but not at least, I am very grateful for the endless love, support, and encouragement from my whole family and friends. Thank you for helping me achieved balance between work and life during my Ph. D journey.

Abstract

Piezoelectric materials play important roles in mechatronics as sensors and actuators in which lead zirconate titanate that contains more than 50 wt% Pb has been primarily used over last decades. However, environmental concern on harmful elements accelerates extensive studies on lead-free piezoelectric materials. Bi-perovskite materials and their solid solutions, especially $\text{Bi}_{0.5}\text{Na}_{0.5}\text{TiO}_3\text{-SrTiO}_3$ (BNT-ST) ceramics attract great attention because of their large strains obtained at low driving electric fields 4 kV/mm when modified with other ABO_3 compounds or impurities. This low field-induced strain is believed to be related with the chemically induced phase transition from ferroelectric to relaxor state in ternary BNT-ST-based ceramics. However, exact understanding about the phase transition in ternary BNT-ST-based ceramics is still lacking. Therefore, there is a necessity for extensive research on the composition-derived phase transition and associated electromechanical properties in the ternary BNT-ST- ABO_3 systems.

In the first stage of the work, with an aim to enhance the low driving field-induced strain in lead-free BNT piezoelectric ceramics, CaTiO_3 and BiAlO_3 are selected as new ABO_3 compounds in two ternary systems $\text{Bi}_{0.5}\text{Na}_{0.5}\text{TiO}_3\text{-CaTiO}_3\text{-SrTiO}_3$ (BNT-CT-ST) and $\text{Bi}_{0.5}\text{Na}_{0.5}\text{TiO}_3\text{-SrTiO}_3\text{-BiAlO}_3$ (BNT-ST-BA). The microstructures, crystal structures, dielectric, ferroelectric and electric field-induced strain behavior of these materials are studied. For the ternary BNT-CT-ST, it was found that a phase transition from nonergodic relaxor to ergodic relaxor was induced by ST modification in BNT-CT ceramics. Consequently, a large electromechanical strain of 0.20% corresponding to high normalized strain d_{33}^* of 667 pm/V was obtained even under 3 kV/mm for 0.71BNT-0.01CT-0.28ST ceramics.

In the work of BNT-ST-BA piezoelectric ceramics, we found that the highest normalized strain d_{33}^* value of 707 pm/V was achieved at a relatively low electric field of 3 kV/mm from 2 mol% BA-modified BNT-ST ceramics. We suggest that the naturally induced nonergodicities in the ergodic relaxor generate internal stress. This induced internal stress is responsible for the excellent strain properties of this material. We believe that the materials synthesized in this study are promising candidates for actuator applications.

Finally, to further expand the understand about the effects and roles of ABO_3 on the composition-induced phase transition from ferroelectric to relaxor state in ternary BNT-ST based ceramics, a comparison of the effect of two kinds modifiers, CaTiO_3 and BaZrO_3 (CT and BZ), with different tolerance factors upon the electromechanical properties of BNT-ST are employed. CT- modification decreases the t-factor of BNT-ST, while BZ-modification increases the t-factor within the investigated doping range 0-4 mol%. The different effects of CT and BZ modification upon the phase transition are clearly observed in the polarization and strain hysteresis loops. The CT-modified specimens maintain strong ferroelectricity

without any abnormal enhancement in the electric field-induced strain. However, the addition of as little as 1mol% BZ induces a transition from a non-ergodic relaxor phase to an ergodic relaxor phase, thus resulting in disruption of the ferroelectric order and the generation of a high field-induced strain. The present authors believe that the substitution of large ions (such as Zr^{4+}) into the B-sites, rather than the A-sites, of the $Bi_{0.5}Na_{0.5}TiO_3$ -based ceramics plays a significant role in the phase transition behavior.

Contents

| | |
|---|------------|
| Acknowledgements | i |
| Abstract | ii |
| List of Figure | vii |
| List of Table..... | xi |
| Chapter 1: Introduction..... | 1 |
| 1.1. Statement of the Problem | 1 |
| 1.2. Research Objectives..... | 3 |
| Chapter 2: Literature Review | 5 |
| 2.1. Basics of Ferroelectrics..... | 5 |
| 2.1.1. Dielectrics | 5 |
| 2.1.1.1. Dielectric Response of Ferroelectrics | 6 |
| 2.1.2. Piezoelectricity and Crystal Symmetry | 7 |
| 2.1.3. An Introduction to the Perovskite Structure..... | 9 |
| 2.1.4. Ferroelectricity and Antiferroelectricity..... | 11 |
| 2.1.4.1. Polarization Switching and Hysteresis Loops | 12 |
| 2.2. Relaxor ferroelectrics | 13 |
| 2.2.1. Phenomenological signatures of relaxors | 13 |
| 2.2.2. Models describing relaxation mechanisms | 17 |
| 2.2.2.1. Compositional heterogeneity/fluctuations and diffused phase transition | 17 |
| 2.2.2.2. Superparaelectric model..... | 18 |
| 2.2.2.3. Dipolar glass model | 18 |
| 2.2.2.4. Random field model..... | 19 |
| 2.3. Phase transition and phase boundary | 20 |
| 2.3.1. Phase boundaries in lead-based piezoelectric materials..... | 21 |
| 2.3.1.1. Pb(Zr, Ti)O ₃ piezoelectric compositions..... | 21 |

| | | |
|-------------------|---|-----------|
| 2.3.1.2. | Pb(Mg, Nb)O ₃ piezoelectric compositions | 22 |
| 2.3.2. | Phase boundary in Bi _{0.5} Na _{0.5} TiO ₃ -based ceramics | 23 |
| 2.3.2.1. | Bi _{0.5} Na _{0.5} TiO ₃ -BaTiO ₃ (BNT-BT) solid solutions | 24 |
| 2.3.2.2. | Bi _{0.5} Na _{0.5} TiO ₃ -Bi _{0.5} K _{0.5} TiO ₃ (BNT-BKT) solid solutions | 26 |
| 2.3.2.3. | Bi _{0.5} Na _{0.5} TiO ₃ -SrTiO ₃ (BNT-ST) solid solutions..... | 28 |
| Chapter 3: | Experimental Procedure and Characterization | 30 |
| 3.1. | Experimental Procedure..... | 30 |
| 3.1.1. | Compositions | 30 |
| 3.1.2. | Raw materials..... | 30 |
| 3.1.3. | Mixing and milling..... | 31 |
| 3.1.4. | Calcinations..... | 31 |
| 3.1.5. | Pellet preparation | 31 |
| 3.1.6. | Sintering | 32 |
| 3.1.7. | Lapping and polishing..... | 32 |
| 3.1.8. | Electrode application..... | 32 |
| 3.1.9. | Poling | 32 |
| 3.2. | Structural characterization | 33 |
| 3.2.1. | Density Measurement | 33 |
| 3.2.2. | X-Ray Diffraction Analysis | 33 |
| 3.2.3. | Microstructural analysis | 34 |
| 3.3. | Electrical characterizations..... | 35 |
| 3.3.1. | Dielectric properties | 35 |
| 3.3.2. | Piezoelectric coefficient (<i>d</i> ₃₃)..... | 36 |
| 3.3.3. | Ferroelectric properties | 36 |
| 3.3.4. | Electric field-induced strain measurement..... | 36 |
| Chapter 4: | Result and Discussion | 37 |

| | |
|---|-------------------------------------|
| 4.1. Effect of SrTiO₃ Modification on Dielectric, Phase Transition and Piezoelectric Properties of Lead-Free Bi_{0.5}Na_{0.5}TiO₃-CaTiO₃-SrTiO₃ Piezoelectric Ceramics | 37 |
| 4.1.1. Introduction..... | 37 |
| 4.1.2. Experimental Procedure..... | 38 |
| 4.1.3. Results and Discussion..... | 39 |
| 4.1.4. Summary | 47 |
| 4.2. Large Electric Field-induced Strain Response under a Low Electric Field in Lead-free Bi_{1/2}Na_{1/2}TiO₃-SrTiO₃-BiAlO₃ Ternary Piezoelectric Ceramics | 48 |
| 4.2.1. Introduction..... | 48 |
| 4.2.2. Experiment procedure | 50 |
| 4.2.3. Result and discussion | 51 |
| 4.2.4. Summary | 59 |
| 4.3. Comparing the Electromechanical Properties of CaTiO₃- and BaZrO₃-Modified Bi_{0.5}Na_{0.5}TiO₃-SrTiO₃ Ceramics | 60 |
| 4.3.1. Introduction..... | 60 |
| 4.3.2. Experimental details..... | 61 |
| 4.3.3. Results and Discussion..... | 63 |
| 4.3.4. Summary | 71 |
| Chapter 5: Conclusions and outlook..... | Error! Bookmark not defined. |
| References..... | 78 |
| List of Publications | 86 |

List of Figure

| | |
|--|----|
| Figure 2.1: Schematic temperature dependence of the real dielectric permittivity and spontaneous polarization (PS) for (a) first-order ferroelectrics, (b) ferroelectrics with a diffuse phase transition and (c) typical relaxors [29]. | 7 |
| Figure 2.2: Symmetry hierarchy for piezoelectricity. | 9 |
| Figure 2.3: (a) Ideal perovskite structure with chemical formula ABO_3 and (b) three dimensional network of corner shearing octahedral of O-2 ions [35]. | 11 |
| Figure 2.4: (a) Polarization versus large electric field and (b) bipolar strain in field direction in a large electric field [43]. | 13 |
| Figure 2.5: Exemplary permittivity-temperature curve of a relaxor ferroelectric measured at various frequencies. At the burn temperature T_B , polar nanoregions are forming during cooling, whereas the motion of these regions freezes at the Vogel-Fulcher temperature. | 15 |
| Figure 2.6: Temperature-dependent permittivity of a PMN-PT single during heating. The samples were electrically poled prior to each measurement. The anomalies in both curves mark the ferroelectric-to-relaxor phase transition temperature [143]. | 16 |
| Figure 2.7: The diffuse phase transition model insulation[49]. | 17 |
| Figure 2.8: : A schematic illustration showing how isovalent doping influences the quenched random electric fields that disrupt a long-range ferroelectric order [49]. | 19 |
| Figure 2.9: Cross-section of the Gibbs free energy for 90/10 and 60/40 $Pb(Zr_{1-x}Ti_x)O_3$ along $[M_B]$ path [89]. | 20 |
| Figure 2.10: (a) Phase diagram of $(1-x)PbZrO_3-xPbTiO_3$ and (b) composition-dependent piezoelectric properties of $(1-x)PbZrO_3-xPbTiO_3$ ceramics [89]. | 21 |
| Figure 2.11: Temperature versus composition phase diagram of PMN-PT (C: cubic, R: rhombohedral, M: monoclinic, T: tetragonal) [101]. | 22 |

Figure 2.12: Phase diagram of BNT–BT solid solution, ($F\alpha$: ferroelectric rhombohedral phase, $F\beta$: ferroelectric tetragonal phase, AF: antiferroelectric phase, P: paraelectric phase) [19]. 24

Figure 2.13: Binary phase diagram of the BNT-ST system from 0 mol% to 40 mol% ST. The symbols \square , \circ , and \triangle corresponds to T_d , T_{R-T} and T_m , respectively. Open symbols were obtained from dielectric measurements, while solid symbols from Raman spectroscopy analysis [149]. 29

Figure 4.1: Linear shrinkage and relative density values of BNT–CT–100xST ceramics as a function of ST content 40

Figure 4.2: FE–SEM images of polished and thermally etched BNT–CT–100xST ceramics, (a) $x = 0.22$, (b) $x = 0.24$, (c) $x = 0.26$, (d) $x = 0.28$, (e) $x = 0.30$ and (f) the average grain size as a function of ST content 41

Figure 4.3: X–ray diffraction patterns of BNT–CT–100xST ceramics as a function of ST content, (a) 20–60°, (b) 39.5–41.5°, and (c) 46.5–47.5° 42

Figure 4.4: Temperature–dependent dielectric constant (ϵ_r) and dielectric loss ($\tan \delta$) for the poled (top) and unpoled (bottom) BNT–CT–100xST ceramics as a function of ST content, (a) and (f) $x = 0.22$, (b) and (g) $x = 0.24$, (c) and (h) $x = 0.26$, (d) and (i) $x = 0.28$, (e) and (j) $x = 0.30$ 42

Figure 4.5: Polarization (top) and bipolar strain curves (bottom) for BNT–CT–100xST ceramics as a function of ST content, (a) and (f) $x = 0.22$, (b) and (g) $x = 0.24$, (c) and (h) $x = 0.26$, (d) and (i) $x = 0.28$, (e) and (j) $x = 0.30$ 44

Figure 4.6: Variation of (a) E_c , P_r , and (b) S_{max} , S_{neg} of BNT–CT–100xST ceramics as a function of ST content..... 44

Figure 4.7: Unipolar strain curves for BNT–CT–100xST ceramics as a function of ST content. 45

Figure 4.8 FE-SEM images of the polished and thermally etched surfaces of (a) BNT–ST–0BA, (b) BNT–ST–1BA, (c) BNT–ST–2BA, and (d) BNT–ST–3BA ceramics. Changes to (e) linear shrinkage and relative density and (f) the average grain size of the BNT–ST–100xBA ceramics as a function of BA content..... 51

Figure 4.9: X-ray diffraction (XRD) patterns of BNT–ST–100xBA ceramics as a function of BA content in the 2θ ranges of (a) 30–60°, (b) 39.5–40.5° and (c) 45.8–47.2° 52

Figure 4.10: Temperature dependence of dielectric constant (ϵ_r) and dielectric loss ($\tan \delta$) for the poled (top) and unpoled (bottom) for BNT–ST–100xBA ceramics, (a) and (e) $x = 0$, (b) and (f) $x = 0.01$, (c) and (g) $x = 0.02$, (d) and (h) $x = 0.03$ 53

Figure 4.11: Electric field–induced (top) polarization hysteresis (P – E) and (bottom) bipolar strain (S – E) curves for BNT–ST–100xBA ceramics, (a) and (e) $x = 0$, (b) and (f) $x = 0.01$, (c) and (g) $x = 0.02$, (d) and (h) $x = 0.03$. Extracted (i) P_{\max} , P_r , E_C and (j) S_{\max} , S_{neg} parameters for BNT–ST–100xBA ceramics as a function of BA content..... 53

Figure 4.12: Unipolar strain curves for BNT–ST–100xBA ceramics at different applied electric field strengths of 3, 4 and 5 kV/mm, (a), (e), and (i) $x = 0$, (b), (f), and (j) $x = 0.01$, (c), (g), and (k) $x = 0.02$, (d), (h) and (l) $x = 0.03$ 54

Figure 4.13: (a) S_{\max} values for BNT–ST–100xBA ceramics as a function of applied electric field and (b) d_{33}^* values for BNT–ST–100xBA ceramics as a function of BA content..... 55

Figure 4.14: Comparison of d_{33}^* values against maximum applied electric fields (E_{\max}) between lead–based, lead–free BNT–based, and ferroelectric/relaxor composites. 57

Figure 4.15: Schematic strain mechanisms for three different states of (a) BNT–ST–0BA, (b) BNT–ST–2BA, and (c) BNT–ST–3BA ceramics: stages (i) corresponds to the virgin (or initial) state, stage (ii) corresponds to the application of a significant electric field, and stage (iii) corresponds to removal of the electric field. 58

Figure 4.16: X-ray diffraction patterns of (a)–(c) CT100x with $x = 0.00$ – 0.04 and (d)–(f) BZ100y with $y = 0.00$ – 0.04 ceramics in the 2θ range from 20 to 60°..... 63

Figure 4.17: Polished and thermally etched surface images of (a)–(e) CT100x with $x = 0.00$ – 0.04 and (f)–(i) BZ100y with $y = 0.01$ – 0.04 , and (j) the average grain size as the function of end-member modification. 64

Figure 4.18: Temperature-dependent dielectric constant and dielectric loss for the poled and unpoled of (a)-(e) CT100 x with $x = 0.00-0.04$ and (f)-(i) BZ100 y with $y = 0.01-0.04$ 66

Figure 4.19: Polarization hysteresis loops and switching current curves at 6 kV/mm for (a)-(e) CT100 x with $x = 0.00-0.04$ and (f)-(i) BZ100 y with $y = 0.01-0.04$ 66

Figure 4.20: Effects of CT- and BZ-modifier content on (a) the maximum polarization, (b) the remnant polarization, (c) the coercive field, and (d) the poling/depoling field..... 67

Figure 4.21: Bipolar strain curves at 6 kV/mm for (a)-(e) CT100 x with $x=0.00-0.004$ and (f)-(i) BZ100 y with $y=0.01-0.04$ ceramics..... 68

Figure 4.22: Effects of CT- and BZ-doping level on (a) the maximum strain, and (b) the negative strain of the materials..... 69

Figure 4.23: (a) Piezoelectric constant (d_{33}) and (b) normalized strain (S_{max}/E_{max}) as the function of CT and BZ content..... 70

Figure 5.1: The phase diagram of the BNT-ST-CT (left) and BNT-ST-BA (right) ternary system in the range of 0.22-0.30 mol ST content. 73

Figure 5.2: Compositional dependence of (a) piezoelectric constant (d_{33}) and (b) normalized strain (d_{33}^*) of BNT-ST-CT, BNT-ST-BZ and BNT-ST-BA ceramics..... 74

List of Table

| | |
|---|----|
| Table 2.1: Electrical properties of BNT-BT ceramics | 25 |
| Table 2.2: Electrical properties of BNT-BKT ceramics | 27 |
| Table 2.3: Electrical properties of BNKT ceramics with ion substitution..... | 27 |
| Table 3.1: Raw materials used in the synthesis of ternary BNT-ST-based ceramics | 30 |
| Table 4.1: Comparison of normalized strains d_{33}^* (S_{\max}/E_{\max}) between this study and other BNT-based lead-free piezoceramics | 46 |
| Table 5.1: Quantitative evaluation of differences in radii between ion modification and matrix of $BaZrO_3$ and $BiAlO_3$ endmembers | 75 |

Chapter 1: Introduction

Piezoelectric materials with perovskite structure have attracted a lot of attention for many reasons. This explicit category of materials has been the main focus of current analysis as a result of its easy basic crystal structure facilitates in understanding the relationship between structural modification and physical properties. Moreover, the perovskite electricity materials area unit often become ferroelectric that ensures economical mechanical device transformation of energy and signal with high electricity constant. most significantly, not like different crystal structures, perovskites do not have a compact atomic number 8 framework, and this provides nice flexibility for chemical substitution. As a results of the variable chemical compositions and crystal symmetries, several physical properties will be tailored consistent with the precise desires of the assorted applications [1, 2].

1.1. Statement of the Problem

Piezoelectric ceramic materials are widely used in modern industry to transform electrical signals into mechanical strain and vice versa; this coupling nature enables piezoelectric materials to be applied in electromechanical systems as both actuators and sensors. The piezoelectric devices are used in many current applications such as accelerometers, automotive fuel injection, piezoelectric transformers, vibration control, ultrasound sensors and generators and inkjet printers amongst many others [3]. Lead zirconate titanate (PZT) ceramics have been the dominant piezoelectric material in these applications for a long time because of its superior dielectric and piezoelectric properties [4]. In particular, its large piezoelectric response has made PZT one of the most widely used materials for electromechanical applications. However, PZT is becoming increasingly unacceptable because of global concerns regarding its toxicity as it contains more than 60 weight percent of lead. The use of volatile starting materials (PbO or Pb₃O₄) during processing causes an accumulation of lead in the environment. Very low concentrations of lead or lead derivatives can cause serious hazards to the brain, nervous system, kidney and blood. In addition, recycling and waste disposal of lead- containing devices could be hazardous for the health and environment. As a result, the European Union (EU) proceed the “Restriction of the use of certain Hazardous Substances in electrical and electronic equipment” (RoHS) and “Waste Electrical and Electronic Equipment” (WEEE) in 2003 [5, 6]. The WEEE regulates the disposal, reuse and recycling of the mentioned equipment. While the RoHS is an important requirement to assure that the equipment can be accomplished safely without hazarding the environment or people’s health. Lead as well as other toxic substances such as cadmium, mercury, the polybrominated diphenyl ethers flame-retardants polybrominated biphenyls have been

identified as a major risk during recycling, disposal, or even improper use. Therefore, as of 1 July 2006, any product placed on the open market cannot exceed 0.1% by weight of any of these substances, except cadmium, where the limit is even less than 0.01% by weight. There are activities to establish similar regulations in countries all over the world. In Asia, South Korea, Japan and China have different approaches for establishing RoHS-like regulations [7]. In South Korea regulations equivalent to the EU legislation with respect to the restricted substances, maximum concentration values, and exemptions are already enforced [8]. In China and Japan labeling of electronic devices is required if the values for the six EU-defined hazardous substances exceed the corresponding EU maximum concentrations [9, 10].

Although piezoelectric materials are currently exempted from these regulations/directives due to the difficulty in finding a suitable substitution which can compare with lead, a global lead-free policy is foreseeable in the future. Before 1990, research activities were mainly aimed at finding systems with better characteristics than the PZT system. However, this is not for the purpose of protecting the environment but merely to seek systems with improved properties over PZT. Since about 1990, research has mostly directed towards the development of lead free piezoceramics, which would compete and replace lead-based materials due to before-mentioned legislation. Recently, the lead-free piezoelectric ceramics take much attention, especially bismuth-based piezoelectric ceramic. Bi^{3+} is a preferred element to replace Pb^{2+} because of its same electron structure with Pb^{2+} . The exhibition of good piezoelectric properties in Bi-based compounds has been reasoned as a consequence of the presence of Bi^{3+} stereo-chemically active lone-pair of electrons [11]. $\text{Bi}_{0.5}\text{Na}_{0.5}\text{TiO}_3$ (BNT) is considered one of the most promising lead-free relaxor materials and a potential candidate to replace lead-based materials. BNT has been widely examined and investigated in recent years because of its structural varieties [12-14], beside the materials possess interesting dielectric, piezoelectric and electromechanical properties [15-17]. Nonetheless, the problematic poling, low resistivity and high recorded coercive field are the downsides of unmodified BNT ceramics. Moreover, in comparison with lead-based materials, the electromechanical behavior of BNT is not suitable for commercialize. In order to obtain the materials with better performance, the doping modification of BNT ceramics have been investigated for a long time. Zhang et al. found that $0.92\text{Bi}_{0.5}\text{Na}_{0.5}\text{TiO}_3-0.06\text{BaTiO}_3-0.02\text{K}_{0.5}\text{Na}_{0.5}\text{NbO}_3$ (92BNT-6BT-2KNN) ceramic had an ultrahigh strain response up to 0.45% under the field of 80 kV/cm, which is indeed higher than the values obtained by the PZT ferroelectric ceramics [18]. It is generally believed that this giant strain is associated with the reversible electric field-induced phase transition from an ergodic relaxor to a ferroelectric state [19]. However, it is a crucial obstacle that such giant strain properties in the incipient BNT-based piezoceramics are only induced by a relatively high electric field, which restrict the functional application of these lead-free piezoceramics [7].

Currently, the solid solution $(1-x)\text{BNT}-x\text{SrTiO}_3$ (BNT-ST) is considered to be an important binary system among BNT-based ceramics, which was firstly reported by K. Sakata and Y. Masuda [20]. The most outstanding character of this material is that the required driving electric field to achieve giant strain is much lower than those of other BNT-based ceramics. It has been reported that the BNT-ST forms a rhombohedral ferroelectric and pseudo cubic morphotropic phase boundary (MPB) at $x = 0.25-0.28$ with a large normalized strain ($S_{\text{max}}/E_{\text{max}}$) of about 600 pm/V under a relatively low field of 4 kV [21-24]. Considering the favorable properties of BNT-ST binary solid solution, few recent studies have been suggested that exploring ternary systems can result in discovering high performance piezoelectric in BNT-ST ceramics. Through this approach, a maximum strain of 0.27% at 4 kV/mm for BNT-ST- AgNbO_3 [25], a high strain of 0.24% with 4 kV/mm at low sintering temperature for BNT-ST- LiNbO_3 [26], and a large strain of 0.239% under ultra-low driving field of 3 kV/mm for BNT-ST- KTaO_3 [27] were obtained. However, unlike binary compositions, uncovering the phase transition in a ternary system is exceedingly more difficult as the number of possible end-member combinations greatly increases, leading to a thorough understanding of phase transition from ferroelectric to relaxor in ternary BNT-ST- ABO_3 ceramics still lacking. Therefore, research on the ternary BNT-ST based ceramics is believed to be its early stage and there are still many rooms to be investigated and examined.

1.2. Research Objectives

In recent years, there has been a considerable and renewed interest in understanding the relationship between structure and properties in ferroelectric solid solutions and this has been further stimulated by the quest for lead free alternatives to lead based systems with equally high actuating performances. In this perspective, detailed structural studies play an important role both in understanding phase transition and the subsequent enhancement of electric-field induced strain properties. Therefore, the aim of this thesis is to demonstrate the importance of roles of various ABO_3 endmembers on the phase transition and low-field induced strain properties of ternary BNT-ST- ABO_3 ceramics. In so-doing, firstly, the detailed structural studies of $\text{Bi}_{0.5}\text{Na}_{0.5}\text{TiO}_3\text{-CaTiO}_3\text{-SrTiO}_3$, and $\text{Bi}_{0.5}\text{Na}_{0.5}\text{TiO}_3\text{-SrTiO}_3\text{-BiAlO}_3$ ternary ceramics systems are performed. The entire systems have been studied over a range of compositions and compositionally driven structural phase transitions have been studied. The composition-dependent dielectric, piezoelectric and low-driving field-induced strain properties are characterized and discussed in detail with regards to their compositions. Finally, to further understand the phenomenological aspects of the ferroelectric to relaxor phase transition process in the ternary BNT-ST systems, the present work compares the effect of CaTiO_3 and BaZrO_3 modification upon the crystal structure, dielectric, ferroelectric and field-induced strain properties of the two ternary BNT-ST- CaTiO_3 and BNT-ST- BaZrO_3 ceramics. These findings are believed

to significantly contribute to our insight into phase transformation process from ferroelectric to relaxor ferroelectric in the ternary BNT-based ceramics.

Chapter 2: Literature Review

2.1. Basics of Ferroelectrics

This chapter provides the fundamentals of dielectrics and ferroelectrics and their connected properties applicable to the objectives of this analysis. In resultant section, a literature survey is given presenting the updated information on unleaded bismuth-based electricity.

2.1.1. Dielectrics

Dielectrics are insulating materials that have virtually no free charge carriers. When an insulating dielectric material is placed under an electric field, there is no long-range charge transport but only a local re-arrangement of charge such that the material acquires a dipole moment. This phenomenon is known as polarization. Under an external electric field (E) the electric displacement vector D can be written as:

$$D = \varepsilon E = \varepsilon_0 E + P \quad 2.1$$

Where D is dielectric displacement, ε is the dielectric permittivity (or dielectric constant), E is applied electric field, and P is called the polarization (dipole moment per unit volume) which can be expressed as:

$$P = \chi_e \varepsilon_0 E \quad 2.2$$

Where χ_e is the electric susceptibility and ε_0 is the free space permittivity ($8.85 \times 10^{12} \text{ C}^2/\text{Nm}^2$). It follows from the above two equations:

$$D = \varepsilon_0 E + \chi_e \varepsilon_0 E = \varepsilon_0 (1 + \chi_e) E \quad 2.3$$

$$\varepsilon = \varepsilon_0 (1 + \chi_e) \quad 2.4$$

$$\frac{\varepsilon}{\varepsilon_0} = (1 + \chi_e) = \varepsilon_r \quad 2.5$$

Where ε_r is called the relative permittivity.

In an alternating electric field, the dielectric permittivity or relative permittivity is a complex quantity, and it is written as:

$$\varepsilon_r = \varepsilon' + i\varepsilon'' \quad 2.6$$

Where the real part ε' is mentioned as real permittivity and ε'' is the imaginary part, which is concerned to the energy loss in the system. The dielectric constant strongly depends on the defects (imperfection) and

the chemical structure of the materials. The dielectric response function of a system highly depends on the frequency and temperature because of the various polarization mechanisms and as a consequence relaxation and resonance effects in a dielectric material occur as a function of frequency. Each type of polarization requires time to perform this is why the degree of the overall polarization depends on the time variation of the electric field. The following four major polarization mechanisms are usually seen [28]:

(1). Electronic (atomic) polarization: This occurs as a result of the distorted electron cloud in response to an electric field and the atom temporarily acts as a dipole. The Electronic polarization is observed in all materials. The response time of atomic polarization is very short and this contributes at high frequencies, up to frequencies on the order of $\sim 10^{15}$ Hz.

(2). Ionic polarization: In ionic polarization the constituent cations and anions of a crystal are physically displaced by the external field. The polarization has an average response time of ~ 1 ps. Ionic polarization contributes to the measured permittivity up to frequencies of $\sim 10^{12}$ Hz.

(3). Molecular (dipolar) polarization: Dipolar polarization existing in materials possesses permanent dipoles. When an electric field is applied to such a material, the permanent dipoles tend to align along the electric field direction, resulting in a finite net polarization. It is a relatively slow process and contributes only at lower frequencies ($< 10^8$ Hz).

(4). Space charge polarization: This phenomenon is the process of the accumulation of charges in multiphase or inhomogeneous dielectrics. Space charge polarization is relatively slow, and typically responds only at lower frequencies ($< 10^4$ Hz).

2.1.1.1. Dielectric Response of Ferroelectrics

Ferroelectric materials exhibit high dielectric constants (up to $\sim 10^5$ under certain conditions) because of the large spontaneous polarization. Ferroelectric materials can be classified into two categories with respect to the origin of the polarization [29]: one is the displacive type ferroelectric, in which the polarization occurs due to the small displacement of the cations with respect to the anions, and the other is the order-disorder type ferroelectrics, in which the polarization occurs because of the ordering of the ions (i.e., permanent dipole moments align). Ionic crystals, such as PbTiO_3 and BaTiO_3 are generally displacive type ferroelectrics, and crystals containing H-bonds, such as potassium dihydrogen phosphate (KH_2PO_4) are usually order-disorder type ferroelectrics. The spontaneous polarization disappears above a certain temperature which is called the Curie point. The dielectric constant increases rapidly with the temperature and reaches the maximum near the Curie point. The high temperature phase is called the

paraelectric phase and the lower temperature phase is called the ferroelectric phase. In the case of paraelectric phase, the dielectric constant commonly obeys the Curie-Weiss law:

$$\epsilon' = \frac{C}{T-T_0} \quad 2.7$$

Where C is known as the Curie constant and T_0 is a characteristic temperature which is equal to the Curie temperature for 2nd-order phase transitions.

The typical temperature-dependent dielectric constants for ferroelectric materials are depicted in Figure 2.1. Based on their response as a function of temperature and frequency it is possible to classify the ferroelectric materials into three major categories: (a) normal ferroelectrics (BaTiO_3 , PbTiO_3), (b) ferroelectrics with a diffuse transition ($\text{BaTi}_{1-x}\text{Sn}_{1-x}\text{O}_3$) and (c) relaxors ($\text{PbSc}_{1/2}\text{Nb}_{1/2}\text{O}_3$, $\text{PbMg}_{1/3}\text{Nb}_{2/3}\text{O}_3$) [30, 31].

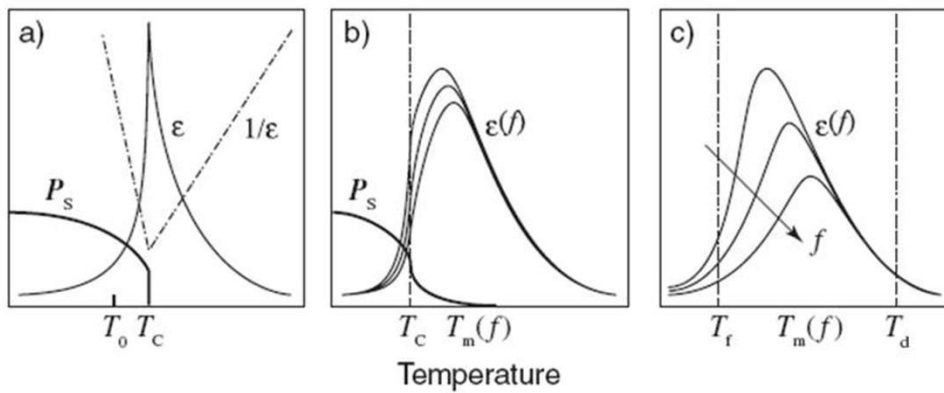


Figure 2.1: Schematic temperature dependence of the real dielectric permittivity and spontaneous polarization (PS) for (a) first-order ferroelectrics, (b) ferroelectrics with a diffuse phase transition and (c) typical relaxors [29].

2.1.2. Piezoelectricity and Crystal Symmetry

In 1880, Jacques Curie and Pierre Curie first time exposed the piezoelectricity phenomenon [32]. The term refers to the generation of an electric moment in response to mechanical stress and vice versa. Mathematically, it can be written as

$$P_i = d_{ijk}\sigma_{jk} \quad 2.8$$

$$S_{ij} = d_{kij}E_k \quad 2.9$$

Equation (2.8) describes direct piezoelectricity, where P gives the magnitude of the electric moment per unit volume or polarization charge per unit area, T is the applied stress and d is called the piezoelectric coefficient which is related to crystal structure. Equation (2.9) refers to converse piezoelectricity, where S is the induced strain in response to the external electric field E . The piezoelectric coefficient, d , is numerically identical for both direct and converse piezoelectric effects [4]:

$$d = \frac{P}{\sigma} = \frac{S}{E} \quad 2.10$$

A simplified notation is often used where one of the subscripts is dropped, and the piezoelectric coefficient becomes d_{ij} . Equations 2.8 and 2.9 then becomes:

$$P_i = d_{ij}\sigma_j \quad 2.11$$

$$S_i = d_{ij}E_j \quad 2.12$$

The d coefficients are usually expressed as ($\times 10^{-12}$) C/N for the direct effect and ($\times 10^{-12}$) m/V for the converse effect. The classes of materials that exhibit such properties are called piezoelectric materials and because of their unique ability to couple electrical and mechanical displacements they are widely used as sensors and actuators.

The structure and symmetry of a material plays a decisive role in piezoelectricity. The necessary crystallographic requirement for a material to show piezoelectricity is that it should not have a center of symmetry. As shown in Figure 2.2, in the total of the 32 crystallographic point groups, 21 groups are non-centrosymmetric, which can show piezoelectricity, while 11 groups are centrosymmetric [33, 34]. In addition, the combined symmetry elements in point group 432 do not allow the piezoelectric effect. Thus, there are 20 as non-centrosymmetric piezoelectric point groups [4]. Ten out of these 20-point groups, polarization can be induced by internal stress. The remaining 10 groups can show a spontaneous polarization. These 10 groups are the polar groups, and materials with these point group symmetries can potentially demonstrate piezoelectric as well as pyroelectric effects. Out of these 10 groups, there is a subgroup exhibiting spontaneous polarization and reversible polarization, which can display all three effects. (ferroelectric, piezoelectric and pyroelectric). It should be obvious that all ferroelectric materials are also pyroelectric and therefore piezoelectric as well but not all pyroelectric materials show ferroelectricity.

The 32-point groups are subdivision of seven basic crystal systems, which are based on the degree of symmetry. There are seven basic crystal systems are triclinic, monoclinic, orthorhombic, tetragonal, trigonal (rhombohedral), hexagonal and cubic, which is arranged in ascending order of symmetry.

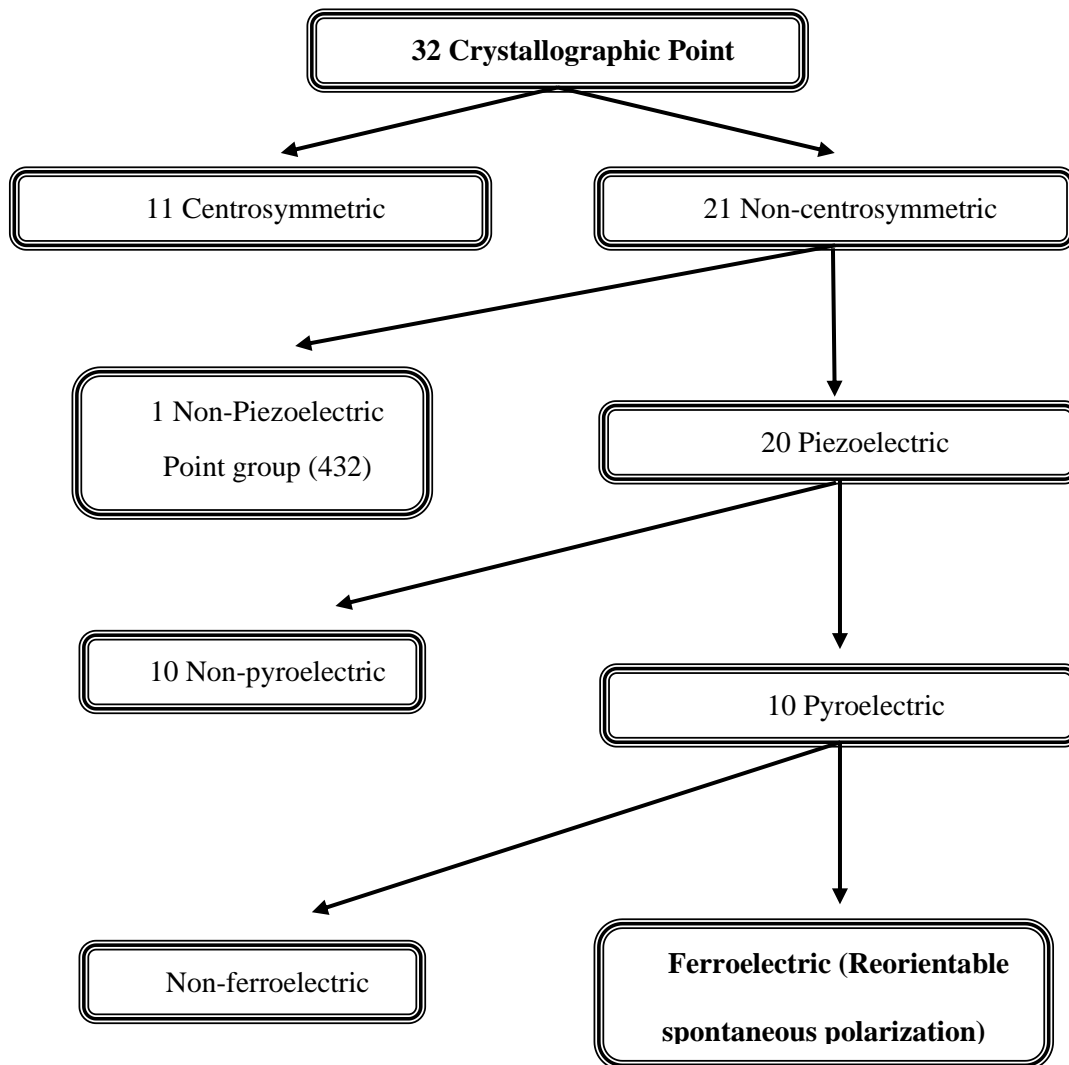


Figure 2.2: Symmetry hierarchy for piezoelectricity.

2.1.3. An Introduction to the Perovskite Structure

The term “perovskite” assigns to a large family of crystals with structures based on that of the mineral CaTiO_3 , which is known as perovskite, which was based on the name of a Russian mineralogist Count Lev Aleksevich von Perovski (1792-1856). The perovskite structure, represented as ABX_3 , is one of the most versatile crystal structures. The ideal perovskite structure has cubic symmetry. The A site is in 12-fold coordination with large cations, the B site is in 6-fold coordination with smaller cations, and the X sites are 6-fold coordinated anions. The crystal structure is shown in Figure 2.3. The choices of A & B are very broad. Examples of common A-site cations are: Ca^{2+} , Sr^{2+} , Na^+ , K^+ , Pb^{2+} , Ba^{2+} , La^{3+} and Bi^{3+} ; examples of common B-site cations are : Mg^{2+} , Zn^{2+} , Sc^{3+} , Al^{3+} , Fe^{3+} , Zr^{4+} , Sn^{4+} , Ti^{4+} , Ta^{5+} and Nb^{5+} and X is typically

either an oxygen or a fluorine ion. In other words, the perovskite structure can tolerate a wide range of compositional variation. The simple ternary perovskite can be divided into $A^{1+}B^{5+}O_3$, $A^{2+}B^{4+}O_3$, $A^{3+}B^{3+}O_3$ types and oxygen and cation deficient phases. Most perovskite-type ferroelectrics are compounds with $A^{2+}B^{4+}O_3$ or $A^{1+}B^{5+}O_3$ -type formula [35].

Not all compounds with the formula ABO_3 have a perovskite structure. Goldschmidt (1926) proposed a simple geometrical relationship between cations and anions which can be used to describe the stability of the perovskite structure [36]. According to Goldschmidt, the geometrical requirement for the formation of the perovskite structure is that the ionic radii r_A , r_B and r_O of the A, B and the O ions must satisfy the following relationship:

$$t = (r_A + r_O) / \sqrt{2}(r_B + r_O) \quad 2.13$$

Where “t” is called the tolerance factor. The ionic radii refer to those reported by Shannon [37]. The relationship phenomenologically describes the range of relative sizes of A and B cations for which the perovskite structure is stable. The indication of a tolerance factor is how far an atom can migrate from the ideal packing position and still maintain the perovskite structure. The adjustment in t values can induce the structural modification such as distortion, rotation, tilt of the octahedra [1]. These structure factors subsequently involve the electrical properties. Generally, the perovskite structure is said to be stable if t lies in the range $0.880 < t < 1.090$ [38]. It has been known that perovskites with the tolerance factor higher than one ($t > 1.0$) normally favors tetragonal distortion whereas tolerance factor less than one ($t < 1.0$) favors rhombohedral or monoclinic or orthorhombic symmetry. For ideal cubic perovskite structure, the tolerance factor is equal to 1. $SrTiO_3$ is an example of material having a cubic perovskite structure at room temperature.

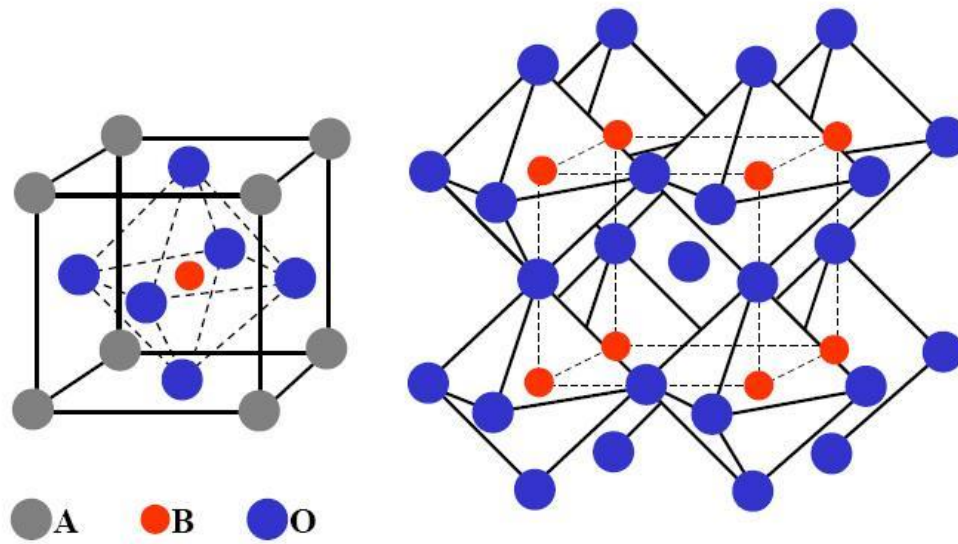


Figure 2.3: (a) Ideal perovskite structure with chemical formula ABO_3 and (b) three dimensional network of corner shearing octahedral of O-2 ions [35].

2.1.4. Ferroelectricity and Antiferroelectricity

Ferroelectricity is characterized by a spontaneous polarization in the absence of an electric field. The spontaneous polarization can be switched by applying an external electric field [39]. Materials exhibit this property are called ferroelectric materials. In ferroelectric materials, the unit cell exhibits a net permanent dipole moment. This dipole moment does not immediately translate into a macroscopic polarization of the material due to the distribution of the randomly oriented dipole moments in the case of polycrystalline ceramics. In polycrystalline materials but also in single crystals, the orientation distribution of the dipole moments is not completely random on the unit cell level but organized in groups called domains. Domains are areas where the dipole direction of individual adjacent unit cells is the same. These domains have a net non- zero polarization. A large number of domains arrange in such a way within the material that the macroscopic polarization of the material is zero. The interface between two domains is called domain wall. In ferroelectric material, the width of domain walls is very small, the scale of a few nm or less [40]. For example, in a tetragonal ferroelectric phase, the angles between two domains are either 90° or 180° , whereas they are 71° , 109° , or 180° in a rhombohedral phase. The walls separated by oppositely oriented polarization are called c or 180° domain walls, while a or 90° domain walls separate perpendicular domains. 180° domains can be reversed with minimal structural strains. However, switching of 71° , 90° , 109° domains require a significant structural deformation.

An antiferroelectric state is defined as one in which lines of ions in the crystal are spontaneously polarized in antiparallel directions to give a net polarization of zero [41]. The “lines” as defined by Kittel are nowadays referred to as sub cells of antipolar order but the general principles are unchanged. Antiferroelectric domains are then regions where a certain type of antipolar order exists. Antipolar domains do not have a net polarization. The antiferroelectric state, contrary to the ferroelectric one, will not be piezoelectric as a center of symmetry will exist. Antiferroelectric are also defined as antipolar crystals with free energies comparable to polar crystals [4].

2.1.4.1. Polarization Switching and Hysteresis Loops

Polarization switching in ferroelectrics is of particular importance for actuator, sensor and ferroelectric memory applications amongst others. When an external field is applied in a direction opposite to the polarization, the polarization can be reoriented in the direction of the electric field [35]. This process is reversible and is called polarization switching. When the polarization is parallel to an applied electric field, the switching is done. However, it is not necessary that the polarization is exactly reoriented along the electric field direction. The electric field at which a macroscopic polarization changes sign is called the coercive field (E_c). The polarization (macroscopic and /or microscopic) of a ferroelectric or antiferroelectric only exists up to the Curie temperature. The Curie temperature is defined as the temperature where a ferroelectric or antiferroelectric phase changes to a paraelectric phase. When a ferroelectric material is subjected to a large electric field, it shows hysteretic behavior of the polarization and strain. Figure 2.4 display typical polarization and strain hysteresis loop for ferroelectric materials from which various polarization and strain values such as remnant polarization (P_r), coercive electric field (E_c), maximum strain (S_{max}), and negative strain (S_{neg}) can be determined.

Starting with the unpoled ferroelectric material, the initial polarization and strain values are zero at zero electric field ($E_0 = 0$, $P_0 = 0$, $S_0 = 0$). When an electric field is applied, strain and polarization increased up to the maximum applied field (E_{max}) to their respective maximum values (S_{max} and P_{max}). On a microscopic scale, the ferroelectric domains are originally randomly distributed. As the electric field increases, however, domains in which the direction of spontaneous polarization is opposite to electric field begin to switch to a more energetically favorable direction. The switching process continues until all of the domains are aligned in the electric field direction. When the electric field is removed, strain and polarization are reduced but do not return to their initial values entirely in a ferroelectric because most of the domains remained aligned and only a small portion of the domains returns to their original state. These new values are called a remanent strain (S_r) and remanent polarization (P_r). When an electric field is applied in opposite direction, the polarization will return to zero at the negative coercive field ($-E_c$). The

corresponding strain (S_{\min}) will be at a local minimum but not usually return to its original unpoled value ($S_{\min} \neq S_0$). It is usually referred to as negative strain (S_{neg}) since it is lower than S_r [42]. When the field is maximized in negative direction (E_{max}) the strain (S_{max}) and polarization (P_{max}) are reached at nearly all domains are again oriented along the new field direction. Once the field is removed, the cycle can start again but starting from P_r and S_r instead of P_0 and S_0 . It should be noted that, in an ideal ferroelectric, the magnitude of the remanent polarization always equal and is independent of the sign of last applied field. The remanent strain is also equal in magnitude and sign independent of the last field direction [43].

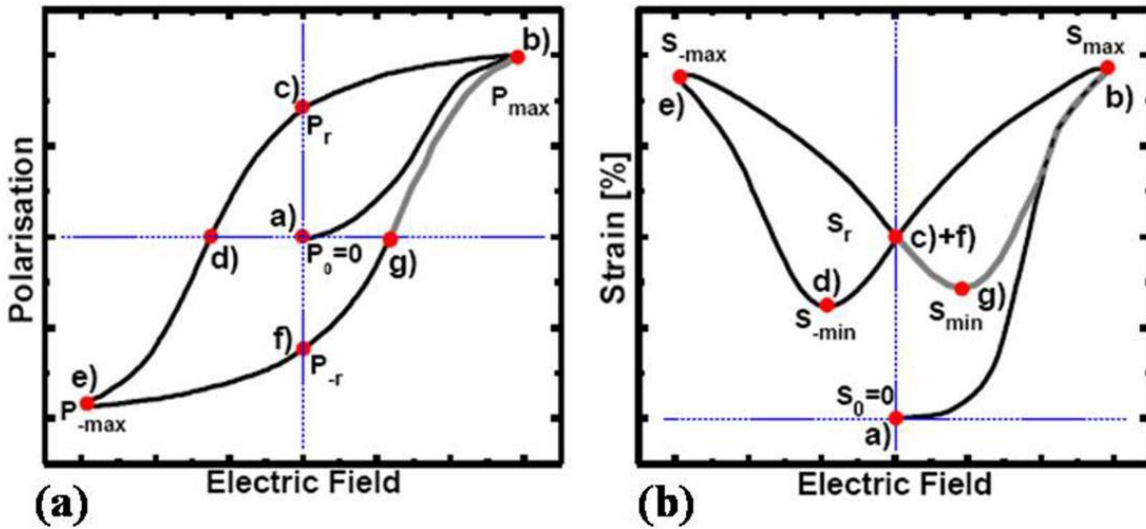


Figure 2.4: (a) Polarization versus large electric field and (b) bipolar strain in field direction in a large electric field [43].

2.2. Relaxor ferroelectrics

2.2.1. Phenomenological signatures of relaxors

Ferroelectric materials usually show minor changes in the dielectric permittivity with frequency due to domain wall oscillations in weak alternative current electric fields. However, some dielectric materials without any ferroelectric long-range order possess significant frequency dispersion in the permittivity, which originates from relaxational processes. Because of that, these materials are called "relaxors" or "relaxor ferroelectrics" and well-known examples are $\text{Pb}(\text{Mg}_{1/3}\text{Nb}_{2/3})\text{O}_3$ (PMN), $(1-x)\text{Pb}(\text{Mg}_{1/3}\text{Nb}_{2/3})\text{O}_3-x\text{PbTiO}_3$ (PMN-PT), and $\text{Pb}_{1-x}\text{La}_x(\text{Zr}_{1-y}\text{Ti}_y)_{1-x/4}\text{O}_3$ (PLZT). The high dielectric and piezoelectric properties of relaxor ferroelectrics make this material class highly interesting for industrial applications. Based on several

selected review articles [15, 30, 44-49], the fundamental concepts and properties of relaxor ferroelectrics will be presented.

The apparent frequency dispersion of relaxors is usually attributed to the presence of chemically disordered regions, which can appear due to, e.g., thermal fluctuations or defects. These nanometer-scale regions are embedded in a highly polarizable, cubic matrix and can contain dipole moments due to the lattice distortion induced by the chemical disorder. If these dipole moments are coupled, they form a region with a local polarization ("polar nanoregion", PNR). A typical temperature-dependent permittivity curve of a relaxor material is shown in Figure 2.5, which will be used to discuss the thermal evolution of this material class.

At high temperatures, the dipoles in the chemical disordered regions are highly mobile and uncorrelated [50]. Therefore, thermal fluctuations prevent these regions from developing a local polarization and the Curie-Weiss law is valid in this paraelectric temperature range without showing any frequency dispersion in the permittivity.

With decreasing temperature, the permittivity curve starts to deviate from the Curie-Weiss law at the Burns temperature T_B [51]. At this temperature, the dipoles in the disordered region become increasingly correlated and PNRs are formed [52-54], which change the symmetry of the material on a local, nanometer sized scale. The PNRs are mobile and not yet correlated to each other, which is why still no frequency dispersion is occurring at temperatures close to T_B [52, 53]. Below T_B and above the Vogel-Fulcher temperature T_{VF} in Figure 2.5, the relaxor is in the ergodic state, in which the spatial and the time average of the polarization directions of the PNRs are equal. The PNRs increase in number and size with further cooling between T_B and the maximum of the permittivity curve T_m [55]. In connection with that, the local polarization increases, and dielectric response is enhanced.

The position of the permittivity maximum in Figure 2.5 is frequency-dependent, which is a typical feature of a relaxor material. At T_m , the correlation length of the PNRs is large enough to overlap with other PNRs. This leads to a reduced mobility in an applied electric field and therefore to a decrease of the dielectric response of the material. With further decrease in temperature, this correlation continues for PNRs with smaller correlation length and T_m occurs at lower temperatures when measured at lower frequencies. It is important to note that no structural phase transition occurs at T_m in a relaxor, which in contrast to a classical ferroelectric material [15, 30, 44-49].

At temperatures below T_m , the correlation of the PNRs increases and the thermally activated reorientation of PNRs decreases. Both effects result in a lower permittivity with decreasing temperature (Figure 2.5).

The frequency dispersion is a consequence of the dielectric relaxation of the differently sized and correlated PNRs in a weak oscillating electric field. Larger PNRs react slower to the electrical field and show therefore reduced dielectric properties at higher frequencies, where smaller PNRs still can follow the electric field at higher frequencies. This kind of relaxation process does not possess a single characteristic relaxation time, but a distribution of relaxation times due to the differently sized and correlated PNRs. Like in the case of polymers, this relaxation can be described by a Vogel-Fulcher type relationship, which results in the observed frequency-dependency of the permittivity [15, 30, 44-49].

By approaching the Vogel-Fulcher temperature T_{VF} , the motion of the PNRs freezes, i.e., the relaxations times diverge towards infinity and the spatial and the time average of the PNRs are not equal anymore. Therefore, the relaxor changes to the nonergodic state at T_{VF} , but this state change is not accompanied by a structural phase transition and only connected to the frozen dynamics of the PNRs. In addition, no signature of the state change can be observed in the permittivity-temperature curve in Figure 2.5 unless the frequency-dependency of the permittivity is evaluated. The freezing temperature T_{VF} is influenced by the application of an electric field [56, 57]. Finally, the permittivity decreases with further cooling below T_{VF} due to reduced motion of the dipoles and the PNR walls.

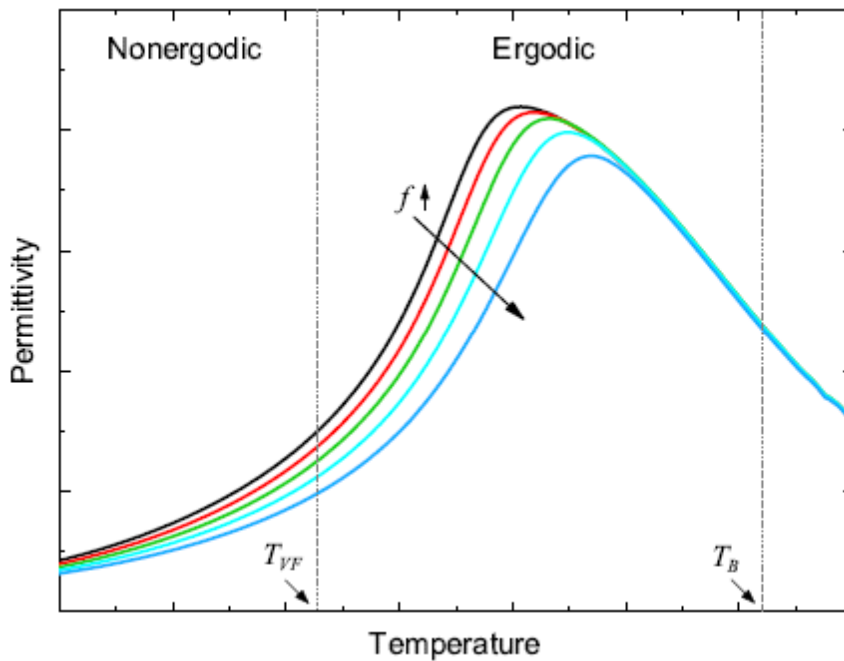


Figure 2.5: Exemplary permittivity-temperature curve of a relaxor ferroelectric measured at various frequencies. At the burn temperature T_B , polar nanoregions are forming during cooling, whereas the motion of these regions freezes at the Vogel-Fulcher temperature.

In some materials like PMN-PT, a sharp or diffuse phase transition from a relaxor to a ferro- electric phase can occur during cooling, which is usually marked by an anomaly in the permittivity at the phase transition temperature [47, 58, 59]. In addition, it is also possible to induce a ferro- electric phase by applying an electric field to a relaxor. Various authors reported such induced phase transition in e.g. PMN [60-62], PLZT [63-65], PMN-PT [66, 67], $(1-x)\text{Pb}(\text{Zn}_{1/3}\text{Nb}_{2/3})\text{O}_3\text{-}x\text{PbTiO}_3$ (PZN-PT) [67], $(1-x)(\text{Bi}_{1/2}\text{Na}_{1/2})\text{TiO}_3\text{-}x\text{BaTiO}_3$ (BNT- x BT) [56, 68], or Mn-doped $\text{Bi}_{0.5}(\text{Na}_{0.9}\text{K}_{0.1})_{0.5}\text{TiO}_3$ [69]. Figure 2.6 shows the temperature-dependent permittivity of a PMN-PT single crystal [66] and of PLZT [70] during heating. Prior to the measurements, the samples were poled with a direct current electric field. It can be clearly seen that the permittivity shows an anomaly (PMN-PT) or a peak (PLZT) at the ferroelectric-to-relaxor transition temperature T_{F-R} .

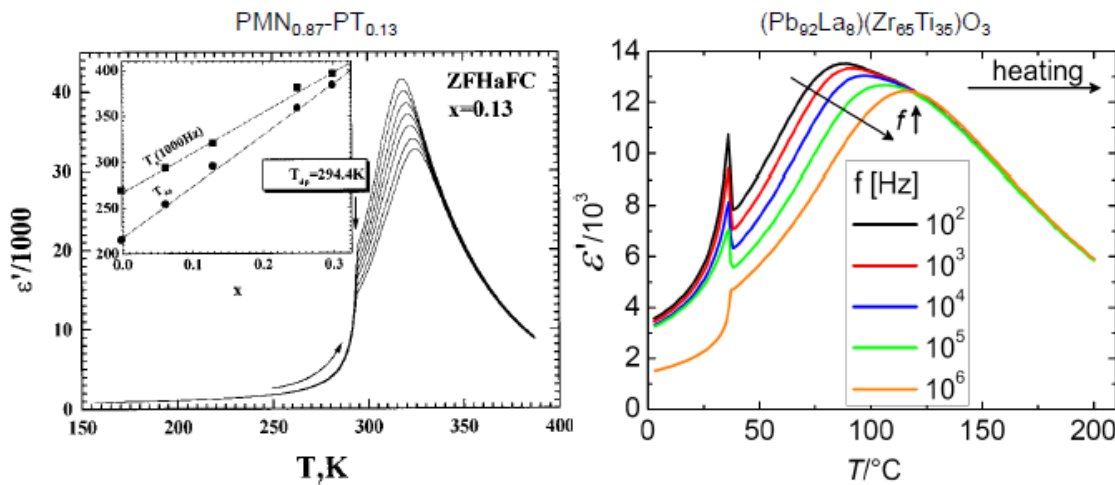


Figure 2.6: Temperature-dependent permittivity of a PMN-PT single during heating. The samples were electrically poled prior to each measurement. The anomalies in both curves mark the ferroelectric-to-relaxor phase transition temperature [143].

The mechanism behind the electric field-induced phase transition is not completely understood. It is known that the PNRs initially align and grow with the application of an electric field [61], but the step following a further increase of the field is proposed to be either complete coalescence [71] or percolation [72] of PNRs, which could probably also depend on the material under investigation. In any case, a remanent ferroelectric phase can only be induced if the relaxor is in the nonergodic state below T_{VF} , because thermally enhanced motion of the PNRs would destroy the ferroelectric order on the ergodic state. It is important to note that T_{F-R} (occurs during heating) and T_{VF} (occurs during cooling) does not necessarily need to coincide, since the induced long-range ferroelectric order might be already thermally destroyed

below T_{VF} [73, 74]. However, a large unipolar strain could be achieved in the ergodic phase due to the reversible electric field-induced phase transition. Such a behavior was found in polycrystalline $(0.94-x)\text{BNT}-0.06\text{BT}-x(\text{K}_{1/2}\text{Na}_{1/2})\text{NbO}_3$ (BNT-BT-KNN) for $x = 2$ mol% and 6 mol%, which is in the ergodic state at room temperature [18, 19, 42].

2.2.2. Models describing relaxation mechanisms

Several theories exist that attempt to describe the observed electromechanical behavior of relaxor ferroelectrics. Among them some are briefly described below

2.2.2.1. Compositional heterogeneity/fluctuations and diffused phase transition

Smolensky [75] and Kirillov and Isupov [76] assumed that the compositional heterogeneity causes different local Curie temperatures which have a Gaussian distribution around the mean Curie temperature. As a result, the broad maximum of dielectric susceptibility is understood in terms of a diffuse phase transition consisting of a series of local phase transitions. The local transitions are assumed to be of the first order, giving rise to mostly PNRs in the non-polar phase above the mean Curie transition. The arising PNRs are assumed to flip because of thermal fluctuations. Below the mean Curie temperature, the thermally activated reorientation of the regions ceases (their polarization freezes) and simultaneously polar regions fill the whole volume [75, 76].

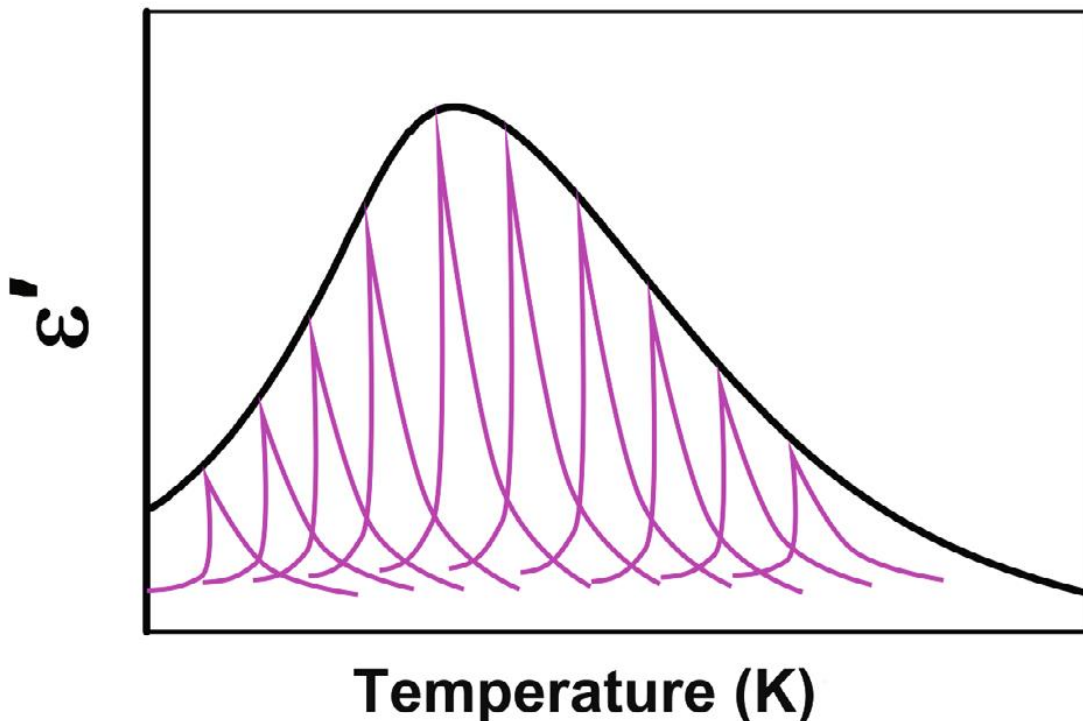


Figure 2.7: The diffuse phase transition model insulation[49].

2.2.2.2. Superparaelectric model

The above compositional heterogeneity model was extended by Cross [15] who suggested that the small PNRs, postulated to exist in relaxor ferroelectrics, could permit dynamical (thermal) disordering over some range of sizes in a similar manner as spin clusters in the superparamagnetic state. In addition to that the potential minima, between whose PNR states flip, should be different in depth because of different local symmetries caused by the internal compositional heterogeneity. As a result, the polar vector will spend longer time in the deepest minimum so that PNR will have a net (weak) polar moment [44].

To calculate the dielectric response, Bell assumed an ideal superparaelectric material, defined as an ensemble of independent, coherently polarizing PNRs, in which each PNR behaves as an independent, classical ferroelectric and the size of PNRs is such that the direction of polarization may be reoriented by thermal fluctuations of the lattice [77]. It is shown that departure from normal ferroelectric behavior becomes significant when the size of coherently polarizing regions is less than 15 nm. Even without invoking a distribution of Curie temperatures, the finite-size constraints predict local polarization fluctuations above the Curie temperature and a departure from the Curie-Weiss law. However, it is noted that the imaginary part of the dielectric constant shows a relaxor behavior when the distributions of sizes is included in the model. The introduction of the electrostatic dipole-dipole interaction, in the form of mean field, leads to a spontaneous transition to a macroscopic ferroelectric state, depending on the interaction strength [44, 49].

2.2.2.3. Dipolar glass model

Relaxor ferroelectrics resemble spin glasses by broken ergodicity near and below T_f and possess main characteristics of nonergodic behavior, e.g. anomalously wide spectrum of relaxation frequencies fulfilling the VF relationship, ageing, dependence of the thermodynamic state on the thermal and field history of a sample [30]. In spin glasses, the nonergodic behavior is explained by a multivalley potential, whose some barriers are so high that the time needed to overcome them is larger than any practically reasonable observation time. Thus, the spin glass cannot reach all the configuration states during the observation time, and consequently, the usual thermodynamic averaging and the time averaging give different results. On contrary, the ferroelectric phase of classical ferroelectrics is also nonergodic, however, the potential minima are equivalent. Due to the compositional disorder, the potential of relaxor ferroelectrics is likely to be more structured than in ferroelectrics and its minima non-equivalent due to the locally broken symmetry as pointed out by Cross [44]. Even though the similarity between relaxor ferroelectrics and dipole glasses is remarkable, there are some differences. For example, field-induced ferroelectric phases and ferroelectric hysteresis loops have not been observed in typical dipole glasses [30].

2.2.2.4. Random field model

In this model, the relaxor behavior is attributed to the existence of domain states induced by a quenched random field arising from charged nano domains and compositional fluctuations [78]. By application of this concept to PMN, they explain the origin of relaxor behavior of PMN is due to intrinsic charge disorder by Mg^{2+} and Nb^{5+} ions inducing uncorrelated and quenched electric field at the Pb^{2+} and Nb^{5+} sites, which are ferroelectric active [78]. The random electric fields in the disordered system can be caused by ionic vacancies, impurities, and other imperfections. However, the main reason of the random field in the disordered dielectrics is the impurity electric dipole, which can have some discrete direction in a host dielectric lattice [79, 80].

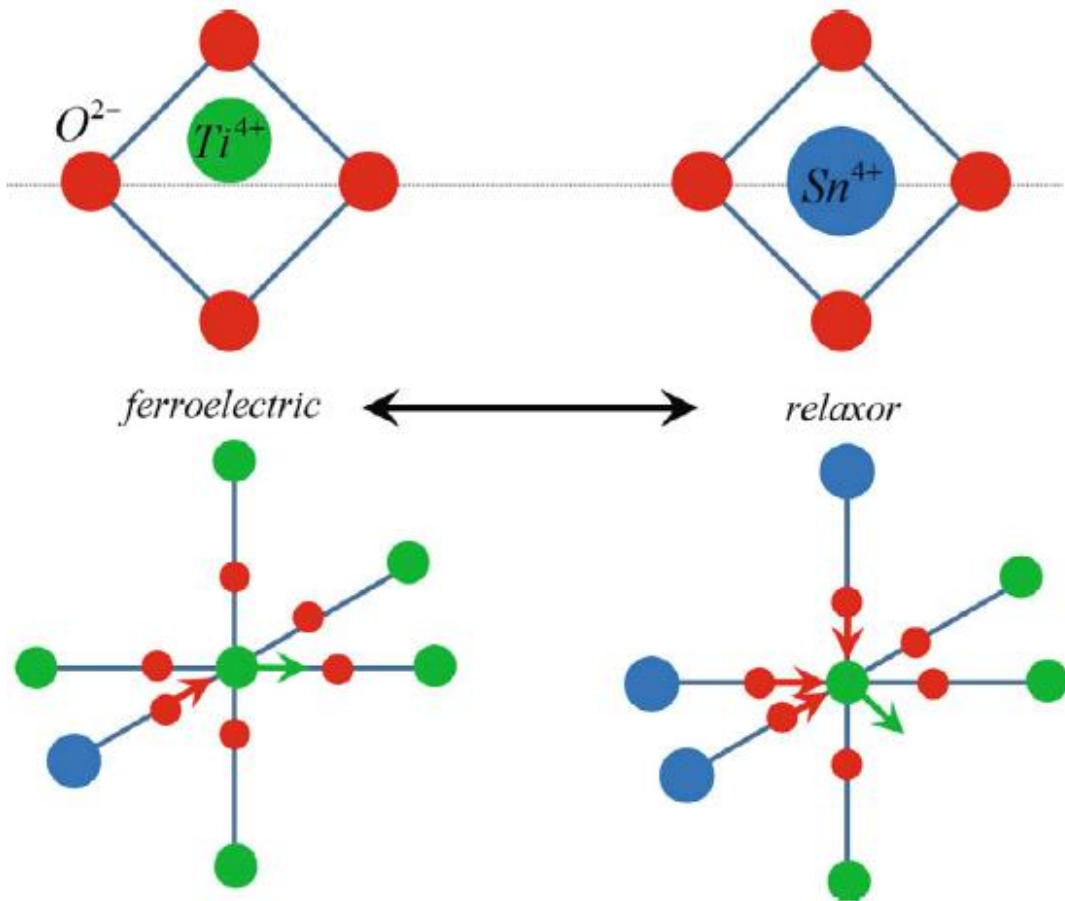


Figure 2.8: A schematic illustration showing how isovalent doping influences the quenched random electric fields that disrupt a long-range ferroelectric order [49].

One of the most important success of the random-field model is explanation for the ferroelectric-to-relaxor crossover during isovalent substitution such as in $\text{BaTi}_{1-x}\text{Sn}_x\text{O}_3$ (BTS) [81] and $\text{BaTi}_{1-x}\text{Zr}_x\text{O}_3$ (BTZ) [82, 83]. When the material is substituted by isovalent ions such as substituting Ti^{4+} to bigger Sn^{4+} for BTS (Figure 2.8), there is no charge disorder, instead a non-ferroelectric environment increases that eventually hinders the individual dipoles from aligning collectively to form a ferroelectric order. This leads to the variation in the distortion of TiO_6 octahedra, which is contributed to the induced relaxor state in the BTS material [49].

2.3. Phase transition and phase boundary

To improve the piezoelectric and electromechanical properties of lead-based and lead-free piezoelectric ceramics, a coexistence of multiple phase is considered as a method to achieve the purpose [84]. Accordingly, the concept of “morphotropic phase boundary” (MPB) was first mentioned by Jaffe et al. [85], who discovered the highest value of piezoelectric constant of PZT in a composition around an MPB [85]. From a theoretical viewpoint, a phenomenological theory, which is developed by Landau, and first-principles calculations were used to explain the phase transition in piezoelectric materials [86-88]. The Gibbs free energy is the fundamental concept behind the Landau theory, which is dependent on the temperature, composition, electric field, and other external parameters [86]. It is generally considered that the flatness of the Gibbs free energy profile (the instability of Gibbs free energies) is greatest near the phase transition (Figure 2.9), which is attributed to promote the polarization rotation and piezoelectricity enhancement [86]. Therefore, the formation of phase boundaries should be observed as a powerful tool in improvement of electrical performances of perovskite piezoelectric materials, especially for the improvement of piezoelectricity.

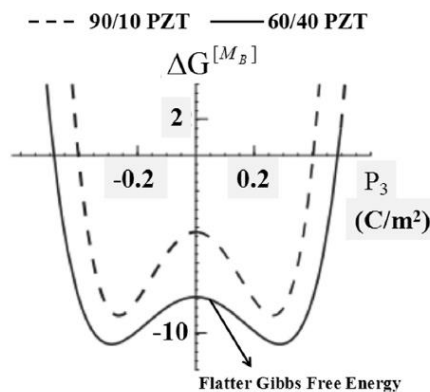


Figure 2.9: Cross-section of the Gibbs free energy for 90/10 and 60/40 $\text{Pb}(\text{Zr}_{1-x}\text{Ti}_x)\text{O}_3$ along $[\text{M}_B]$ path [89].

2.3.1. Phase boundaries in lead-based piezoelectric materials

2.3.1.1. $\text{Pb}(\text{Zr}, \text{Ti})\text{O}_3$ piezoelectric compositions

Ferroelectric properties of PbTiO_3 are known since the early 1950s [90]. Many of its properties are analogous to that of BaTiO_3 [91]. Its room temperature crystal structure is tetragonal, and it undergoes a paraelectric to ferroelectric phase transition at its Curie temperature ($T_C = 490^\circ\text{C}$). Among the perovskite solid solutions, PbZrO_3 - PbTiO_3 (PZT) solid solution has widespread application in technology [90, 92]. The PbZrO_3 - PbTiO_3 phase diagram is shown in Figure 2.10 [85, 93]. These enhanced properties were found to be at the boundary of a rhombohedral ($R3c$) to tetragonal ($P4mm$) structure transition. Additionally, this phase transition is largely temperature independent, differentiating it from transitions that are more sensitive to temperature changes. The former is deemed the morphotropic phase boundary (MPB), while the latter is referred to as a polymorphic phase transition (PPT).

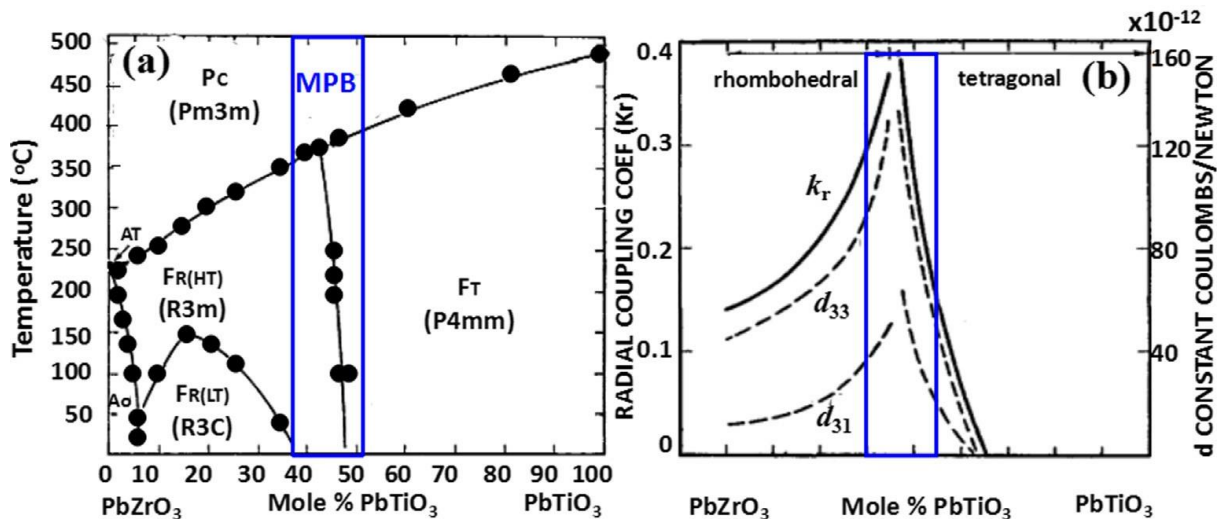


Figure 2.10: (a) Phase diagram of $(1-x)\text{PbZrO}_3$ - $x\text{PbTiO}_3$ and (b) composition-dependent piezoelectric properties of $(1-x)\text{PbZrO}_3$ - $x\text{PbTiO}_3$ ceramics [89].

The enhanced electromechanical properties found at the morphotropic phase boundary were originally attributed to enhanced polarizability due to an increased number of possible polarization directions. At the MPB, there is a lowering of Gibbs free energy between coexisting, ferroelectric states allowing for these additional polarization orientations and domain wall mobility [94]. Structural studies later revealed that a monoclinic phase (Cm) was present in the MPB region where it was once thought to only be a coexistence of rhombohedral and tetragonal structures [93, 95-97]. This monoclinic phase's symmetry allows for the rotation of the polarization directions between the pre-MPB rhombohedral phase (PbZrO_3 side) and the post-MPB tetragonal phase (PbTiO_3 side). This monoclinic, bridging phase reduces the energy for the

polarization vector realignment and enhances the piezoelectric response [88, 98-100]. This concept of enhanced electromechanical properties at the transition between two ferroelectric phases sparked a wave of research that attempted to replicate the success found with lead-containing, PZT.

2.3.1.2. $\text{Pb}(\text{Mg}, \text{Nb})\text{O}_3$ piezoelectric compositions

$\text{Pb}(\text{Mg}, \text{Nb})\text{O}_3$ (PMN) is a relaxor ferroelectric with a low Curie point ($T_C = -10^\circ\text{C}$). PMN possesses a broad and diffused phase transition below the Curie point. It exhibits high dielectric constant and less temperature dependence of the dielectric constant close to room temperature. The dielectric constant is dependent on frequency and with frequency the Curie point can shift to higher temperatures [101]. The phase diagram of PMN-PT near the MPB region is shown in Figure 2.11. $(1-x)\text{Pb}(\text{Mg}_{1/3}\text{Nb}_{2/3})\text{O}_3$ - $x\text{PbTiO}_3$ solid solution for $x < 0.20$ shows relaxor behavior, revealing very high maximum dielectric constant ($\sim 30,000$). When compared to the dielectric constant of BaTiO_3 (10,000), which is currently used in multilayer capacitors, PMN-PT solid solution gives high dielectric constant value for composition with x between 0.05 and 0.10. Since the dielectric permittivity in this compositional region is very high, the PMN-PT solid solutions are very good candidates for high charge density capacitors.

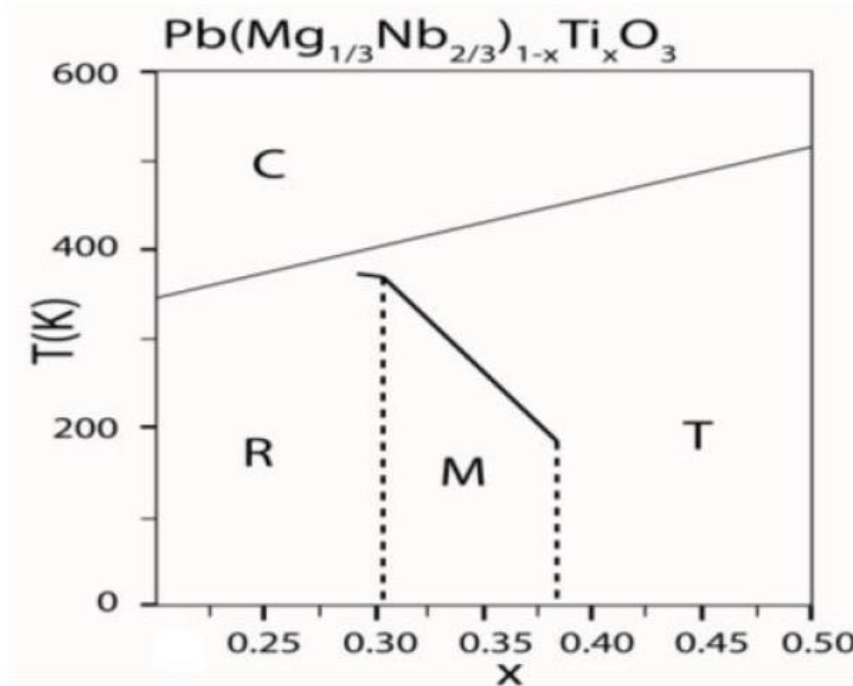


Figure 2.11: Temperature versus composition phase diagram of PMN-PT (C: cubic, R: rhombohedral, M: monoclinic, T: tetragonal) [101].

Even though PMN-PT solid solution shows high piezoelectric response, it has some disadvantages such as low TC and lower rhombohedral to tetragonal transition temperature. Since T_C is very low, thermal depoling may happen to the ceramics at high operating temperature. Hence the operating temperature must be kept low always. The operating temperature range of piezoelectric materials is 2/3 of the lowest phase transition temperature so that the depoling can be avoided. The low depoling temperature of PMN-PT solid solution makes the material difficult in application.

2.3.2. Phase boundary in $\text{Bi}_{0.5}\text{Na}_{0.5}\text{TiO}_3$ -based ceramics

BNT is a perovskite ferroelectric with rhombohedral symmetry at room temperature. It has at least two more structural phase transitions between room temperature and its sintering temperature. In 2002 Jones and Thomas [102] reported a detailed structural investigation on BNT, which suggested a rhombohedral to tetragonal phase transition between 200°C and 320°C and from tetragonal to cubic phase at 540°C [102]. The region between 200 and 320°C has been considered exhibiting a coexistence of rhombohedral and tetragonal phases with polar regions [103, 104] and often designated as the depolarization temperature (T_d) [105, 106]. BNT ceramic shows strong ferroelectric property of a large remanent polarization ($P_r \sim 38 \mu\text{C}/\text{cm}^2$) and relatively high piezoelectric properties ($d_{33} \sim 73 \text{ pC}/\text{N}$) compared with other lead-free piezoelectric ceramics [107]. Therefore, BNT has become a promising candidate to replace lead-based piezoelectric materials. Even though, there are some drawbacks such as high coercive field ($E_c \sim 73 \text{ kV}/\text{cm}$) and high conductivity, which hinders the BNT into the actual applications. To overcome these issues, the construction of phase boundaries through chemical modification (ion doping or solid solutions) is a favorable and widely approach for improving the electrical performances of BNT materials.

It is noted that there are two kinds of morphotropic phase boundary (MPB) existing in BNT ceramics, namely MPB(I), and MPB(II), which can be often found by doping different additives [107, 108]. The first type MPB(I) is almost borrowing ideas from the typical MPB concept of lead PZT. In the MPB(I) boundary, the coexistence of ferroelectric rhombohedral and tetragonal phases results in the improvement of piezoelectricity. Appropriately, enhanced piezoelectric coefficient d_{33} , high dielectric constant ϵ_r and large electromechanical coupling factor k_p are found to be obtained at this MPB range. By contrast, the second type MPB(II) boundary involves a phase transition from ferroelectric to antiferroelectric or from ferroelectric to relaxor ferroelectric (FE-RFE), which does not show a significant piezoelectric coefficient but has recently received significant attention due to its high electromechanical strain properties [22, 27, 108-114]. This kind of phase transition is appropriate for describing polymorphic phase transition rather than the typical MPB due to its temperature independence.

2.3.2.1. $\text{Bi}_{0.5}\text{Na}_{0.5}\text{TiO}_3\text{-BaTiO}_3$ (BNT-BT) solid solutions

$\text{Bi}_{0.5}\text{Na}_{0.5}\text{TiO}_3\text{-BaTiO}_3$ (BNT-BT or BNBT) solid solution is one of promising lead-free piezoelectric ceramic, which was first reported by T. B. Wang et al. [115] in 1987, they mention the MPB at around 6 mol% of BT level. In 1991, T. Takenaka et al. [116] studied the $(1-x)\text{BNT-xBT}$ (BNT-BT100x) in more detail, they found that the BNT-BT has a rhombohedral-tetragonal MPB at $x = 0.06\text{--}0.07$ at room temperature. The temperature dependence of dielectric constant of BNBT5 display a broad shape near the Curie point and may be a result of the diffuse phase transition because the BNT-BT system is a typical example of a relaxor ferroelectric with A-site complex ions. The three phases of ferroelectric, antiferroelectric and paraelectric, which exist in a wide temperature range, can be recognized by anomalies of the dielectric constant and dielectric loss. The temperature dependence of polarization of BN-BT5 confirmed the ferroelectric and antiferroelectric phase transition, respectively. By the same observation on all compositions of BN-BT system, they constructed a temperature and composition dependent phase diagram based on x-ray diffraction, dielectric and piezoelectric data up to 30 mol% barium titanates, as seen in Figure 2.12. The room temperature properties of MPB at $x = 0.06$ ceramic were presented at dielectric constant of 580, piezoelectric constant d_{33} of 125 pC/N, coupling factor k_{33} of 55%, and Curie temperature T_c of 288°C , which appear effective for high-frequency ultrasonic or piezoelectric actuator application, respectively. In 2002, B. J. Chu et al. [117] also presented electrical properties of BNT-BT ceramics. The x-ray diffraction of NBT-BT system showed the rhombohedral-tetragonal MPB near 0.06 mol BT level, which is coincides with previous studies [115, 116].

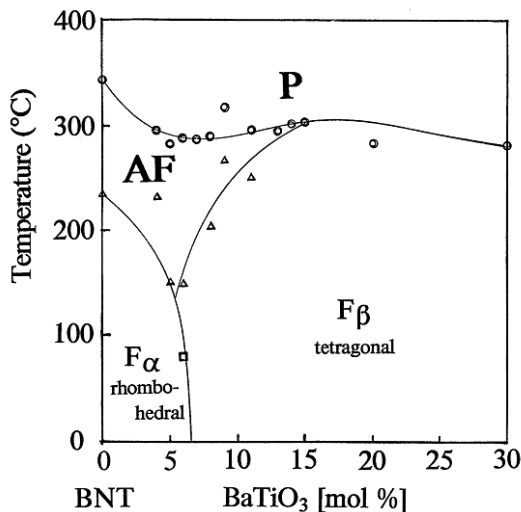


Figure 2.12: Phase diagram of BNT-BT solid solution, (F_{α} : ferroelectric rhombohedral phase, F_{β} : ferroelectric tetragonal phase, AF: antiferroelectric phase, P: paraelectric phase) [19].

In 2005, R. Ranjan et al. [118] provide a detailed powder x-ray diffraction analysis for compositions around the MPB. They show that there are no measurable tetragonal lattice distortions or tetragonal superstructure reflexes in BNT–BT between the MPB (6 mol% BT) and 10 mol% BT. They instead claim a nearly cubic phase. C. Xu et al. [119], however, show clear tetragonal distortion above 6 mol% BT added. The remnant polarization (P_r) peaks at the MPB at $38.8 \mu\text{C}/\text{cm}^2$ [119]. The coercive field (E_c) is continuously reduced with increasing BT content up to its lowest value of 3.25 kV/mm at 8 mol% BT. Compositional dependence of d_{33} , k_0 , ϵ_r , and $\tan\delta$ is reported up to 12 mol% BT with their optimum values of 155 pC/N, 36.7%, and approximately 2.5%, respectively, at the MPB (6 mol% BT). In contrast, the relative dielectric constant ϵ_r peaks at 8 mol% BT with 1099 [119]. This is in contradiction to the original results previous [115-117]) but no reason is evident. C. Xu et al. [119] also measure the diffuseness of the phase transition at T_d . The gamma value of MPB of BNT–BT is reported as 2.02, making it a pure relaxor, which is also reported here [120]. The relaxor nature is attributed to the A-site cation disorder of BNT–BT. At the MPB, temperature-dependent k_p shows a drop around 80°C , while it for d_{33} and $\tan\delta$ is about 105°C . Temperature-dependent polarization hysteresis for 0, 6 and 12 mol% BT content show a typical ferroelectric behavior below 140°C , 60°C and 160°C , respectively, with decreasing E_C when the temperature increases [120]. Above these respective temperatures, antiferroelectric-like pinched loops or nearly double loops are found in all three compositions. The fact that there is always some small amount of hysteresis at low fields is treated as evidence that above T_d a small amount of polar ferroelectric material remains. On the basis of TEM results and temperature dependence permittivity of MPB of BNT–BT solid solution, C. Ma et al. [121] reported that the 6 mol% BT composition belongs to a rhombohedral R3c phase, having a complex domain structure while the 7 mol% BT consist of a tetragonal P4bm phase with nanodomain morphology. Even though the MPB was believed as rhombohedral–tetragonal phase transition [117] or nearly cubic [118] in the past. Table 2.1 summarizes the electrical properties of BNT-BT ceramics. The arguments on the phases as well as unopened properties of MPB compositions, lead BNT–BT solid solution become more interesting in research so far.

Table 2.1: Electrical properties of BNT-BT ceramics

| Material system | Phase structure | d_{33} (pC/N) | k_p | T_m ($^\circ\text{C}$) | T_d ($^\circ\text{C}$) | Ref. |
|--|-----------------|-----------------|-------|----------------------------|----------------------------|-------|
| $0.94\text{Bi}_{1/2}\text{Na}_{1/2}\text{TiO}_3\text{-}0.06\text{BaTiO}_3$ | R-T | 125 | 0.2 | 288 | | [116] |
| $0.94\text{Bi}_{1/2}\text{Na}_{1/2}\text{TiO}_3\text{-}0.06\text{BaTiO}_3$ | R-T | 122 | 0.29 | 225 | 100 | [117] |
| $0.94\text{Bi}_{1/2}\text{Na}_{1/2}\text{TiO}_3\text{-}0.06\text{BaTiO}_3$ | R-T | 155 | 0.367 | | 105 | [119] |
| $0.94\text{Bi}_{1/2}\text{Na}_{1/2}\text{TiO}_3\text{-}0.06\text{BaTiO}_3$ | R-T | 148 | – | | | [122] |

| | | | | | | |
|--|-----|-----|------|-----|-----|-------|
| 0.93Bi _{1/2} Na _{1/2} TiO ₃ -0.07BaTiO ₃ | R-T | 134 | – | 305 | 165 | [123] |
| 0.925Bi _{1/2} Na _{1/2} TiO ₃ -0.075BaTiO ₃ | R-T | 186 | – | | | [124] |
| 0.935Bi _{1/2} Na _{1/2} TiO ₃ -0.065BaTiO ₃ | R-T | 150 | 0.51 | | | [125] |
| 0.94Bi _{1/2} Na _{1/2} TiO ₃ -0.06BaTiO ₃ | R-T | 174 | 0.28 | 284 | | [126] |

2.3.2.2. Bi_{0.5}Na_{0.5}TiO₃-Bi_{0.5}K_{0.5}TiO₃ (BNT-BKT) solid solutions

Bismuth sodium titanate (BNT) and bismuth potassium titanate (BKT) solid solution is one of the well-known lead-free binary ceramic systems (BNT-BKT or BNKT), which was synthesized by Elkechai et al. in 1996 [127]. Later, the enhanced piezoelectric properties were discovered in the composition being close to the rhombohedral-tetragonal phase boundary. From the study of Sasaki et al, the existence of a MPB between BNT and BKT, indicating a coexistence of rhombohedral and tetragonal phases, in the compositional range 16-20 mol% BKT was investigated, which based on the structural analysis as well as the corresponding compositionally dependent peaks in dielectric and piezoelectric coefficients [128]. Yoshii et al. investigated the electrical properties of BNT-BKT ceramics focusing on the depolarization temperature (T_d) [105]. Near the MPB compositions, highest electromechanical coupling factor ($k_{33} = 0.56$) for BNT-16BKT and a high remanent polarization ($P_r = 38.4 \mu\text{C}/\text{cm}^2$) and piezoelectric constant ($d_{33} = 157 \text{ pC}/\text{N}$) were achieved for BNT-20BKT ceramics [105]. Yang et al. [129] reported the MPB in the range of 16-20 mol% BKT in BNT-BKT, which agrees with the results of Sasaki et al. [128]. They focused on optimization of processing parameters, find that d_{33} , $\tan\delta$, ϵ_r and k_p improve up to a maximum sintering temperature of 1170°C, after which they decrease slightly. The best values were found to be 144 pC/N, 3.7%, 893, and 0.29, respectively, at 18 mol% BKT [129]. Hiruma et al. also reported different properties, which show optimum values at different mole percentages of BKT. In particular, d_{33} and k_{33} are maximized with values of 157 pC/N and 0.56, respectively at 20 mol% BKT, while ϵ_{33} , and E_c are optimal at 22 mol% BKT [105]. Zhang et al. also achieved a highest d_{33} of ~192 pC/N with the highest k_p of ~32% at 22 mol% BKT in BNT-BKT ceramics sintered at 1150°C [130]. The summary of properties of BNT-BKT solid solutions are showed in Table 2.2.

Recently, an enhancement in the electric-field induced strain properties can be achieved in BNT-BKT ceramics by addition of some ions. In Table 2.3, a list of phase structure and electrical properties of ion doped-BNT-BKT ceramics is revealed. It is reported that the substitution of ion B-site such as Hf⁴⁺, Zr⁴⁺, Sn⁴⁺, Nb⁵⁺, and Ta⁵⁺ in BNT-BKT can decrease the depolarization temperature (T_d), which results in a disruption of the long range ferroelectric and induces a phase transition from a ferroelectric (rhombohedral-tetragonal) phase to a non-polar (pseudo cubic) phase [131-135]. In addition, the effects

of ion types on the properties were also investigated. In 2012, by comparison of isovalent Sn^{4+} and aliovalent Ta^{5+} doping on B-sites Ti^{4+} in lead-free $\text{Bi}_{1/2}(\text{Na}_{0.82}\text{K}_{0.18})_{1/2}\text{TiO}_3$ perovskite, Han et al found that although both dopants led to a diffuse phase transformation, Ta^{5+} substitution more rapidly induced the ferroelectric-relaxor transition than Sn^{4+} , which is attributed to the donor-induced A-site vacancies by Ta^{5+} [136]. Furthermore, a comparison of Li^+ - and La^{3+} doped BNKT ceramics was made by Dinh et al. [137]. It was found that the addition of Li can result in saturated P-E loops and typical butterfly shaped S-E curves, while La induces a ferroelectric-relaxor phase transition, which leads to increased strain. In a conclusion, polycrystalline materials in the BNT–BKT system are interesting lead–free alternatives because they have a simple chemical formula, easy fabrication process (conventional solid-state reaction), and low cost of the raw materials. Moreover, the existence of MPB similar to the PZT system and excellent electrical properties suitable for applications make these materials interesting.

Table 2.2: Electrical properties of BNT-BKT ceramics

| Material system | Phase structure | d_{33} (pC/N) | k_p | T_m (°C) | T_d (°C) | Ref. |
|---|-----------------|--------------------|-------|---------------|---------------|-------|
| 0.80 $\text{Bi}_{1/2}\text{Na}_{1/2}\text{TiO}_3$ -0.20 $\text{Bi}_{1/2}\text{K}_{1/2}\text{TiO}_3$ | R-T | 157 | | 270 | 174 | [105] |
| 0.82 $\text{Bi}_{1/2}\text{Na}_{1/2}\text{TiO}_3$ -0.18 $\text{Bi}_{1/2}\text{K}_{1/2}\text{TiO}_3$ | R-T | 144 | 0.29 | | 150 | [129] |
| 0.78 $\text{Bi}_{1/2}\text{Na}_{1/2}\text{TiO}_3$ -0.22 $\text{Bi}_{1/2}\text{K}_{1/2}\text{TiO}_3$ | R-T | 192 | 0.32 | | | [130] |
| 0.77 $\text{Bi}_{1/2}\text{Na}_{1/2}\text{TiO}_3$ -0.23 $\text{Bi}_{1/2}\text{K}_{1/2}\text{TiO}_3$ | R-T | 207 | 0.35 | | | [138] |
| 0.80 $\text{Bi}_{1/2}\text{Na}_{1/2}\text{TiO}_3$ -0.20 $\text{Bi}_{1/2}\text{K}_{1/2}\text{TiO}_3$ | R-T | 195 | 0.27 | 284 | 100 | [139] |

Table 2.3: Electrical properties of BNKT ceramics with ion substitution

| Material system | Phase structure | d_{33} (pC/N) | Strain (%) | d_{33}^* (pm/V) | Ref. |
|--|-----------------|--------------------|---------------|----------------------|-------|
| $\text{Bi}_{1/2}(\text{Na}_{0.7}\text{K}_{0.2}\text{Li}_{0.1})_{1/2}\text{TiO}_3$ | | 231 | | | [140] |
| $\text{Bi}_{1/2}(\text{Na}_{0.78}\text{K}_{0.2}\text{Ag}_{0.02})_{1/2}\text{TiO}_3$ | R | 180 | | | [141] |
| $\text{Bi}_{1/2}(\text{Na}_{0.78}\text{K}_{0.22})_{1/2}(\text{Ti}_{0.97}\text{Hf}_{0.03})\text{O}_3$ | | | 0.38 | 475 | [132] |
| $\text{Bi}_{1/2}(\text{Na}_{0.78}\text{K}_{0.22})_{1/2}(\text{Ti}_{0.97}\text{Zr}_{0.03})\text{O}_3$ | | 31 | 0.43 | 614 | [131] |
| $\text{Bi}_{1/2}(\text{Na}_{0.82}\text{K}_{0.18})_{1/2}(\text{Ti}_{0.97}\text{Nb}_{0.03})\text{O}_3$ | RT-Pc | | 0.47 | 641 | [135] |
| $\text{Bi}_{1/2}(\text{Na}_{0.82}\text{K}_{0.18})_{1/2}(\text{Ti}_{0.98}\text{Ta}_{0.02})\text{O}_3$ | RT-Pc | | 0.34 | 566 | [134] |
| $\text{Bi}_{1/2}(\text{Na}_{0.78}\text{K}_{0.22})_{1/2}(\text{Ti}_{0.95}\text{Sn}_{0.05})\text{O}_3$ | T-Pc | | 0.35 | 585 | [133] |

| | | | | |
|---|----------|-----------------------|-----------------------|-------|
| $[\text{Bi}_{1/2}(\text{Na}_{0.82}\text{K}_{0.18})_{1/2}]_{0.97}\text{Li}_{0.03}\text{TiO}_3$ | | 110 | 250 | [137] |
| $[\text{Bi}_{1/2}(\text{Na}_{0.82}\text{K}_{0.18})_{1/2}]_{1-x}\text{La}_x\text{TiO}_3$ | | 172 ($x = 0.02$) | 650 ($x = 0.03$) | [137] |
| $(\text{Bi}_{0.5}\text{Na}_{0.78}\text{K}_{0.18}\text{Li}_{0.04})_{0.5}(\text{Ti}_{0.95}\text{Sn}_{0.05})\text{O}_3$ | T-Pc | 0.39 | 646 | [142] |
| $(\text{Bi}_{0.5}\text{Na}_{0.385}\text{K}_{0.09}\text{Li}_{0.025})(\text{Ti}_{0.975}\text{Ta}_{0.025})\text{O}_3$ | RT-Pc | 0.436 | 727 | [143] |
| $[\text{Bi}_{0.5}(\text{Na}_{0.84}\text{K}_{0.16})_{0.5}]_{0.96}\text{Sr}_{0.04}\text{Ti}_{0.975}\text{Nb}_{0.025}\text{O}_3$ | R3c-P4bm | 0.70 | 1400 | [144] |

2.3.2.3. $\text{Bi}_{0.5}\text{Na}_{0.5}\text{TiO}_3\text{-SrTiO}_3$ (BNT-ST) solid solutions

The lead-free solid solution between BNT and SrTiO_3 (ST) was first reported by Sakata and Masuda [20] in 1974 with the aim to shift the phase transitions of pure BNT to lower temperatures, thus allowing a systematic study of the functional properties of the system. Several studies have demonstrated that increasing ST content in BNT-based materials leads to destabilization of the long-range ferroelectric state and decreased T_d as well as P_r [21, 145-148]. The BNT-ST is a binary solid solution between the end members BNT and ST. The BNT-ST displays a rhombohedral structure at room temperature below 20 mol% ST [149, 150]. Increasing ST content leads to a gradual increase in the lattice parameter between 3.885 Å and 3.905 Å [151]. The increase in lattice parameter is accompanied by a gradual decrease of the unit cell distortion from rhombohedral to pseudocubic below 20 mol% ST. Further ST content leads to a considerable change of the rhombohedral distortion at room temperature and vanishing non-cubic distortions and relaxor features [145, 150-152]. Initially, this relaxor state was termed an antiferroelectric state [20]; however, subsequent reports discarded antiferroelectricity in the system [153]. Based on the results from XRD, dielectric properties, and Raman spectroscopy analysis, Rout et al. [149] proposed a phase diagram for the BNT-ST system, as displayed in Figure 2.13. The phase boundary featured in the BNT-ST at room temperature is at 20 mol% ST, indicating the transformation from a rhombohedral to a pseudocubic phase, as previously indicated by changes in lattice parameter and unit cell distortion. This phase boundary was reported in other studies between 25 mol% ST and 28 mol% ST [21-23, 145, 150].

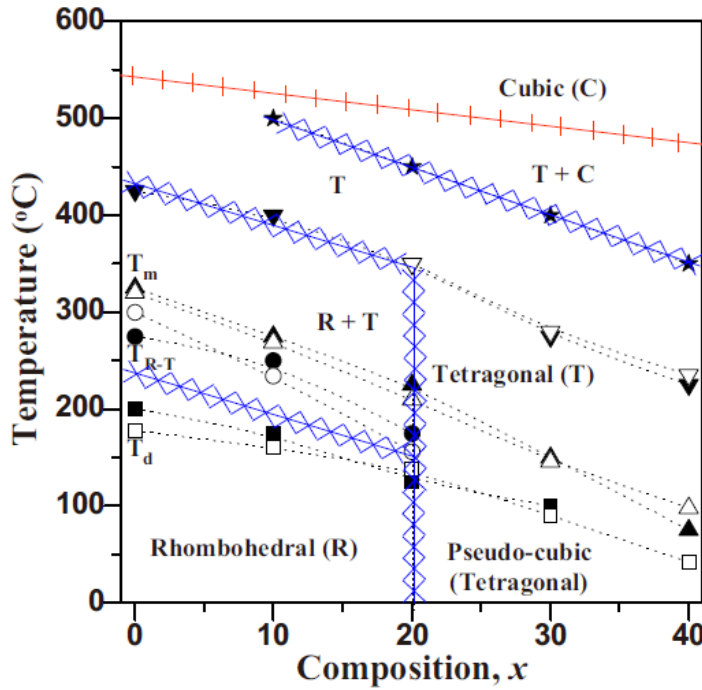


Figure 2.13: Binary phase diagram of the BNT-ST system from 0 mol% to 40 mol% ST. The symbols \square , \circ , and \triangle corresponds to T_d , T_{R-T} and T_m , respectively. Open symbols were obtained from dielectric measurements, while solid symbols from Raman spectroscopy analysis [149].

The phase boundary between the rhombohedral and the pseudocubic phases has a considerable effect on the electromechanical properties of the system. Hiruma et al. [21] reported the normalized strain d_{33}^* and piezoelectric constant d_{33} of the BNT-ST in a broad compositional range. The maximum piezoelectric constant $d_{33} = 130$ pC/N was reported to be around 22 mol% ST, followed by a decrease leading to negligible values above 28 mol% ST and maximized $d_{33}^* = 500$ pm/V at 6 kV/mm. In the meantime, Krauss et al. [145] observed the maximum strain of about 0.29% at 25 mol% ST and suggested to attribute it to a ferroelectric to antiferroelectric phase transition. Later, Duong et al. [22] revealed the the phase transition from non-ergodic to ergodic relaxor occurred at 26 mol% ST, and the highest strain under 4 kV/mm electric field, of 0.25% ($d_{33}^* \approx 620$ pm/V), was observed at 28 mol% ST. These results imply that the BNT-ST ceramics have the competitive advantage of larger strain under lower operating field compared with other BNT-based lead-free piezoelectric ceramics. Therefore, these ceramics are considered as promising candidates for actuator applications.

Chapter 3: Experimental Procedure and Characterization

3.1. Experimental Procedure

Processing of piezoelectric ceramics consists of oxides or carbonates powders to achieve the desired phase, compaction of powder to form a green body and then sintering to produce dense structure. The structural, microstructural, and electrical properties of ceramics strongly depend on their chemical composition, processing routes and fabrication techniques. In order to achieve greater performance and reliability of ceramics, it is very important to handle the compositions and processes parameters carefully. The two most ideally used methods to produce piezoelectric ceramic powders are sol gel processing and solid state reaction. Sol gel process is expensive; it produces very fine high purity powders which can sinter at much lower temperatures to achieve densities close to theoretical value. Solid state reaction is the most commonly used method due to its lower cost. In this thesis, solid state reaction method is used for the synthesis of piezoelectric ceramics. The experimental procedure and techniques used for the preparation and characterization of the ceramics in this study are described in this chapter.

3.1.1. Compositions

For ceramics specimens, four different systems were investigated:

- 1) The ternary $(0.99-x)\text{Bi}_{0.5}\text{Na}_{0.5}\text{TiO}_3-0.01\text{CaTiO}_3-x\text{SrTiO}_3$ ($x = 0.22, 0.24, 0.26, 0.28$ and 0.30)
- 2) The ternary $(0.78-x)\text{Bi}_{0.5}\text{Na}_{0.5}\text{TiO}_3-0.22\text{SrTiO}_3-x\text{BiAlO}_3$ ($x = 0; 0.01, 0.02$ and 0.03)
- 3) The ternary $(0.76-x)\text{Bi}_{0.5}\text{Na}_{0.5}\text{TiO}_3-0.24\text{SrTiO}_3-x\text{CaTiO}_3$ ($x = 0; 0.01, 0.02, 0.03$ and 0.04)
- 4) The ternary $(0.76-y)\text{Bi}_{0.5}\text{Na}_{0.5}\text{TiO}_3-0.24\text{SrTiO}_3-y\text{BaZrO}_3$ ($x = 0; 0.01, 0.02, 0.03$ and 0.04)

3.1.2. Raw materials

Commercially available reagent grade bismuth oxide, sodium carbonate, strontium carbonate, calcium carbonate, barium carbonate, zirconia oxide, aluminum oxide and titanium oxide were used as starting raw materials in the fabrication of the mentioned four systems. The details specifications of these powders are given in Table 3.1. These starting materials were first put in the oven at 100°C for 24 h to remove moisture, and then weighed according to their stoichiometric formulae.

Table 3.1: Raw materials used in the synthesis of ternary BNT-ST-based ceramics

| Chemical Name | Chemical formula | Purity | Particle (mesh) size | Source |
|---------------|------------------|--------|----------------------|--------|
|---------------|------------------|--------|----------------------|--------|

| | | | | |
|----------------------|--------------------------|-------|-------------------|-----------------------|
| Bismuth (III) Oxide | Bi_2O_3 | 99.9% | 0.2 μm | High Purity Chemicals |
| Sodium Carbonate | Na_2CO_3 | 99.9% | 20 mesh | High Purity Chemicals |
| Strontium Carbonate | SrCO_3 | 99.9% | - | High Purity Chemicals |
| Calcium Carbonate | CaCO_3 | 99% | - | High Purity Chemicals |
| Barium Carbonate | BaCO_3 | 99.9% | - | High Purity Chemicals |
| Titanium (IV) Oxide | TiO_2 | 99.9% | 0.2 μm | High Purity Chemicals |
| Zirconium (IV) Oxide | ZrO_2 | 99% | 0.1 μm | High Purity Chemicals |
| Aluminum (III) Oxide | Al_2O_3 | 99.9% | 0.1 μm | High Purity Chemicals |

3.1.3. Mixing and milling

After weighing the starting raw powders according to their stoichiometric formula, they were mixed and milled thoroughly inside a polyethylene jar with ZrO_2 balls (5-10 mm in diameter) as a mixing media and ethanol as solvent for 24 h, at the rate of 260 rpm. During milling process, when ball and ball or ball and jar wall collide, some amount of powder between them is repeatedly fractured, cold welded, flattened and rewelded, which reduce the particle size, and form uniform particles slurry. The wet slurry is then dried at 100°C for 24 h.

3.1.4. Calcinations

After proper mixing and milling, the dried milled powders were calcined at 850 oC temperatures in a closed alumina crucible with an indigenous programmable furnace. The powders were thoroughly grounded using mortar and passel and ball milled again to avoid glamorization of the particles. The pulverized powders were then used for the study of their phase formation as well as their reaction mechanism.

3.1.5. Pellet preparation

After calcinations, the powders were added with an organic binder polyvinyl alcohol (PVA, 5%). To get uniform and fined grain, the granules were passed through a 150 μm sieve. Pellets of 0.5g were made by using a cylindrical steal die of 12 mm in diameter. Initially the die was kept in a highly viscous mobile oil to prevent it from rousting. Taking out from the oil, the die was cleaned with isopropyl alcohol and acetone. Then the die containing the powder were uniaxially pressed with a pressure of 98 MPa in a hydraulic press.

Before releasing the pressure from the die, minimum 30 second time was given to minimize the stress on the pellet. Then the green pellets were then sintered to form the powders in bulk samples.

3.1.6. Sintering

Density of the electronic ceramics is a very sensitive parameter and that directly affects the material properties. Therefore, proper sintering of the pellets is essential for electrical property measurements. The pellets of the prepared compositions were put in alumina crucible and were taken into the furnace for sintering. The temperature was increased to 550 °C and maintained there for 2 h to remove all PVA binders and then increased at the rate of 5°C/min. To prevent Bi, and Na evaporation from the pellets, corresponding powders was used as an ambient, and sintered at 1175°C for 2 h in a programmable furnace. The pellets were furnace cooled and taken out of the furnace for density measurements.

3.1.7. Lapping and polishing

In order to make, fine smooth and flat surface for subsequent electrical property measurements lapping was carried out to obtained 0.5- and 1-mm thick specimens of the as sintered pellets by lapping machine (HRG-150E). The lapped pellets were then washed in acetone and polished with a sandpaper (cc 1000 cw) and then with an electric polishing machine (Dong ILT, 802-0408). The polished pellets were then thoroughly sonicated with acetone in ultrasonic machine (Branson, 5210) and dried at 100°C for 5 h.

3.1.8. Electrode application

The selection of suitable electrode for the test of materials is important to get a good response of the test material. Platinum (Pt) for dielectric and ferroelectric properties measurements and silver (Ag) electrodes for piezoelectric properties measurements were deposited on the opposite faces of the lapped and polished pellets by a dc sputtering and screen-printing techniques, respectively. The deposited electrodes were then fired at 500°C in case of Pt and 700°C in case of Ag for 20 min. Finally, silver wires were attached as terminal for electrical connections.

3.1.9. Poling

The piezoelectric materials are composed of randomly oriented domains, which possess identical structures but have a random orientation, resulting in a small or zero net spontaneous polarization. Therefore, it can be supposed that the properties of the ceramics are isotropic. The poling process is used to align the randomly oriented domains of piezoelectric materials. During this process, a high direct current electric field is applied to the material for a length of time. Through this polarizing (poling) treatment, domains most nearly aligned with the electric field. When the electric field is removed most of the dipoles are locked into a configuration of near alignment. In the present research, electroded pellets were poled at

4 kV/mm in a silicon oil bath at room temperature for 30 min, using a DC field high voltage power supply (Conver Tech, SHV30).

3.2. Structural characterization

3.2.1. Density Measurement

The densities of the as sintered ceramic pellets were determined by the Archimedes' immersion principal method using an electronic densimeter (SD-120L). The samples were weighed both in air and suspended in water. The density was calculated using the expression:

$$\rho = \frac{0.997 \times W_{dry}}{W_{dry} - (W_{wet} - W_{wire})} \quad 3.1$$

Where 0.997 is the density of water at room temperature, W_{dry} is the dry weight, W_{wet} is the weight of the sample and the wire suspended in water, and W_{wire} is the weight of the wire suspending the sample in the water.

3.2.2. X-Ray Diffraction Analysis

X-ray diffraction (XRD) technique is a powerful tool for material characterization as well as for detailed structural elucidation. As the physical properties of solids (e. g., electrical, optical, magnetic, ferroelectric, etc.) depend on atomic arrangements of materials, determination of the crystal structure is an indispensable part of the characterization of materials, mainly the identification of the chemical species. In the present study crystallographic and phase analyses were performed by an X-ray diffractometer (XRD RAD III, Rigaku, Japan) by using monochromatic $\text{CuK}\alpha$ radiation with the wavelength $\lambda_{\text{K}\alpha}=1.54178$ angstrom. The detection range was 20 to 80 degrees with a step size of 0.02° and a speed of $2^\circ/\text{min}$. The crystal parameters were calculated by using Bragg's law:

$$n\lambda = 2d\sin\theta \quad 3.2$$

$$\frac{1}{d^2} = \frac{h^2+k^2+l^2}{a^3} \quad 3.3$$

Where, a: crystal parameters for cubic structure

d: lattice spacing

h, k, l - lattice index

θ - diffraction angle

The volume percentage of perovskite phase in each composition was calculated using the following qualitative equation [154]:

$$\% \text{Perovskite} = \frac{(I_{100})_{\text{perov}}}{(I_{110})_{\text{perov}} + (I_{222})_{\text{perov}}} \times 100 \quad 3.4$$

where (I_{110}) and (I_{222}) are the major X-ray peak intensities for a perovskite phase and a pyrochlore phase, respectively.

The crystallite size of powders can be determined by measuring the Bragg peak width at half the maximum intensity and using the Scherer formula:

$$d_c = \frac{0.9\lambda}{B \cos \theta} \quad 3.5$$

where d_c is the crystallite size, λ is the wavelength of the X-radiation used, B is the peak width at half the maximum intensity (FWHM), and θ is the Bragg angle.

X-ray densities were calculated as suggested by B.D. Cullity [154]

$$\rho = \frac{\sum A}{NV} = \frac{1.66042 \sum A}{V} \quad 3.6$$

Where, ρ : X-ray density (g/cc), $\sum A$: Sum of the atomic weights of all the atoms in the unit cell, N : Avogadro's number, V : Volume of a unit cell. If the composition is of atomic weight A , then

$$A = \sum n_1 M \quad 3.7$$

Where, n_1 : number of molecules per unit cell and M : molecular weight.

The macroscopic density or the experimental bulk density of a particular specimen, determined from Archimedes principle is usually less and that cannot be exceeded the X-ray density, because the macroscopic specimen usually contains some cracks and pores.

3.2.3. Microstructural analysis

A scanning electron microscope (SEM) is a powerful microscope that uses electrons rather than light to form an image of objects such as fractured metal components, foreign particles and residues, polymers, electronic components, biological samples, and countless others. The shorter wavelength of electrons permits image magnifications of up to 100,000X, as compared to about 2,000X for conventional light microscopy. An SEM also provides a greater depth of field than a light microscope, allowing complex,

three-dimensional objects to remain sharp and in focus. This capability reveals details that cannot be resolved by light microscopy.

In this thesis work the microstructure was studied by SEM and field-emission electron microscope (FE-SEM, JEOL, JSM-650FF, Japan). Before the microstructural analysis, disc type samples were polished with silicon carbide and alumina polishing powders, thoroughly washed with acetone and then thermally etched at 1100°C for 1 h.

3.3. Electrical characterizations

The electrical properties were measured to investigate the effect of amount of ABO_3 on the BNT-ST ceramics. The following parameters were determined:

- 1) Dielectric properties (Dielectric constants and dielectric losses as a function of frequency and temperature)
- 2) Ferroelectric properties (Polarization (P) versus Electric field (E))
- 3) Piezoelectric coefficient (d_{33})
- 4) Electric field-induced strain (Strain (%) versus Electric field)

3.3.1. Dielectric properties

The room temperature relative dielectric permittivity ϵ_r and the dissipation factor ($\tan\delta$) were measured using the impedance grain phase analyzer (Hewlett Packard 4194A) with a working frequency range from 0.1 Hz to 40 MHz.

The temperature-dependent dielectric properties of both poled and unpoled specimens were determined using an impedance analyzer (HP4192A, USA) attached to a computer programmable electric furnace at different frequencies (0.1–10MHz) in temperature range 25 to 350°C under a heating and cooling rate of 2°C/min.

From the capacitance, the dielectric constant can be calculated using following equation:

$$\epsilon_r = \frac{\epsilon}{\epsilon_0} = \frac{Cd}{A\epsilon_0} \quad 3.8$$

Where, ϵ is the measured permittivity of the sample, ϵ_0 is the permittivity of the free space (8.85×10^{-12} F/m), C is the capacitance, d is the thickness of the sample, and A is the area of the electrode.

3.3.2. Piezoelectric coefficient (d_{33})

The piezoelectric coefficient (d_{33}) can easily be extract from the direct piezoelectric effect. The generation of charge (D_3) upon the application of an applied stress (σ_3). ($D_3 = d_{33}\sigma_3$). In this study, the piezoelectric coefficient d_{33} was measured using a Quasi-Static Piezo- d_{33} Meter (Model ZJ-6B, China). Prior to measure the piezoelectric coefficient, the samples were poled in silicon oil by applying an electric field of 4 kV/mm for 30 min. Finally, the piezoelectric coefficients were measured after 24 h of the poling

3.3.3. Ferroelectric properties

The easiest and most frequently used approach to measure the polarization hysteresis loop (P- E) is the simple Sawyer-Tower method. In this study, the ferroelectric hysteresis (P-E) loops were characterized by using a computer controlled modified Sawyer-Tower circuit. The modified Sawyer-Tower circuit were driven by a function generator (Agilent 33250A, USA) whose signal is amplified 1000 times by a high voltage amplifier (610, TREK Inc., Medina, NY, USA), which provides a maximum output voltage of 10 kV and a maximum output current of 2 mA. All data were recorded with an oscilloscope (Tektronix TDS1002, USA). During the polarization measurement, an electric field of 3-6 kV/cm was applied using a frequency of 0.5 Hz with amplified triangular waveform. To prevent the breakdown from the side area of the samples, samples were immersed in silicone oil during the measurements.

3.3.4. Electric field-induced strain measurement

The bipolar and unipolar electric field-induced stain was measured using a linear variable differential transducer (LVDT Mitutoyo MCH-331 & M401, Japan). The strain measurements were all done on Ag electrodes samples with a thickness of 1mm. The voltage was supplied by a high voltage amplifier (610, TREK Inc., Medina, NY, USA) driven by a function generator (Agilent 33250A, USA). Electric fields as high as 3-6 kV/cm was applied using a frequency of 0.5 Hz with amplified triangular waveform and all data was recorded with an oscilloscope (Tektronix TDS1002, USA). The normalized strain ($d_{33}^* = S_{max}/E_{max}$) was calculated as the ratio of the maximum strain (S_{max}) to the maximum electric field (E_{max}) in the unipolar strain-field curves. During testing, the samples were submerged into silicon to prevent it from breakdown.

Chapter 4: Result and Discussion

4.1. Effect of SrTiO₃ Modification on Dielectric, Phase Transition and Piezoelectric Properties of Lead-Free Bi_{0.5}Na_{0.5}TiO₃-CaTiO₃-SrTiO₃ Piezoelectric Ceramics

This work has been published in Journal of the Korean Ceramic Society in 2020 [155]

This study investigated the structures, dielectric, ferroelectric and piezoelectric properties of lead-free (0.99- x)Bi_{0.5}Na_{0.5}TiO₃-0.01CaTiO₃- x SrTiO₃ (BNT-CT-100 x ST, $x = 0.22 \sim 0.30$) piezoelectric ceramics. These piezoceramics were successfully prepared using the conventional solid-state reaction method sintered at 1175°C for 2h. It was found that a phase transition from nonergodic relaxor to ergodic relaxor was induced by ST modification in BNT-CT ceramics. Consequently, a large electromechanical strain of 0.20% corresponding to high normalized strain d_{33}^* of 667 pm/V was obtained even under 3 kV/mm for BNT-CT-28ST ceramics. Therefore, it is noted that lead-free BNT-CT-100 x ST ceramics can be promising candidates for actuator applications.

4.1.1. Introduction

Piezoelectric materials have attracted a great deal of attention for electronic devices, such as actuators, transducers and sensors, *etc.* The most widely used piezoelectric material are PbTiO₃-PbZrO₃ (PZT)-based component systems [4]. However, volatilization of toxic PbO during high temperature sintering not only causes environmental pollution, but also generates instability of composition and electrical properties of the final products. It is recently desired to use lead-free materials for environmental protection; and in many countries (European Union, Japan, Korea, etc.), the governments have encouraged the industry to remove lead from electric and electronic equipment [109, 156-158]. Accordingly, lead-free piezoelectric materials concerned with ceramics based on (K_{0.5}Na_{0.5})NbO₃ (KNN) and Bi_{1/2}Na_{1/2}TiO₃ (BNT) have been widely attracting attention to replace PZT ceramics [159-163].

Especially, Bi-based lead-free piezoceramics such as Bi_{1/2}Na_{1/2}TiO₃-BaTiO₃ (BNT-BT) or Bi_{1/2}Na_{1/2}TiO₃-Bi_{1/2}K_{1/2}TiO₃ (BNKT) materials have been considered as potential candidates for actuator applications because of their excellent electromechanical strain properties. Those bismuth-based materials possess a reversible phase transition between an ergodic relaxor state and a ferroelectric with the application of electric field that results in an abnormal electromechanical strain [19, 147, 164-167]. However, the required electric field to obtain large strain is twice as high as the field used to achieve maximum

polarization and strain in typical soft PZT system, which is one of the critical problem to be used in practical applications [19].

One material to overcome this problem is BNT–SrTiO₃ (BNT–ST) ceramics. This system was firstly reported by Sakata and Masuda [20]. It revealed that phase transition in BNT–ST system with respect to room temperature from rhombohedral to pseudo–cubic phase occurs around 20~25 mol% ST [149], accompanying with a considerable effect on the electromechanical properties. The maximum piezoelectric constant (d_{33}) value of 127 pC/N at around 24 mol% ST, followed by decreasing markedly d_{33} value to no piezoelectric response with more than 28 mol% ST, at which it exhibits a large strain reaching values of 0.29% at 6 kV/mm. This high strain is attributed to the reversible electric–field–induced phase transition between relaxor and ferroelectric phase [21]. Furthermore, many researchers are recently investigating BNT–ST ceramics with amount of ST around 25~26 mol% showed a very high strain ~0.26% at electric field as low as 4 kV/mm [22, 24, 168-170].

Besides, the effect of other alkaline-earth metal ion doping, such as Ca²⁺, on the electrical properties and phase transition behaviors of BNT ceramics were conducted by Watanabe *et al.*[171]. According to this study, Ca²⁺ substitution resulted in a decrease of the depolarization temperature (T_d) which seems to relate to the reduction of rhombohedral distortion in Ca-substituted BNT ceramics [171]. It was found that the rate of T_d dropped down to room temperature in the Ca–substituted BNT system was faster than that in the Sr–substitution, therefore, maximum values of piezoelectric properties could be obtained at a very small amount ~ 2 at% of Ca²⁺ substitution [171].

Recently, many studies have further improved the actuating performance by forming BNT–based ternary phase systems such as Bi_{0.5}Na_{0.5}TiO₃–KNbO₃–SrTiO₃ [172], Bi_{0.5}Na_{0.5}TiO₃–BaTiO₃–Sr₂MnSbO₆ [173], Bi_{0.5}Na_{0.5}TiO₃–SrTiO₃–LiNbO₃ [26], Bi_{0.5}Na_{0.5}TiO₃–BaTiO₃–Bi(Mn_{0.5}Ti_{0.5})O₃ [174] and so on. On the other hand, few research have been studied on piezoelectric properties and phase transition behavior of BNT–CT–based system[89, 175].

From these background, we tried to synthesize (0.99– x)Bi_{0.5}Na_{0.5}TiO₃–0.01CaTiO₃– x SrTiO₃ (BNT–CT–100 x ST) ceramics as a new BNT–based ternary system. This study systemically investigated the structures, dielectric and ferroelectric properties of BNT–CT–100 x ST ceramics.

4.1.2. Experimental Procedure

BNT–based lead–free piezoceramics with the compositions of BNT–CT–100 x ST ($x = 0.22, 0.24, 0.26, 0.28$ and 0.30) ceramics were prepared by a conventional solid–state reaction method. The component oxides and carbonates powders, Bi₂O₃ (99.9 %), TiO₂ (99.0 %), Na₂CO₃ (99.8 %), CaCO₃ and SrCO₃ (99.0

%), were used as raw materials (High Purity Chemicals, Japan). The raw materials were mixed in stoichiometric proportions by conventional ball milling treatment in ethanol using ZrO₂ balls, then dried and calcined at 850°C for 2h to form the uniform solid solution. The resultant powders were mixed with the polyvinyl alcohol (PVA) binder and then pressed into green discs with a diameter of 12 mm under a uniaxial pressure of 98 MPa. Finally, the pellets were placed in a sealed alumina crucible and sintered at 1175°C for 2 h.

The density of the sintered ceramics was measured by using Archimedes' immersion principle method using a digital densimeter (SD-120L, A&D, Japan). To determine relative density value, the theoretical density of each composition was calculated by using the formula:

$$\rho = \frac{\sum A_C + \sum A_A}{V_C \times N_A} \quad 4.1$$

Where, $\sum A_C$: the sum of the atomic weights of all cations in the formula unit, $\sum A_A$: the sum of the atomic weights of all anions in the formula unit, V_C : the unit cell volume, N_A : Avogadro's number.

The crystal structure was characterized with an X-ray diffractometer (XRD, RAD III, Rigaku, Japan) by using monochromatic CuK α radiation with the wavelength $\lambda = 1.54178 \text{ \AA}$. The polished and thermally etched surfaces of samples were imaged via Field-Emission Scanning Electron Microscopy (FE-SEM, JEOL JSM-650FF, USA) and the crystal structure was characterized with an X-ray diffractometer (XRD, RAD III, Rigaku, Japan). For electrical measurements, a silver paste was screen printed on both sides of specimens and subsequently burnt in at 700°C for 30 min. The polarization (P) and strain (S) hysteresis as a function of the external electric field (E) were measured with a piezoelectric measurement system (aixACCT aixPES, Aachen, Germany). The temperature-dependent dielectric constant (ϵ_r) and dielectric loss ($\tan \delta$) of the BNT-CT-100xST ceramics were carried out at a heating rate of 5°C/min in a temperature-regulated chamber connected to a precision LCR meter (E4980AL, Keysight, USA) at 1, 10, and 100 kHz.

4.1.3. Results and Discussion

The linear shrinkage and relative density values of BNT-CT-100xST ceramics as a function of ST content are displayed in Figure 4.1. All samples exhibited around 15% values of linear shrinkage and high relative densities reached over 97%. These results indicate that the sintering temperature at 1175°C is suitable for densification of BNT-CT-100xST ceramics regardless of ST modification.

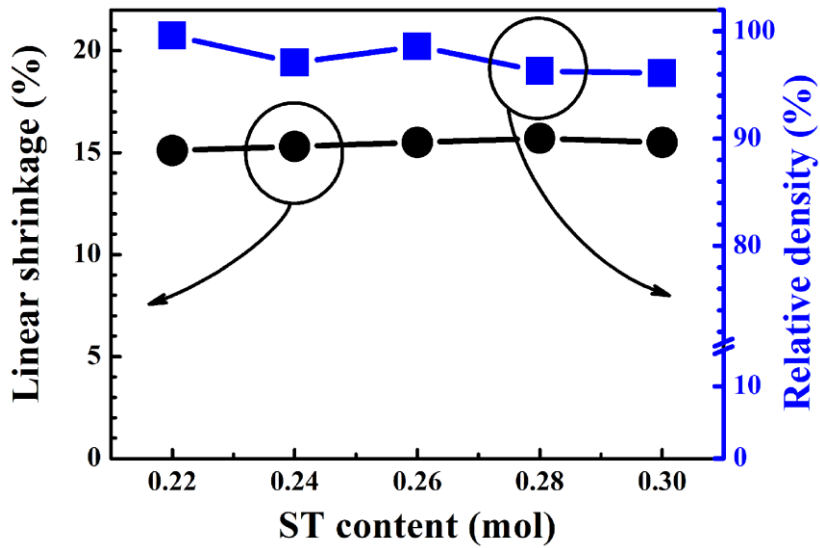


Figure 4.1: Linear shrinkage and relative density values of BNT–CT–100xST ceramics as a function of ST content

FE–SEM images of BNT–CT–100xST ceramics display in Figure 4.2. All images revealed dense microstructures, which is consistent with behaviors of relative densities for BNT–CT–100xST ceramics as can be seen in Figure 4.1. The average grain size values were determined by the linear intercept method that were decreased with increasing ST content. The largest AGS was $9.42 \pm 1.19 \mu\text{m}$ for BNT–CT–22ST ceramics and the smallest AGS was $5.48 \pm 0.62 \mu\text{m}$ for the BNT–CT–30ST ceramics. The changes are consistent with previous results in the microstructures of ST–modified BNT–based ceramics [22, 145], which seems to be closely related to the thermodynamic behaviors of the synthesized materials and diffusion behavior of Sr [23, 176]. In fact, it was reported that the temperatures required for the formations of BNT and ST phases start at around 530°C and 560°C , respectively [177, 178]. For detail, at 530°C BNT phase is formed due to the decomposition of Na_2CO_3 and its reaction with Bi_2O_3 and TiO_2 . The densification of BNT phase structure goes on with subsequent Sr^{2+} diffusion from decomposing SrCO_3 [23]. It is noticed that the transport of Sr^{2+} occurs along grain boundaries rather than through the BNT phase [176]. The development of ST mainly at grain boundary results in the formation of core-shell structure [23, 176]; in our present work, it is possibly the cause of preventing grain growth in BNT–ST systems. Therefore, the different reaction temperatures of two materials are suggested to be the origin of the decreased grain size with increasing the ST doping level.

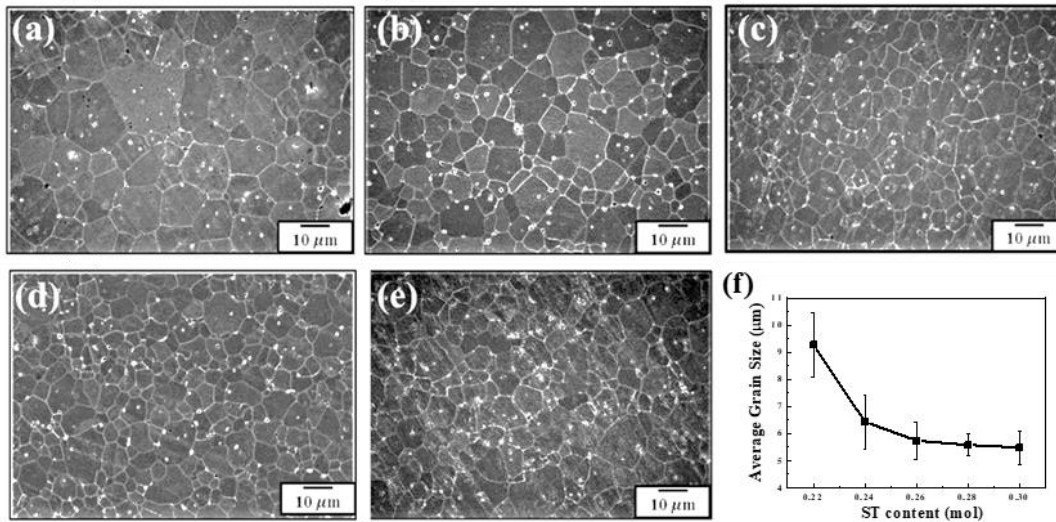


Figure 4.2: FE-SEM images of polished and thermally etched BNT-CT-100xST ceramics, (a) $x = 0.22$, (b) $x = 0.24$, (c) $x = 0.26$, (d) $x = 0.28$, (e) $x = 0.30$ and (f) the average grain size as a function of ST content

Figure 4.3 presents XRD patterns of BNT-CT-100xST ceramics at room temperature. In Figure 4.3, all samples exhibited single perovskite phases, demonstrating that a uniform solid solution was formed. From Figure 4.3(b) and (c), the BNT-CT-100xST ceramics showed a single cubic perovskite structure as evidence by no peaks splitting in ranges of 39.7° - 40.3° and 45.9° - 47.1° except for $K\alpha_2$ peaks. It indicates that all compositions can be categorized as the relaxor materials [179, 180]. Besides, the lattice parameters were increased with increasing the ST content as evidenced by shifting to lower angle of (111) and (002) peaks. The reason for this change is that the ionic radius of Sr^{2+} (1.32 \AA) is bigger than the averaged A-site ionic radius of BNT-CT (Bi^{3+} : 1.17 \AA , Na^{1+} : 1.16 \AA and Ca^{2+} : 1.00 \AA) [171]. This result implies that the modified ST does not affect the crystal structure change in BNT-CT system, which is well matched with other BNT-based lead-free relaxor materials [181-185].

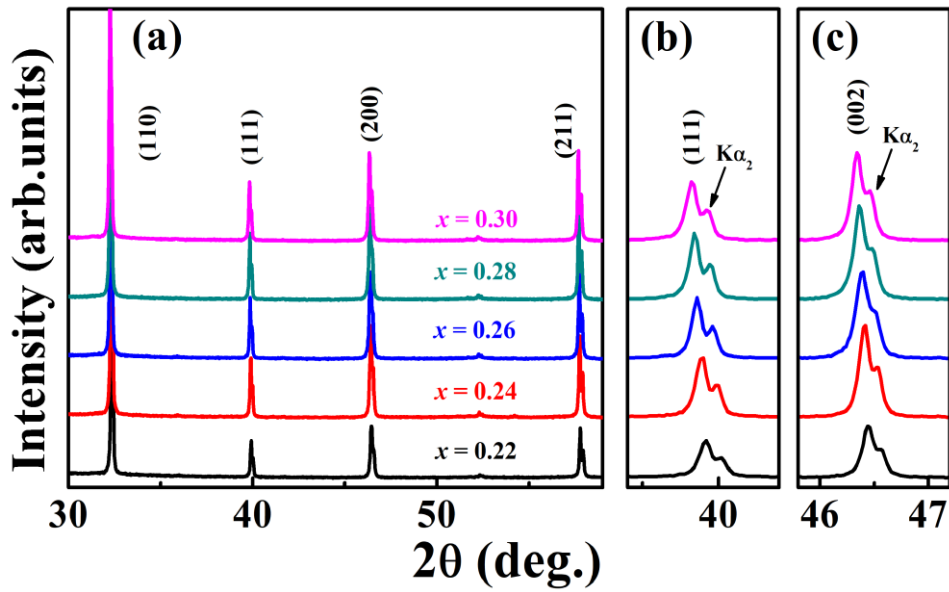


Figure 4.3: X-ray diffraction patterns of BNT–CT–100 x ST ceramics as a function of ST content, (a) 20–60°, (b) 39.5–41.5°, and (c) 46.5–47.5°

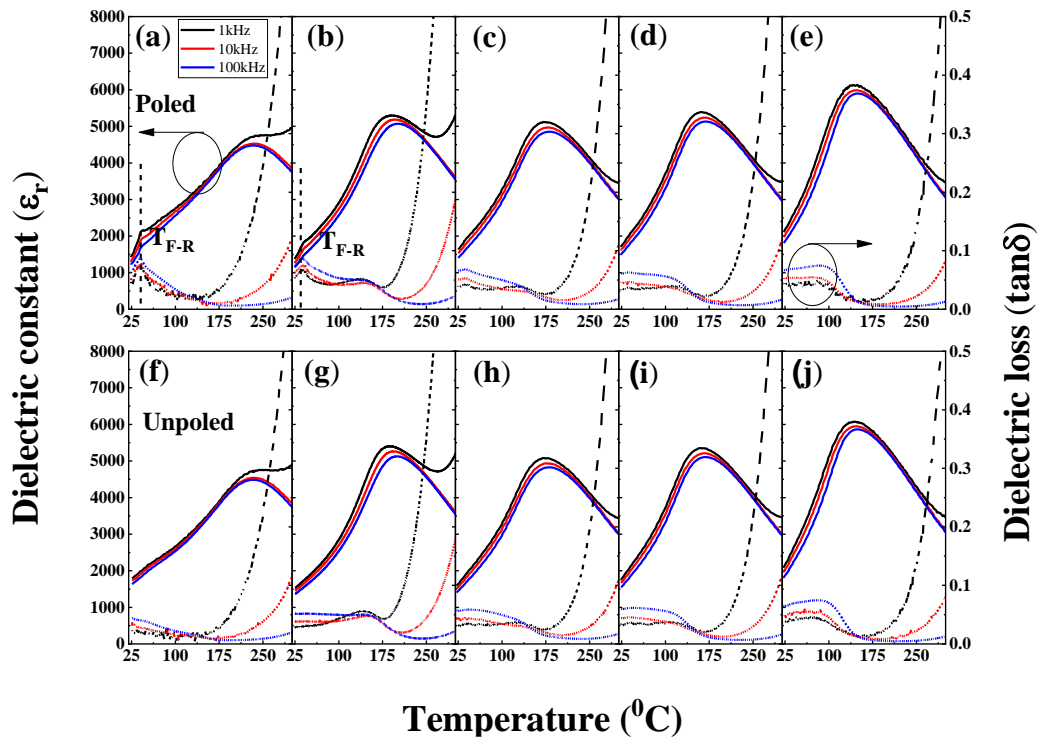


Figure 4.4: Temperature–dependent dielectric constant (ϵ_r) and dielectric loss ($\tan \delta$) for the poled (top) and unpoled (bottom) BNT–CT–100 x ST ceramics as a function of ST content, (a) and (f) $x = 0.22$, (b) and (g) $x = 0.24$, (c) and (h) $x = 0.26$, (d) and (i) $x = 0.28$, (e) and (j) $x = 0.30$

Figure 4.4 shows the temperature dependence of dielectric constant (ϵ_r) and dielectric loss ($\tan \delta$) for both unpoled and poled BNT-CT-100xST ceramics with three measurement frequencies of 1, 10 and 100 kHz. All the poled and unpoled specimens showed a strong frequency dispersion and broadened peaks in dielectric spectra, implying that BNT-CT-100xST ceramics can be categorized as relaxors. Furthermore, poled BNT-CT-22ST ceramics revealed two abnormal peaks. The first one is referred to as T_m , which denotes the temperature giving the maximum dielectric constant. As shown in Figure 4.4, with increasing ST content, T_m shifted toward lower temperatures from 230°C for BNT-CT-22ST ceramics to 142°C for BNT-CT-30ST ceramics which is consistent with observations reported in previous studies [21, 22, 145, 186]. The second anomaly peak located at the lower temperature region corresponds to T_{F-R} (the ferroelectric-to-relaxor transition temperature), where the electric-field-induced long-range order breaks down into a short-range one [131, 180]. This result shows that BNT-CT-22ST ceramics is a nonergodic relaxor (NER) at low temperature. We should note that the determination of T_{F-R} is only valid for poled specimens [166, 179, 181, 182]. It is also seen that T_{F-R} decreased from $\sim 40^\circ\text{C}$ for BNT-CT-22ST ceramics to $\sim 30^\circ\text{C}$ for BNT-CT-24ST ceramics and then was not detectable for the compositions with higher ST contents. The absence of apparent T_{F-R} for poled BNT-CT-100xST ceramics with $x \geq 0.26$ in the range measurement data was an indication that lowering of T_{F-R} below the room temperature. This implies that those specimens were ergodic relaxors (ER), in which the field-induced changes were recovered back to their initial state on removal of the electric field at the room temperature [49].

The polarization (P - E) and bipolar strain (S - E) curves of BNT-CT-100xST at the applied electric fields of 4 kV/mm are depicted in Figure 4.5. Typical ferroelectric hysteresis curves, represented by square-type polarization and butterfly-shaped strain hysteresis, were observed for BNT-CT-22ST and BNT-CT-24ST ceramics. As discussed above in reference to Figure 4.4, those two compositions are NER relaxor at room temperature with microscopic cubic structures at zero electric field. When an electric field is applied to the NER materials, it can transform irreversibly into a ferroelectric state [187-189]. Therefore, we can observe the square-shaped P - E curves with butterfly-shaped strain curves of BNT-CT-22ST and BNT-CT-24ST ceramics. A further increase in ST modification led to drastic decreases in remanent polarizations (P_r), coercive fields (E_C) with double hysteresis P - E curves and large strains. The changes in polarization and strain curves such as the drastically decreased E_C , P_r , negative strain (S_{neg}), and increased maximum strain (S_{max}) for $x = 0.28$ ceramics can be categorized an incipient piezoceramics as ER [19]. In fact, those large strains are observed in other BNT-based relaxor materials, which are originated from the reversible transition into a ferroelectric state [181-185].

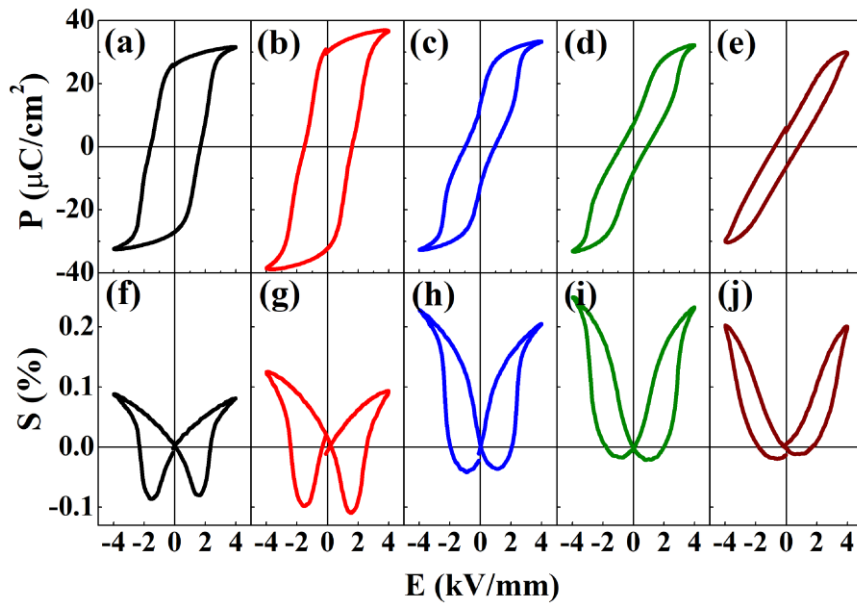


Figure 4.5: Polarization (top) and bipolar strain curves (bottom) for BNT-CT-100xST ceramics as a function of ST content, (a) and (f) $x = 0.22$, (b) and (g) $x = 0.24$, (c) and (h) $x = 0.26$, (d) and (i) $x = 0.28$, (e) and (j) $x = 0.30$

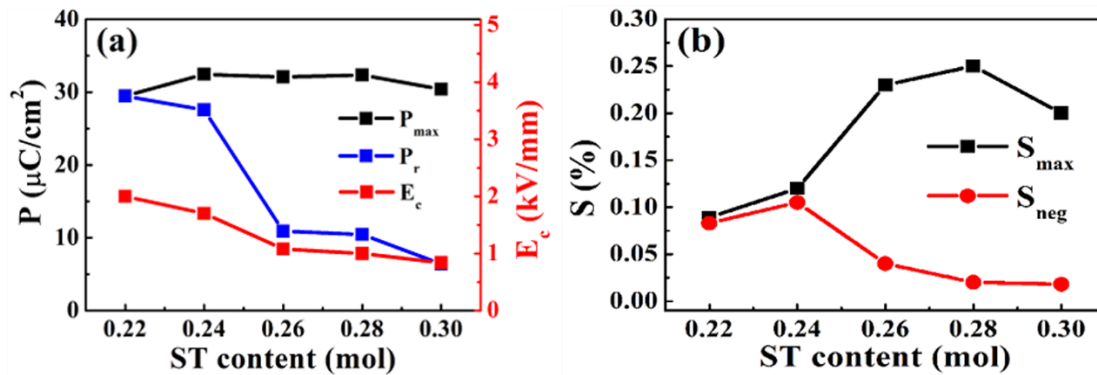


Figure 4.6: Variation of (a) E_c , P_r , and (b) S_{max} , S_{neg} of BNT-CT-100xST ceramics as a function of ST content

For better understanding effects of ST modification, characteristic parameters such as E_c , P_r , maximum polarization (P_{max}), S_{max} , and S_{neg} were extracted from Figure 4.5 and are plotted in Figure 4.6. The ferroelectric BNT-CT-24ST ceramics showed good P_r and E_c around $30.9 \mu\text{C}/\text{cm}^2$ and $1.56 \text{ kV}/\text{mm}$, respectively. However, when the ST content increased those values decreased drastically with strongly pinched P - E curves. Therefore, P_r and E_c reached minimum values as $5.32 \mu\text{C}/\text{cm}^2$ and $0.68 \text{ kV}/\text{mm}$ when

the modification level of ST was 30 mol%. On the other hand, P_{\max} values for BNT–CT–100 x ST ceramics were changed slightly with increasing ST modification. These results in P – E curves imply that FE–to–RE phase transition in BNT–CT–100 x ST ceramics was induced by ST modification. The values of S_{\max} increased with increasing x from 0.22 to 0.28, and then decreased with further increases in ST content. BNT–CT–28ST ceramics showed the highest S_{\max} under the applied electric field of 4 kV/mm of 0.25%.

The unipolar strain curves are plotted in Figure 4.7 with applying electric field as 3 and 4 kV/mm. BNT–CT–22ST and BNT–CT–24ST ceramics exhibited linear unipolar strain curves which are categorized as stabilized FE compositions. On the other hand, with further increases in the ST content, the strain value increased drastically with getting larger hysteresis for $0.24 < x < 0.30$, and then was declined in BNT–CT–30ST ceramics. We obtained the largest strain properties in BNT–CT–28ST ceramics regardless of applied electric fields, which gave the maximum strain of 0.20 % and 0.24% under 3 and 4 kV/mm, respectively. This large unipolar strain is attributed to the ferroelectric–to–relaxor phase transition induced by ST modification that was originated from the interrupted long–range ferroelectric order [131, 180].

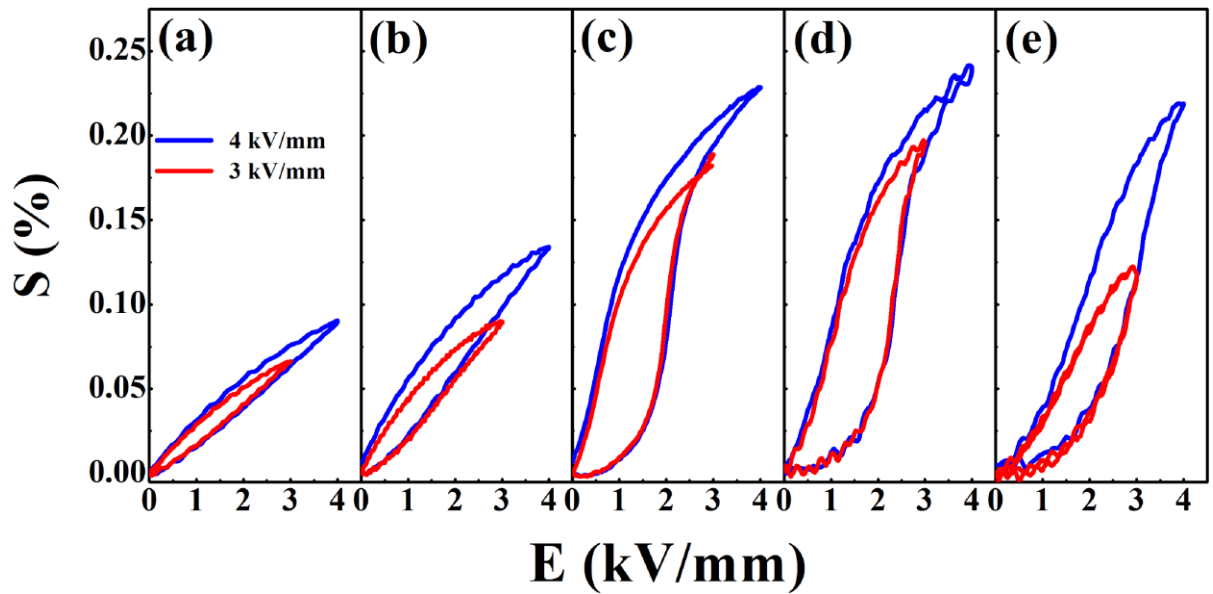


Figure 4.7: Unipolar strain curves for BNT–CT–100 x ST ceramics as a function of ST content.

To confirm the achievement of this study, the characteristic parameters such as the S_{\max} , applied electric field (E_{\max}), and the normalized strain (d_{33}^*) were extracted and calculated from Figure 4.7, which were compared with other piezoceramics in Table 4.1. From previous studies, many high d_{33}^* values of lead–free ceramics had been reported for BNT–BKT–ST5 (600 pm/V) [180], Nb–doped BNKT (641 pm/V) [111], and BNT–BT–KNN2 (560 pm/V) [42]. However, those ceramics required relatively strong electric fields

(around 6 to 8 kV/mm as E_{max}) to obtain large strains, which is a drawback for practical applications mentioned above. In our work, a decrease of the driving field from 6 kV/mm to 3 kV/mm could be obtained for BNT–CT–26ST and BNT–CT–28ST. Furthermore, by utilizing the BNT–CT–ST ternary ceramics, the field–induced–strain behaviors have been improved upon BNT–ST binary materials. For detailed, BNT–CT–28ST ceramics showed the large d_{33}^* value of 667 pm/V, which is higher than 625 pm/V of BNT–28ST [22]. In fact, the main reason for the relatively enhanced strain of this system is unclear yet. However, it found that some difference between polarization and strain curves in BNT–CT–ST ceramics as this study and in BNT–28ST ceramics [22]. There were two facts that one was obtained a relatively broader polarization hysteresis and the other was observed a relatively deeper and larger S_{neg} in comparison to BNT–28ST²⁴⁾ ceramics. From these results, we may assume that the induced nonergodicities by added CT are responsible for relatively enhancing strain properties of BNT–CT–ST ceramics in comparison to BNT–28ST ceramics [26, 179]. To clarify this assumption, it is obviously needed further study. This method could be compared with the relaxor/ferroelectric composite approaches which are recently considered as good techniques for obtaining high low–field induced strain properties [190–192]. Therefore, we believe that BNT–CT–100xST ceramics are promising candidates for actuator applications.

Table 4.1: Comparison of normalized strains d_{33}^* (S_{max}/E_{max}) between this study and other BNT–based lead–free piezoceramics

| Material | S_{max} (%) | E_{max} (kV/mm) | d_{33}^* (pm/V) | References |
|---------------------|---------------|----------------------|----------------------|------------|
| BNT–CT–26ST | 0.185 | 3 | 617 | This work |
| BNT–CT–28ST | 0.20 | 3 | 667 | This work |
| 25ST | 0.24 | 4 | 600 | [24] |
| BNT–28ST | 0.25 | 4 | 625 | [22] |
| BNST28 | 0.29 | 6 | 488 | [21] |
| BNT–BKT–ST5 | 0.36 | 6 | 600 | [180] |
| Nb–doped BNKT | 0.45 | 7 | 641 | [111] |
| BNT–BT–KNN2 | 0.45 | 8 | 560 | [42] |
| 0.93BNKT–0.07BA/BNT | 0.29 | 4 | 725 | [190] |
| 2LF/1.5SN | 0.298 | 4 | 745 | [191] |
| BNKT–0.04BMT/1.5BNT | 0.14 | 2.5 | 560 | [192] |

4.1.4. Summary

The effect of a ST modifier on the crystal structure and electromechanical properties of $(0.99-x)\text{Bi}_{0.5}\text{Na}_{0.5}\text{TiO}_3-0.01\text{CaTiO}_3-x\text{SrTiO}_3$ ceramics were investigated. The results showed that as the ST content was increased, a phase transition from NER to ER occurred in the system. The addition of ST shifted the $T_{\text{F-R}}$ to a lower temperature and destabilized the ferroelectric order resulted in the degradation of remnant polarization, coercive field, and negative strain, which was accompanied by a large electric-field-induced strain of 0.20% and a high normalized strain of $d_{33}^* = 667$ pm/V under a low applied electric field of 3 kV/mm for BNT-CT-28ST ceramics. These results indicated that BNT-CT-100xST can be a promising candidate for actuator application.

4.2. Large Electric Field-induced Strain Response under a Low Electric Field in Lead-free $\text{Bi}_{1/2}\text{Na}_{1/2}\text{TiO}_3\text{-SrTiO}_3\text{-BiAlO}_3$ Ternary Piezoelectric Ceramics

This work has been published in Journal of Electronic Materials in 2020 [193]

Bismuth-based lead-free ceramics are some of the most promising candidates for actuator applications due to their large strain response. Despite the large strains in bismuth-based piezoelectric ceramics, there still remain challenges regarding their utilization in practical applications. For instance, a relatively high operating field is required to obtain the large strain properties. In this work, lead-free $\text{Bi}_{1/2}\text{Na}_{1/2}\text{TiO}_3\text{-SrTiO}_3\text{-BiAlO}_3$ (BNT-ST-BA) ternary piezoelectric ceramics are proposed as materials that could enhance the electromechanical strain performance under low driving field. We found that the highest normalized strain d_{33}^* value of 707 pm/V was achieved at a relatively low electric field of 3 kV/mm from 2 mol% BA-modified BNT-ST ceramics. We suggest that the naturally induced nonergodicities in the ergodic relaxor generate internal stress. This induced internal stress is responsible for the excellent strain properties of this material. We believe that the materials synthesized in this study are promising candidates for actuator applications.

4.2.1. Introduction

Lead-based piezoelectric materials, such as lead zirconate titanate (PZT), are widely used in electrical devices such as piezoelectric actuators, sensors, and transducers due to the excellent electromechanical properties of these materials [4]. However, it is well known that lead (Pb) is toxic and can damage the human body and the environment [194]. Accordingly, many countries have encouraged academic and industrial researchers to replace these materials with lead-free piezoelectric materials [158]. Recently, $(\text{K}_{0.5}\text{Na}_{0.5})\text{NbO}_3$ (KNN)- and $\text{Bi}_{1/2}\text{Na}_{1/2}\text{TiO}_3$ (BNT)-based lead-free piezoelectric materials have attracted wide-spread attention as promising candidates to replace PZT ceramics [159-163, 195-200]. $(\text{Bi}_{1/2}\text{Na}_{1/2})\text{TiO}_3$ (BNT)-based ceramics are of particular interest for actuator applications because of their excellent electromechanical strain properties [147, 165-167, 201-203]. It is understood that the large electromechanical strain (referred to as incipient piezoelectricity) in BNT-based ceramics originates from a reversible electric field-induced phase transition from an ergodic relaxor (ER) phase to a ferroelectric via application of an electric field [19, 182, 204, 205]. However, high electric fields are normally required to obtain large electromechanical strain properties in these incipient piezoceramics. Such high required fields present challenges to the utilization of BNT-based lead-free incipient piezoceramics in practical applications [19].

To overcome this problem, many scientists have pursued methods to decrease the required electric field. For instance, formation of ferroelectric/relaxor ceramic composites was suggested and successfully demonstrated to enhance strain properties under low electric field. The constructed ferroelectric/relaxor composites in $\text{Bi}_{1/2}(\text{Na,K})_{1/2}\text{TiO}_3\text{-BaTiO}_3$ (BNKT-BT) systems decreased the driving field from 6 kV/mm to 4 kV/mm with a high strain of 0.25%, as first reported by Lee *et al.*[190]. Since then, many studies have demonstrated reduction of the driving field in BNT-based incipient piezoceramics by using ferroelectric/relaxor composites [49, 190, 204, 206]. Additionally, BNT-SrTiO₃ (BNT-ST)-based ceramics have also been shown to be promising materials with lower electric field requirements. It has been reported that $(1-x)\text{BNT-xSrTiO}_3$ ceramics undergo a phase transition from a nonergodic relaxor (NER) to an ER for $x \approx 0.26$ with a large strain of about 0.25% under 4 kV/mm [22-24]. It has been suggested that the naturally formed core-shell structure (core and shell regions are comprised of ferroelectrics and relaxor, respectively) in BNT-ST ceramics is responsible for these improved strain properties [23, 24, 168]. Accordingly, it is noted that intentionally or naturally induced ferroelectricities (or nonergodicities) in BNT-based incipient piezoceramics play an important role for improving electromechanical strain properties with a low operating field. Furthermore, it has been suggested that new ternary systems based on BNT-ST ceramics may be a good approach for improving the electromechanical performance in BNT-ST piezoelectric ceramics. Zhu *et al.*[25] have reported that a large strain of 0.27% at 4 kV/mm was obtained by incorporating 1 mol% AgNbO_3 (AN) into BNT-ST piezoelectric ceramics. Furthermore, Hong *et al.*[26] investigated the effect of LiNbO_3 modification on the electrical properties in BNT-ST piezoelectric ceramics and obtained a large strain of 0.246% at 4 kV/mm with a normalized strain of 616 pm/V.

BiAlO_3 (BA) possesses a rhombohedral perovskite structure at room temperature and has recently attracted great attention due to its excellent ferroelectric properties with a large polarization of 76 $\mu\text{C}/\text{cm}^2$ [25]. Therefore, BA modification in BNT-ST ceramics is expected to improve electromechanical strain properties, as has in fact been reported by Ullah *et al.*[207, 208]. This study showed that a very large strain of 0.35% at an electric field of 6 kV/mm could be observed for compositions with 3 mol% BA, which forms a morphotropic phase boundary between tetragonal and pseudo cubic phases in BNKT ceramics [207]. Recently, it has been noted that the introduction of BA into $\text{Bi}_{0.5}\text{Na}_{0.5}\text{TiO}_3\text{-BaTiO}_3$ (BNT-BT) resulted in lowering the phase transition from ferroelectric to relaxor phase to below room temperature and lead to a large strain response of ~0.37% with normalized strain $S_{\text{max}}/E_{\text{max}}$ of 533 pm/V [209]. Therefore, it is reasonable to propose that the combination of BNT-ST as a host material and BA as a modifier could be a promising method to achieve large strain responses under the low driving field in lead-free material.

Accordingly, we synthesized lead-free BNT-ST-BA ternary piezoelectric ceramics and systemically investigated the effect of BA modification on the structural, dielectric, and electromechanical strain properties. We obtained improved electromechanical strain properties with relatively low operating field ($d_{33}^* = 707$ pm/V at 3 kV/mm) with 2 mol% BA-modified lead-free BNT-ST ternary piezoelectric ceramics, which is comparable with other materials. We suggest that the naturally induced nonergodicity in the ER state is responsible for these improved electromechanical strain properties in lead-free BNT-ST-BA ternary piezoelectric ceramics. These results suggest that lead-free BNT-ST-BA ternary piezoelectric ceramics are promising candidates to replace lead-based material in practical applications.

4.2.2. Experiment procedure

All ceramic samples were synthesized via conventional solid-state methods. The raw materials of Bi_2O_3 (99.99%), Na_2CO_3 (99.0%), TiO_2 (99.99%), SrCO_3 (99.9%), and Al_2CO_3 (99.9%), were weighed according to the desired chemical composition $(0.78-x)\text{Bi}_{1/2}\text{Na}_{1/2}\text{TiO}_3-0.22\text{SrTiO}_3-x\text{BiAlO}_3$ (BNT-ST-100xBA) for $x = 0, 0.01, 0.02, \text{ or } 0.03$. The weighed powders were mixed by ball milling for 24 h in ethanol using ZrO_2 balls. The wet slurry was dried at 100 °C for 24 h in a dry oven. After proper mixing and crushing with milling, the powders were calcined at 850 °C for 2 h with a heating rate of 5 °C/min in a furnace. Then, the calcined powders were ball milled again for 24 h. After drying, polyvinyl alcohol solution (PVA) was added to the prepared powders as a binder. Subsequently, the powders were pressed into small disks of 12 mm diameter under a 98 MPa linear compressor. Finally, the pellets were sintered in covered alumina crucibles at 1175 °C for 2 h with a heating rate of 5 °C/min in a furnace with an air environment.

The density values for all sintered samples were measured using an electronic densimeter (SD-120 L, A&D, Japan) using Archimedes' immersion principle. The crystal structures were observed using X-ray diffraction (XRD, Ultima, Rigaku, Japan) with Cu radiation. The microstructure was identified using SEM and field-emission electron microscope (FE-SEM, JSM-650FF, JEOL Japan). The electrical measurements were carried out after screen-printing a silver paste on both sides of the disc-shaped samples and subsequent firing at 700 °C for 30 min. All samples were poled in a silicone oil bath at room temperature under a direct current (DC) field of 4 kV/mm for 15 min. Temperature- and frequency-dependent permittivity and dielectric loss for poled and unpoled samples were recorded using a high temperature electric prober system (KEYSIGHT-E4980AL Precision LCR Meter, USA). The electric-field-induced polarization (P - E) and strain curves (S - E) for all samples were carried out at 1 Hz in a silicon oil bath using a modified Sawyer-Tower circuit and a linear variable differential transducer (LVDT, Mitutoyo MCH-331 & M401).

4.2.3. Result and discussion

Figure 4.8 presents images of the polished and thermally etched surfaces of the BNT–ST–100xBA ceramics along with corresponding relative densities. All microstructure images of the samples exhibited similar grain morphologies and dense microstructures, with linear shrinkage of approximately 16% and relative densities of over 97%, regardless of BA modification. These results indicate that 1175 °C is a suitable sintering temperature for BNT–ST–100xBA ceramics. In contrast, the average grain size (AGS) of the samples were strongly influenced by BA content. The calculated AGS value of the BNT–ST–0BA ceramics was about 5.92 μm , which drastically decreased to 1.84 μm in the BNT–ST–3BA ceramics.

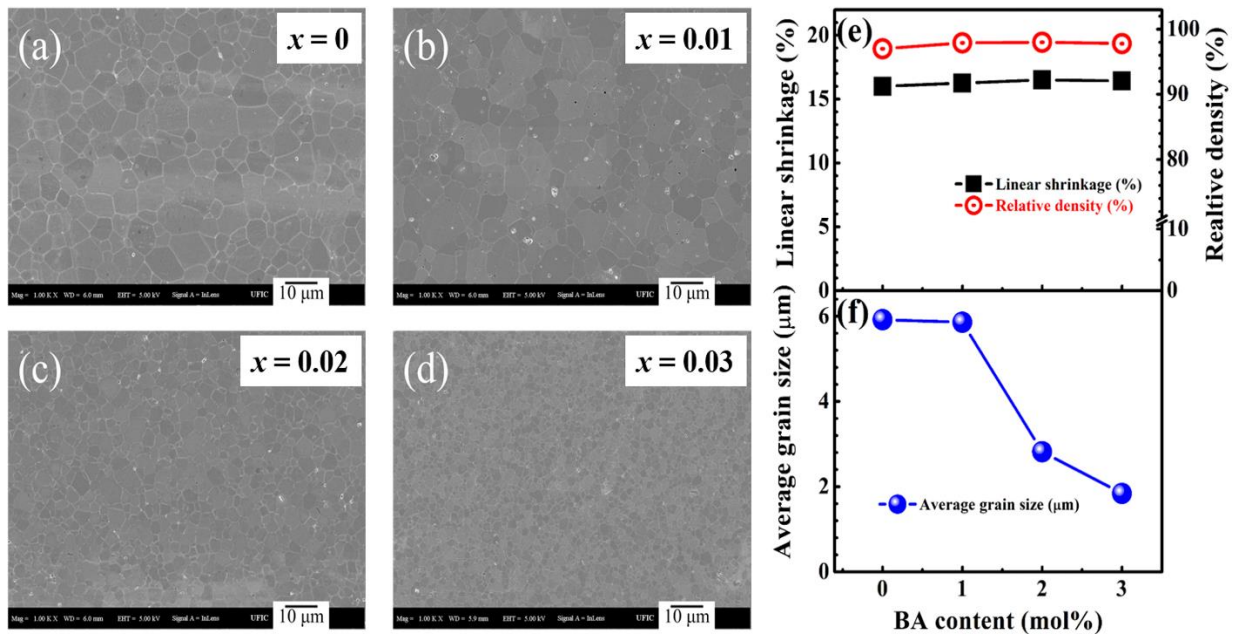


Figure 4.8 FE-SEM images of the polished and thermally etched surfaces of (a) BNT–ST–0BA, (b) BNT–ST–1BA, (c) BNT–ST–2BA, and (d) BNT–ST–3BA ceramics. Changes to (e) linear shrinkage and relative density and (f) the average grain size of the BNT–ST–100xBA ceramics as a function of BA content.

The XRD patterns in the 2θ range of $30\text{--}60^\circ$ of the BNT–ST–100xBA ceramics are displayed in Figure 4.9(a). We obtained a single perovskite structure without any secondary phase in all samples. This result indicates that Al^{3+} ions completely diffused into the B–sites of BNT–ST ceramics. To clarify the effect of BA modification on crystal structure in the BNT–ST ceramics, the detailed XRD patterns corresponding to 2θ ranges of $39.5\text{--}40.5^\circ$ and $45.8\text{--}47.2^\circ$ are shown in Figure 4.9(b) and (c), respectively. All BNT–ST–100xBA ceramics exhibited a single cubic structure, which is evidenced by no peak splitting, except for

$K\alpha_2$ peaks. This data indicates that the crystal structure of BNT–ST ceramics is feebly influenced by BA modification.

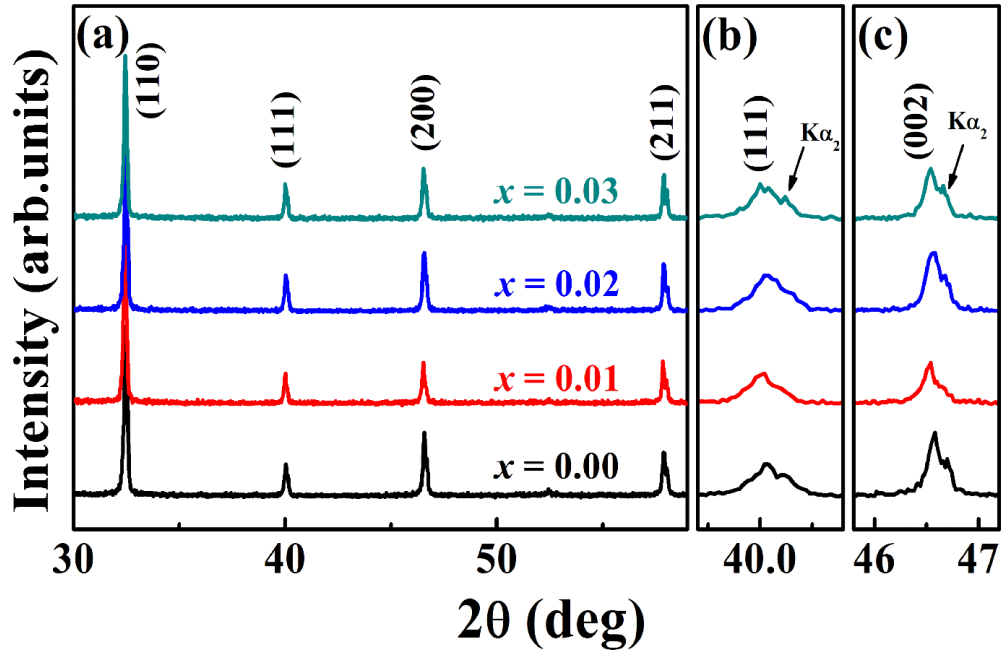


Figure 4.9: X–ray diffraction (XRD) patterns of BNT–ST–100xBA ceramics as a function of BA content in the 2θ ranges of (a) $30\text{--}60^\circ$, (b) $39.5\text{--}40.5^\circ$ and (c) $45.8\text{--}47.2^\circ$.

Figure 4.10 depicts the temperature dependence of the dielectric constant (ϵ_r) and dielectric loss ($\tan \delta$) of the poled and unpoled BNT–ST–100xBA ceramics. All BNT–ST–100xBA ceramics were categorized as relaxor, as evidenced by the strong frequency–dependent dispersions from room temperature to around 200°C and broad, diffuse peaks at the temperature of the dielectric maxima (T_m). In the case of BNT–ST–0BA and BNT–ST–1BA ceramics, abnormal peaks in both the dielectric constant and loss curves were observed in the lower temperature region of the poled samples. These anomalies are associated with the ferroelectric to relaxor transition temperature (T_{F-R}) that emerges from disassociation of long-range ordered ferroelectrics (or polarized ferroelectrics converting to relaxor) by thermal stimulation [19, 181]. With increasing BA content, the T_{F-R} decreased from 49°C for BNT–ST–0BA ceramics to around 29°C for BNT–ST–1BA ceramics, then either vanished or shifted to below room temperature. Accordingly, we can suggest that BNT–ST–0BA and BNT–ST–1BA ceramics are NER at the low temperature, while BNT–ST–2BA and BNT–ST–3BA ceramics can be categorized as ER at room temperature ($\sim 25^\circ\text{C}$). Therefore, these results imply that the stabilized NER of BNT–ST–0BA ceramics undergoes a phase transition from a NER (or ferroelectrics) to an ER as BA is added.

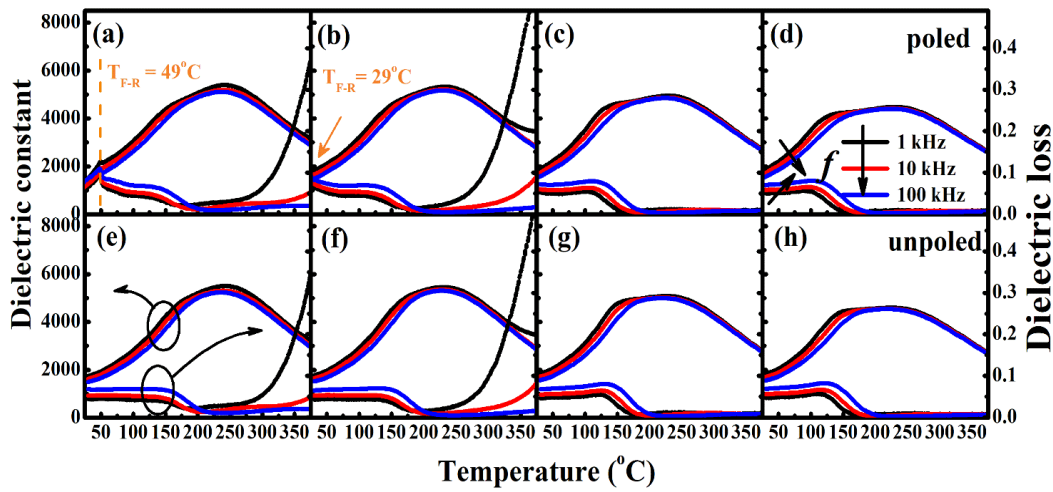


Figure 4.10: Temperature dependence of dielectric constant (ϵ_r) and dielectric loss ($\tan \delta$) for the poled (top) and unpoled (bottom) for BNT–ST–100xBA ceramics, (a) and (e) $x = 0$, (b) and (f) $x = 0.01$, (c) and (g) $x = 0.02$, (d) and (h) $x = 0.03$.

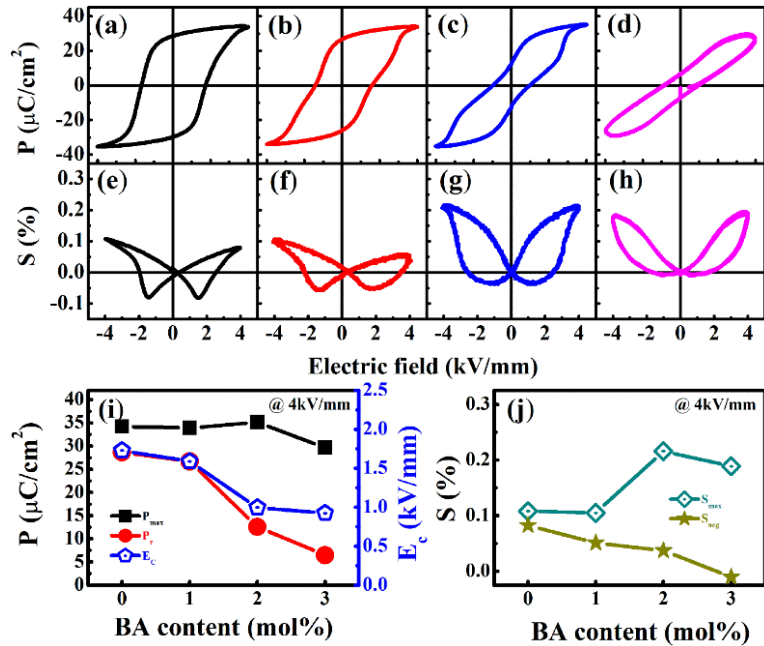


Figure 4.11: Electric field–induced (top) polarization hysteresis (P – E) and (bottom) bipolar strain (S – E) curves for BNT–ST–100xBA ceramics, (a) and (e) $x = 0$, (b) and (f) $x = 0.01$, (c) and (g) $x = 0.02$, (d) and (h) $x = 0.03$. Extracted (i) P_{\max} , P_r , E_c and (j) S_{\max} , S_{neg} parameters for BNT–ST–100xBA ceramics as a function of BA content.

Electric field-induced polarization hysteresis (P - E) and bipolar strain (S - E) curves for BNT-ST-100xBA ceramics under an electric field of 4 kV/mm are depicted in Figure 4.11. Additionally, maximum polarization (P_{\max}), remanent polarization (P_r), coercive field (E_C), maximum strain (S_{\max}), and negative strain (S_{neg}) values were extracted from the P - E and S - E curves and are summarized in Figure 4.11(i) and (j), respectively. As shown in Figure 4.11(a), BNT-ST-0BA ceramics exhibited strong ferroelectricity, which is confirmed by a square-shaped P - E curve and a butterfly-shaped strain curve. P_{\max} , P_r , and E_C for BNT-ST-0BA ceramics were $34.3 \mu\text{C}/\text{cm}^2$, $28.7 \mu\text{C}/\text{cm}^2$, and $1.72 \text{ kV}/\text{mm}$, respectively. With increasing BA content, P_{\max} increased slightly to $35.1 \text{ mC}/\text{cm}^2$ for BNT-ST-2BA ceramics, while P_r and E_C were drastically degraded to $12.6 \mu\text{C}/\text{cm}^2$ and $0.97 \text{ kV}/\text{mm}$, respectively. In the case of BNT-ST-3BA ceramics, all the parameters relating to polarization were decreased to a P_{\max} of $29.6 \mu\text{C}/\text{cm}^2$, a P_r of $6.4 \mu\text{C}/\text{cm}^2$, and a E_C of $0.92 \text{ kV}/\text{mm}$, eventually resulting in slim P - E curves. Bipolar strain properties were also influenced by BA modification. With a small amount of BA modification (less than 1 mol%), butterfly-shaped strain curves were obtained, and S_{\max} and S_{neg} values were slightly degraded from 0.107% and 0.08%, respectively, for BNT-ST-0BA ceramics to 0.105% and 0.05%, respectively, for BNT-ST-1BA ceramics. However, the S_{\max} value for BNT-ST-2BA ceramics drastically increased to 0.21%, which was accompanied by an extreme degradation of S_{neg} . In fact, it is known that phase transition behavior from NER to ER in BNT-based ceramics are responsible for these changes to P - E and S - E curves [19, 182, 202]. Furthermore, S_{neg} was observed to vanish with further increase to the BA content to $x = 0.03$. Accordingly, we conclude that the ER state is completely stabilized in BNT-ST-3BA ceramics.

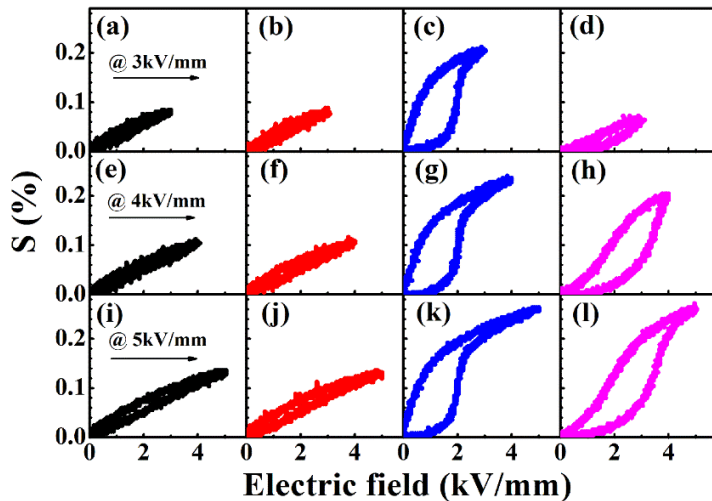


Figure 4.12: Unipolar strain curves for BNT-ST-100xBA ceramics at different applied electric field strengths of 3, 4 and 5 kV/mm, (a), (e), and (i) $x = 0$, (b), (f), and (j) $x = 0.01$, (c), (g), and (k) $x = 0.02$, (d), (h) and (l) $x = 0.03$

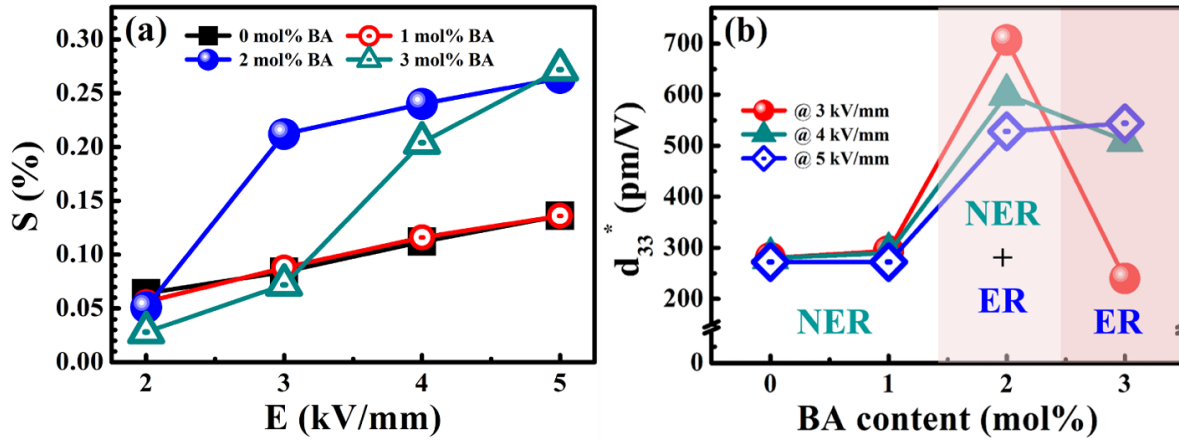


Figure 4.13: (a) S_{\max} values for BNT–ST–100xBA ceramics as a function of applied electric field and (b) d_{33}^* values for BNT–ST–100xBA ceramics as a function of BA content.

Figure 4.12 displays unipolar strain curves for BNT–ST–100xBA ceramics under the applied electric fields of 3, 4, and 5 kV/mm. To better understand the effect of BA modification on unipolar strain, corresponding changes to S_{\max} values for BNT–ST–100xBA ceramics with applied electric fields (2 – 5 kV/mm) are compared in Figure 4.13(a). BNT–ST–0BA ceramics exhibited linear unipolar strain curves regardless of the applied electric field strength. The obtained S_{\max} values at applied electric fields of 3, 4, and 5 kV/mm were 0.08, 0.11, and 0.136%, respectively. The unipolar strain curve for BNT–ST–1BA ceramics preserved this linear behavior with a maximal strain values of 0.139 % obtained at 5 kV/mm. These results are consistent with previous analyses of the temperature-dependent dielectric properties, P – E , and bipolar S – E curves of BNT–ST–0BA and BNT–ST–1BA ceramics that can be categorized as NER (or ferroelectrics). However, the unipolar strain behaviors in BNT–ST–2BA and BNT–ST–3BA ceramics as a function of applied electric field were significantly different from those of BNT–ST–0BA and BNT–ST–1BA ceramics. In the case of BNT–ST–2BA ceramics, abnormally large S_{\max} values were exhibited regardless of the applied electric field strength. The obtained S_{\max} values for BNT–ST–2BA ceramics monotonically increased with increasing applied electric field and were 0.21% at 3 kV/mm, 0.24% at 4 kV/mm, and 0.264% at 5 kV/mm. In contrast, unipolar strain for BNT–ST–3BA ceramics weakly responded to an applied electric field of 3 kV/mm. It is noted that an applied electric field of 3 kV/mm is not enough to trigger a phase transition from ER to ferroelectrics in this material. However, the S_{\max} value drastically increased to 0.21% at 4 kV/mm and 0.27% at 5 kV/mm. These changes in strain behavior are strongly related to different states of the relaxor [26, 182, 210]. More precisely, the required electric field for phase transition from relaxor to ferroelectrics in BNT–ST–3BA ceramics is higher than that for BNT–

ST-2BA ceramics. The reason for this difference is that BNT-ST-3BA ceramics are categorized as fully stabilized ER with absent S_{neg} and drastically decreased P_r , as discussed previously. In other words, this result implies that the electric field required to induce a phase transition from ER to ferroelectrics was decreased by weak nonergodicity (or a small amount of ferroelectric phase) in the BNT-ST-2BA ceramics. Indeed, this fact can be corroborated by detected S_{neg} and P_r values in P - E and bipolar S - E curves, which will be discussed later.

The normalized d_{33}^* ($S_{\text{max}}/E_{\text{max}}$) for BNT-ST-100xBA ceramics as a function of BA content are extracted from the S_{max} data, Figure 4.13(a), and compared in Figure 4.13(b). The calculated d_{33}^* values for BNT-ST-0BA and BNT-ST-1BA ceramics were lower than 300 pm/V regardless of the applied electric field strength, which is a feature of ferroelectrics. On the other hand, BNT-ST-2BA ceramics exhibited significantly enhanced d_{33}^* values. The highest d_{33}^* value of 707 pm/V observed from BNT-ST-2BA ceramics was obtained at an applied electric field 3 kV/mm, which monotonically decreased to 528 pm/V at 5 kV/mm. The reason for these changes in d_{33}^* value is that most of ergodicities in the BNT-ST-2BA ceramics are completely converted to ferroelectrics by an applied electric field of 3 kV/mm. This phenomenon is evidenced by the drastically increased S_{max} and a saturated unipolar strain curve (Figure 4.12). Accordingly, the d_{33}^* values for BNT-ST-2BA ceramics monotonically decreased with increasing electric field strength even though S_{max} increased steadily. In the case of BNT-ST-3BA ceramics, the lowest d_{33}^* value among the BNT-ST-100xBA ceramics, attaining a value of 3 kV/mm under a low applied electric field. Increasing the applied electric field revealed a drastically enhanced d_{33}^* value. This result implies that BNT-ST-3BA ceramics are fully stabilized ER and an applied electric field of 3 kV/mm is not enough to induce a phase transition from ER to ferroelectrics. According to temperature-dependent dielectrics properties and P - E , bipolar S - E , and unipolar S - E curves, we can conclude that BNT-ST-0BA, BNT-ST-1BA ceramics and BNT-ST-3BA ceramics are NER and ER, respectively. Additionally, it is suggested that BNT-ST-2BA ceramics consists of two different phases: NER and ER. These results are displayed in Figure 4.13(b).

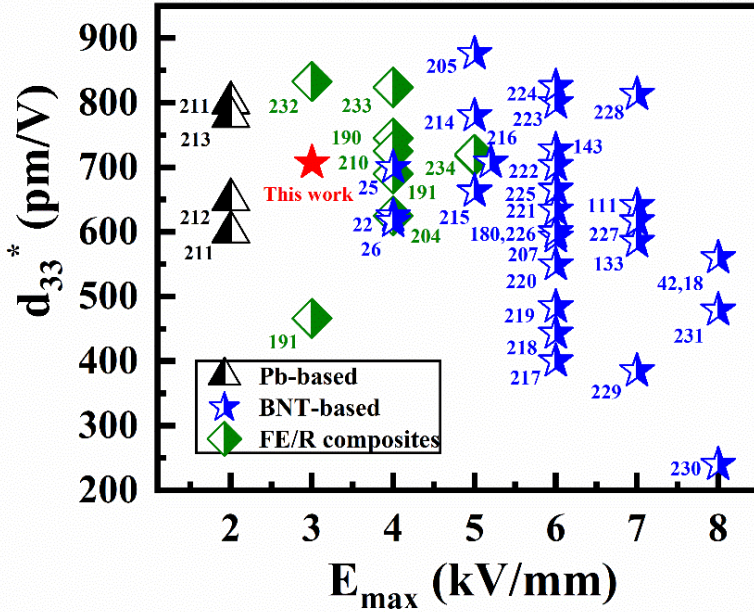


Figure 4.14: Comparison of d_{33}^* values against maximum applied electric fields (E_{max}) between lead-based, lead-free BNT-based, and ferroelectric/relaxor composites.

To confirm our results, the obtained d_{33}^* value for BNT-ST-2BA ceramics are compared to those of other BNT-based materials (Figure 4.14). It is evident that excellent d_{33}^* values have been obtained in the BNT-based materials represented in Figure 4.14 while the operating electric fields were higher than 4 kV/mm. However, the BNT-ST-2BA ceramics of this study presents a high d_{33}^* value at the relatively low electric field of 3 kV/mm, which is superior to other reported BNT-based materials and comparable to other lead-free ferroelectric/relaxor composites [22, 25, 26, 42, 111, 133, 143, 180, 190, 191, 204, 205, 207, 210-234]. As we discussed earlier, we assume that this excellent d_{33}^* value at low driving field for BNT-ST-2BA ceramics originates from the coexistence of NER and ER (more precisely, it seems that nonergodicities are locally spread in the ergodic relaxor).

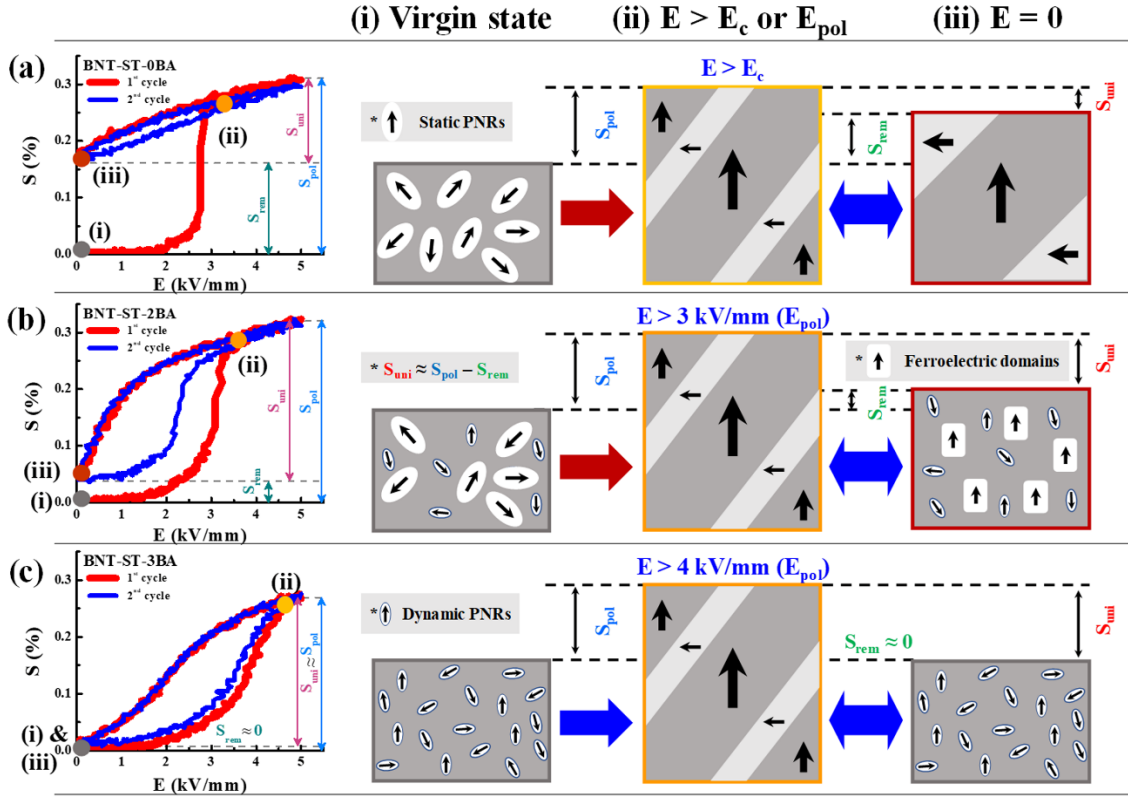


Figure 4.15: Schematic strain mechanisms for three different states of (a) BNT–ST–0BA, (b) BNT–ST–2BA, and (c) BNT–ST–3BA ceramics: stages (i) corresponds to the virgin (or initial) state, stage (ii) corresponds to the application of a significant electric field, and stage (iii) corresponds to removal of the electric field.

To clarify our proposed explanation, a schematic of the strain mechanism for three different states of BNT–ST–0BA, BNT–ST–2BA, and BNT–ST–3BA ceramics is depicted in Figure 4.15. In the case of BNT–ST–0BA ceramics, once electric field ($E \geq E_c$) is applied to NER (consisting of static PNRs) as stage (ii), the highest poling strain (S_{pol}) is obtained with a huge hysteresis at 1st cycle. Phenomenologically, the NER with existing static PNRs in the virgin state (i) are irreversibly transformed into macroscopic ferroelectrics and then ferroelectric domains are aligned to the direction of the electric field (*i.e.*, poling procedure), as illustrated in stage (ii) of Figure 4.15(a). Once induced as ferroelectric domains, these regions are unable to return to the initial (or virgin) state when the applied field is removed. From the perspective of macroscopic strain, a huge remanent strain (S_{rem}) is exhibited by NER. Therefore, a linear unipolar strain (S_{uni}) is practical for applying an electric field during the 2nd cycle. On the other hand, a different strain behavior is exhibited in BNT–ST–3BA ceramics. The ER, consisting of dynamic PNRs (at stage (i) in

Figure 4.15(c), undergoes a reversible phase transition from relaxor to ferroelectrics when an electric field is applied, as shown in stage (ii). Consequently, the highest S_{\max} is commonly obtained with minimal S_{rem} in the ER at a significant electric field ($E > E_{\text{pol}}$). Therefore, we can repeatably obtain a large strain with wide hysteresis in the ER. Finally, the mixed NER and ER state that naturally forms in BNT–ST–2BA ceramics is elucidated. This material can be modeled as consisting of static and dynamic PNRs, which is illustrated in Figure 4.15(b) as stage (i) (or the virgin state). Once a significant electric field is applied to BNT–ST–2BA ceramics, the static and dynamic PNRs are irreversibly and reversibly, respectively, transformed into the ferroelectrics, as shown in stage (ii). Therefore, when the applied electric field is removed, the induced ferroelectric domains partially return to the initial state, as illustrated in stage (iii). More precisely, dynamic PNRs are reversibly randomized, while static PNRs align to the direction of the applied electric field. Therefore, large strain properties are obtained with a huge strain hysteresis and moderate S_{rem} in BNT–ST–2BA ceramics. Interestingly, a significantly decreased poling field (E_{pol}) for BNT–ST–2BA ceramics was observed. This result is the most important feature of investigated materials in this study that strongly relates to the improved d_{33}^* value under low electric field. We assume that the reason for the decreased E_{pol} is the existence of the aligned (or polarized) static PNRs in BNT–ST–2BA ceramics after removing the electric field. In fact, it has been reported that imbedded macroscopic ferroelectric particles (or ferroelectric domains) generates the internal stress in the ER [235]. Furthermore, the electromechanical strain properties under relatively low electric field were improved on due to the generated internal stress [235, 236]. Therefore, it is suggested that the internal stress was induced by the polarized static PNRs in BNT–ST–2BA ceramics, resulting in improvement of strain under low electric field.

4.2.4. Summary

This study investigated the microstructures, crystal structures, and dielectric, ferroelectric, and electromechanical strain properties of lead-free $\text{Bi}_{1/2}\text{Na}_{1/2}\text{TiO}_3\text{--SrTiO}_3\text{--BiAlO}_3$ (BNT–ST–BA) ternary piezoelectric ceramics. It is noted that the highest d_{33}^* value of 707 pm/V was obtained at a relatively low electric field of 3 kV/mm from 2 mol% BA-modified BNT–ST ceramics. We suggest that the naturally induced nonergodicities surrounded by the ergodic relaxor generate internal stress in between their boundaries. Accordingly, this induced internal stress is responsible for the excellent strain properties. We believe that the obtained results indicate that BNT–ST–BA materials are promising candidates for actuator applications.

4.3. Comparing the Electromechanical Properties of CaTiO₃- and BaZrO₃-Modified Bi_{0.5}Na_{0.5}TiO₃-SrTiO₃ Ceramics

This work has been published in Journal of Materials Research in 2020 [237]

The effects of CaTiO₃ (CT) and BaZrO₃ (BZ) modification upon the crystal structure and electromechanical properties of lead-free Bi_{0.5}Na_{0.5}TiO₃-SrTiO₃ piezoelectric ceramics were compared within a doping range of 0-4 mol%. The different effects of CT and BZ modification upon the phase transition are clearly observed in the polarization and strain hysteresis loops. The CT-modified specimens maintain strong ferroelectricity without any abnormal enhancement in the electric field-induced strain. However, the addition of as little as 1mol% BZ induces a transition from a non-ergodic relaxor phase to an ergodic relaxor phase, thus resulting in disruption of the ferroelectric order and the generation of a high field-induced strain. The present authors believe that the substitution of large ions (such as Zr⁴⁺) into the B-sites, rather than the A-sites, of the Bi_{0.5}Na_{0.5}TiO₃-based ceramics plays a significant role in the phase transition behavior.

4.3.1. Introduction

Recently, lead-free piezoceramics have become increasingly important due to the requirement for new alternatives to lead-based ceramics such as Pb(Zr_{1-x}Ti_x)O₃ (PZT) in response to environmental issues [7, 19, 156, 175]. Since first discovery by Smolenskii et.al in 1954 [238], the (Bi_{0.5}Na_{0.5})TiO₃ (BNT) ceramics have been recognized among the most important and superior lead-free materials due to their high Curie temperature (T_C) of 320 °C and relatively large remnant polarization (P_r) of about 38 $\mu\text{C}/\text{cm}^2$ at room temperature. Nevertheless, the effective poling of pure BNT ceramics is difficult because of their large coercive field ($E_C = 7.3$ kV/mm) and high conductivity, which is a disadvantage for the purpose of application. To overcome these problems, chemical modification (ion substitution or solid solutions) is a useful and widely employed method for improving the electrical performances of BNT materials via the construction of phase boundaries [7, 89, 175].

Two kinds of morphotropic phase boundary (MPB) exist in BNT ceramics, namely the typical MPB, or MPB(I), and the polymorphic phase transition, or MPB(II) [107, 108]. In the MPB(I) boundary, the coexistence of ferroelectric rhombohedral and tetragonal phases results in the significant piezoelectricity which can be obtained in (1-x)BNT-xBaTiO₃ (BNT-BT) and (1-x)BNT-x(Bi_{0.5}K_{0.5})TiO₃ (BNKT) material systems [116, 128]. By contrast, the MPB(II) boundary involves a phase transition from ferroelectric to antiferroelectric or from ferroelectric to relaxor ferroelectric (FE-RFE), is temperature-dependent, and has

recently received significant attention due to its high electromechanical strain properties [22, 27, 108-114]. Currently, the solid solution $(1-x)\text{BNT}-x\text{SrTiO}_3$ (BNST) is considered to be an important binary system among BNT-based ceramics, and is reported to form a rhombohedral ferroelectric and pseudocubic MPB at $x = 0.24-0.28$ that results in an ultra-high strain of 0.25% and normalized strain (S_{max}/E_{max}) of 600 pm/V [22, 24, 112, 169, 239]. The origin of large strain in the BNT-based systems is known to be associated with the reversible electric field-induced phase transition from an ergodic relaxor to a ferroelectric state [19, 214, 223]. Furthermore, a similarly large electric field-induced strain has been achieved in many BNT-based ceramics via elemental modification at the A- and/or B-sites, e.g. by the substitution of Fe and Nb into the B-site of BNT-BT [240], the substitution of Ta into BNKT [144], the co-doping of BNKT with Li/Nb [241], or Li-modification of the A-sites in BNKT-BT [242]. Interestingly, in previous work on the modification of BNKT with Nb [111], Cu [243], Sn [136] and Ta [134], the present researchers have found that the FE-RFE phase transition occurs when the dopant modifier leads to a decrease in the Goldschmidt's tolerance factor (t), which is given by Equation 4.1 [36]:

$$t = \frac{r_A + r_O}{\sqrt{2}(r_B + r_O)} \quad 4.1$$

where r_A , r_B , and r_O are the ionic radii of A- and B-site cations, and oxygen, respectively.

Similar phenomena are observed in BNKT modified with other ABO_3 compounds such as LiTaO_3 [143] and CaZrO_3 [228]. Hence, it would be interesting to confirm whether a FE-RFE transition could be induced in the $0.76\text{BNT}-0.24\text{ST}$ ceramics via modification with an ABO_3 -type compound which leads to decreasing tolerance factor. In the present work, CaTiO_3 (CT) and BaZrO_3 (BZ) are selected as two $\text{A}^{2+}\text{B}^{4+}\text{O}_3$ -type endmembers to form two kinds of ternary $\text{BNST}-\text{A}^{2+}\text{B}^{4+}\text{O}_3$ solid solution. Using the Shannon ionic radii, the tolerance factors of CT and BZ are calculated to be 0.966 and 1.01, respectively. Thus, in comparison with the tolerance factor of 0.984 for $0.76\text{BNT}-0.24\text{ST}$ (abbreviated to BNST hereafter), BZ substitution increases the t -value, while CT modification decreases the t -value. This strongly suggests that CT and BZ modifiers exert distinct effects on the ferroelectric properties and could thereby provide further insights into the FE-RFE phase transition of the BNST-based ceramic. Hence, the present paper compares the effect of CT and BZ modification upon the crystal structure, dielectric, ferroelectric and field-induced strain properties of the BNST ceramics.

4.3.2. Experimental details

A range of ceramic powders conforming to the chemical formulas $(0.76-x)\text{Bi}_{0.5}\text{Na}_{0.5}\text{TiO}_3-0.24\text{SrTiO}_3-x\text{CaTiO}_3$ (designated CT100 x) and $(0.76-y)\text{Bi}_{0.5}\text{Na}_{0.5}\text{TiO}_3-0.24\text{SrTiO}_3-y\text{BaZrO}_3$ (designated BZ100 y), with x and $y = 0, 0.01, 0.02, 0.03$ and 0.04 , were synthesized using a conventional solid-state reaction route. The

raw materials Bi_2O_3 (99.99%), Na_2CO_3 (99.0%), TiO_2 (99.99%), SrCO_3 (99.9%), CaCO_3 (99.9%), BaCO_3 (99.9%) and ZrO_2 (99.9%) were weighted according to the nominal compositions after drying at 100 °C for 24 h. After weighing the raw powders according to their stoichiometric formulas, they were mixed and milled thoroughly for 24 h at 400 rpm in a polyethylene jar with ZrO_2 balls (3 and 5 mm in diameter) with ethanol as solvent. The wet slurry was then dried at 100 °C for 24 h, followed by calcination at 850 °C for 2 h with a heating rate of 5 °C/min. The resulting powders were ball milled again with the same parameters. After drying, 10 wt.% of polyvinyl alcohol solution (PVA) was added as a binder. After that, green bodies of 12 mm diameter and about 1.2 mm thickness were prepared and subsequently sintered in covered alumina crucibles at 1175 °C for 2 h with a heating rate of 5 °C/min.

The samples were characterized by X-ray diffraction (XRD; RAD III, Rigaku, Japan) under monochromatic $\text{CuK}\alpha$ radiation with the wavelength $\lambda_{\text{K}\alpha} = 1.54178 \text{ \AA}$. The detection range was 20 to 60 degrees with a step size of 0.02° and a speed of 2°/min. The microstructure was studied by field-emission scanning electron microscope (FE-SEM, JEOL, JSM-6500F, Japan). For measuring the electrical properties, the pellets were coated on both sides with silver paste and sintered at 700 °C for 30 min to form electrodes. The temperature- and frequency-dependent permittivity and dielectric loss of unpoled and poled samples were measured using a high-temperature electric prober system (KEYSIGHT-E4980AL Precision LCR Meter, USA). The electric-field-induced polarization and strain hysteresis loops measurements were performed using the commercial aixPES setup (aixACCT aixPES, Aachen, Germany).

4.3.3. Results and Discussion

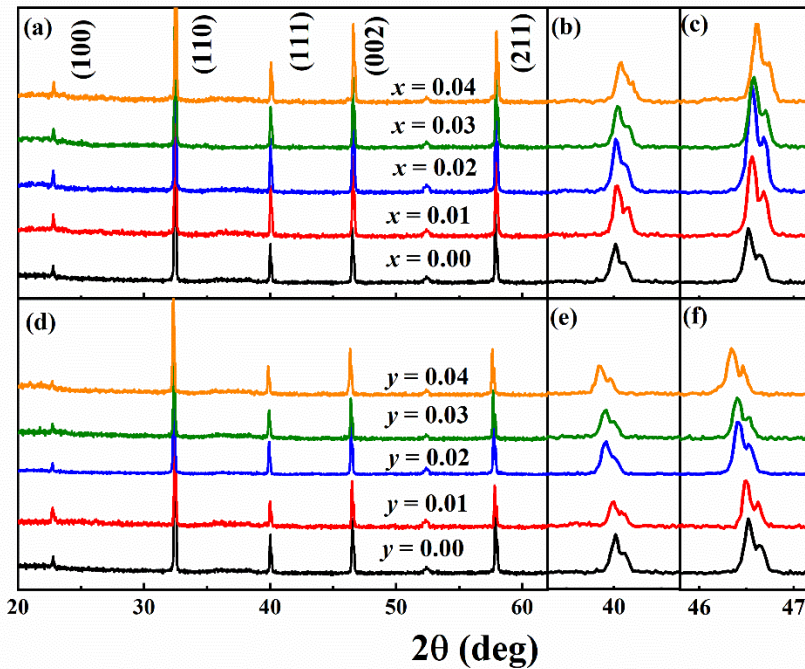


Figure 4.16: X-ray diffraction patterns of (a)-(c) CT100 x with $x = 0.00-0.04$ and (d)-(f) BZ100 y with $y = 0.00-0.04$ ceramics in the 2θ range from 20 to 60°.

The X-ray diffraction patterns of the CT- and BZ-modified BNST ceramics are presented in Figure 4.16. All specimens exhibit a single perovskite structure without any discernible tracks of secondary phase, within the resolution limit of the XRD equipment. This implies that the CT and BZ have diffused into the BNST lattice to form complete solid solutions of BNST-CT and BNST-BZ. In addition, both CT100 x and BZ100 y ceramics display the cubic phases, as indicated by the lack of (111) and (200) peak splitting (except for the $K\alpha$ peaks) at 2θ values of approximately 40° and between 46° and 47°, respectively.

In spite of having the same phase, the addition of CT or BZ leads to completely different evolutions of the lattice parameters in the structures of the BNST ceramics. Thus, whereas the (111) and (200) diffraction peaks of the CT100 x ceramics are seen to gradually shift towards higher angles with increasing concentration of CT, a shift towards lower 2θ values is observed in the BZ100 y ceramics. This result implies that the lattice parameter decreases with CT-substitution but increases with BZ-modification. The origin of this contrast is due to the size difference between the substituent and lattice ions. According to a Shannon's report [37], in the case of 12-fold coordinated A-site ions, Ba^{2+} shows a relatively large ionic radius ($r_{Ba^{2+}} = 1.61 \text{ \AA}$) compared to Ca^{2+} ($r_{Ca^{2+}} = 1.34 \text{ \AA}$) and to the average size of the A-site ions in BNST ($r_{Bi^{3+}} = 1.36 \text{ \AA}$, $r_{Na^+} = 1.39 \text{ \AA}$, $r_{Sr^{2+}} = 1.44$). It is noted that the ion radii of Bi^{3+} for 12-fold coordination is obtained by

extrapolation of its value for the lower coordination numbers [244]. In the case of the 6-fold coordinated B-site ions, the radius of Zr^{4+} is also bigger than that of Ti^{4+} ($r_{Zr^{4+}} = 0.72 \text{ \AA}$, $r_{Ti^{4+}} = 0.605 \text{ \AA}$).

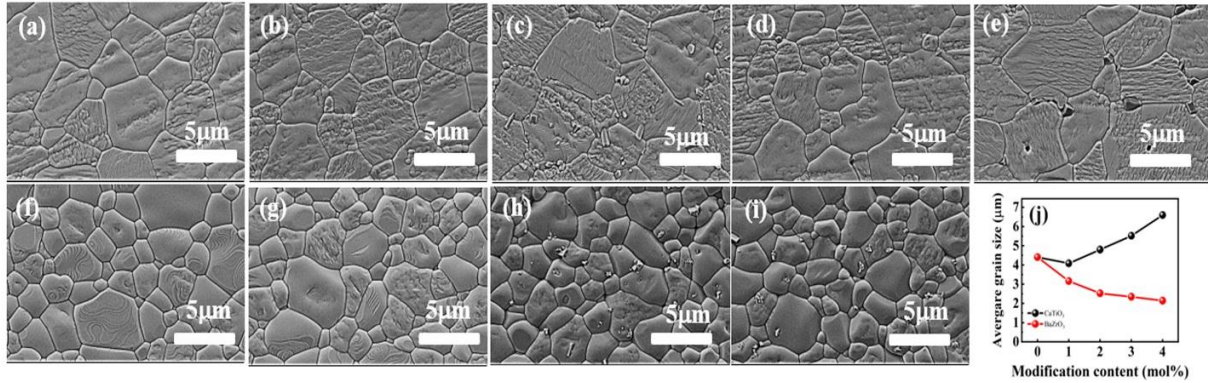


Figure 4.17: Polished and thermally etched surface images of (a)-(e) CT100 x with $x = 0.00-0.04$ and (f)-(i) BZ100 y with $y = 0.01-0.04$, and (j) the average grain size as the function of end-member modification.

The FE-SEM surface micrographs of the polished and thermally etched CT- and BZ-modified BNST ceramics in Figure 4.17 reveal clear differences in the effects of each modifier upon the ceramic microstructures. Thus, while the various CT100 x ceramics display almost identical microstructures, the addition of CT clearly increases the grain size. According to the linear intercept method, the average grain size drastically increases from 4.4 μm for CT0 to around 6.6 μm for CT4, thus demonstrating that CT modification facilitates the growth of grains in the BNST ceramics. By contrast, BZ addition alters the grain morphology from a faceted to a rounder structure and produces a notable decrease in grain size to around 2.1 μm for BZ4, thus indicating that the dissolution of BZ inhibits the grain growth in the BNST ceramics. Since the solid-state sintering process occurs via diffusion-controlled mass transfer through the solid phase, the contrasting effects of CT and BZ upon the ceramic microstructure may be due to the difference in ionic radii of Ca^{2+} , Ba^{2+} and Zr^{4+} . In the case of BZ modification, the smaller Na^+ , Bi^{3+} , and Ti^{4+} ions (1.39 \AA , 1.36 \AA , and 0.605 \AA , respectively) are replaced by the larger Ba^{2+} and Zr^{4+} ions (1.61 \AA and 0.72 \AA , respectively), leading to a decrease in the overall cationic transport due to their lower ion mobility, thus diminishing the diffusion rate and thereby reducing the grain size [245, 246]. By contrast, the presence of the smaller Ca^{2+} (1.34 \AA) in the CT-modified ceramics results in greater ion mobility, which promotes a rapid interdiffusion via the grain boundary, speeding up of the grain growth [247, 248]. Similar changes in

the microstructures of binary BNT-CT and BNT-BZ ceramics have been reported in other studies [249, 250].

In addition, the FE-SEM image of the pure BNST ceramics (CT0 and BZ0), Figure 4.17(a) display rough surfaces which are indicative of domain structures similar to those observed by the present authors in previous work on BNST ceramics produced by thermal etching [22]. In the present work, the domain patterns are seen to persist and extend through the entire volume of the grains with increasing CT concentration, but become less pronounced and decrease in size with BZ modification. The difference in domain structure between the CT- and BZ-modified ceramics influences their electrical and mechanical properties, as described in the following paragraphs.

The temperature-dependent dielectric properties of the poled and unpoled CT100 x and BZ100 y ceramics measured at various frequencies are displayed in Figure 4.18. Here, two distinct anomalies are observed in the dielectric curve of the unmodified ceramics, including: (i) a hump at the ferroelectric-relaxor phase transition temperature (T_{F-R}) of 42 °C, and (ii) a peak at the maximum dielectric constant temperature (T_m) of around 180 °C. With the addition of CT, the T_m increases while T_{F-R} decreases slightly from 42 °C for the unmodified ceramic to around 27 °C for the CT4. By contrast, BZ addition has a significant impact upon the T_{F-R} and T_m values. In comparison with CT modification, the dielectric response of the BZ100 y ceramics exhibits an increase in the broad of T_m and the frequency dispersion at the low temperature region becomes stronger with increasing BZ concentration. This indicates that the relaxation characteristic is more evident in the BZ100 y rather than in the CT100 x system. Moreover, it is reported that the diffuse and frequency-dependent dielectric constant at T_m is mainly attributed to the distortion of A- and B-sites of the perovskite due to the substitution of isovalent cations [203, 251-253]. Thus, the different distortion degrees between Ca²⁺, Ba²⁺ and Zr⁴⁺ ions on the BNST lattice structure are assumed to be the main factor leading to the difference in relaxor behaviors of CT100 x and BZ100 y ceramics. Furthermore, with the addition of only 1 mol% BZ, no discernable T_{F-R} is observed in the measured temperature range of 25- 300 °C. Indeed, all the poled and unpoled BZ100 y samples display similar dielectric curves with the absence of T_{F-R} , thus demonstrating that their transition temperature are below room temperature and, hence, the ergodic relaxor phase will be predominant in the BZ-modified BNST ceramics. The different effects of CT and BZ modification upon the T_{F-R} of the BNST ceramics could lead to distinct ferroelectric and strain properties, as discussed below.

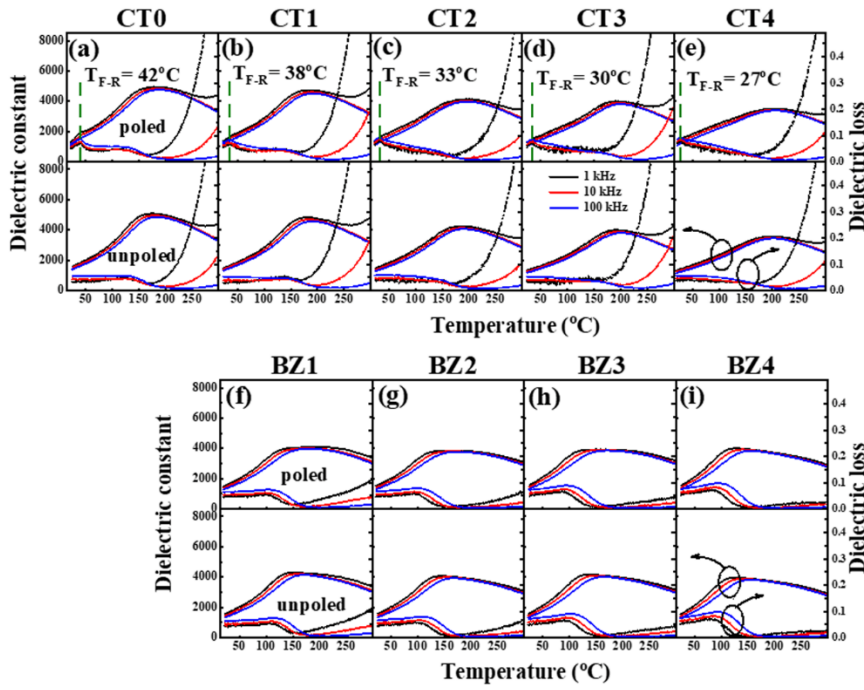


Figure 4.18: Temperature-dependent dielectric constant and dielectric loss for the poled and unpoled of (a)-(e) CT100 x with $x = 0.00-0.04$ and (f)-(i) BZ100 y with $y = 0.01-0.04$.

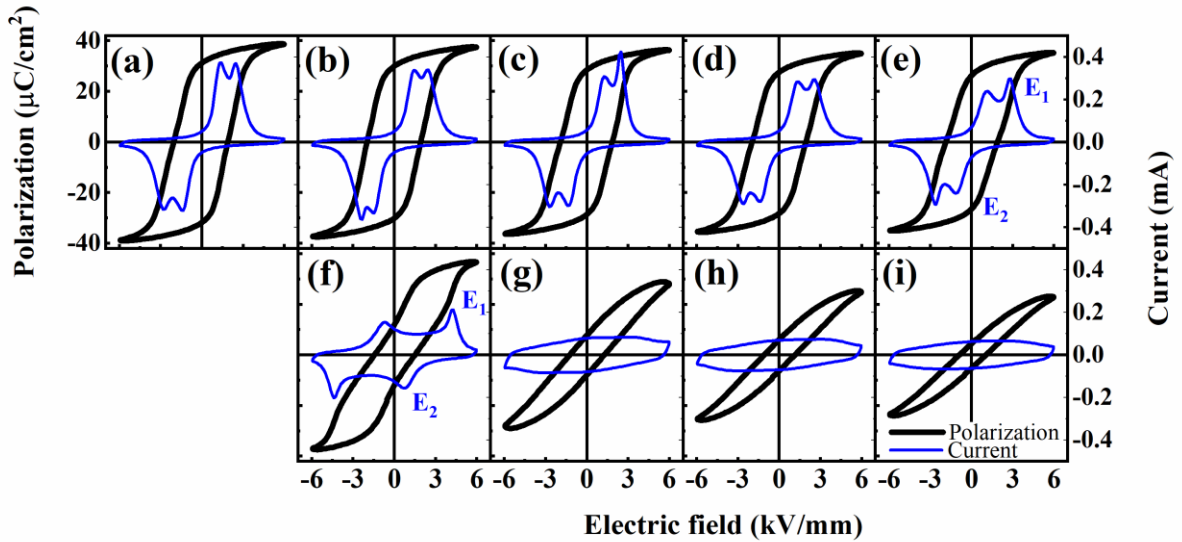


Figure 4.19: Polarization hysteresis loops and switching current curves at 6 kV/mm for (a)-(e) CT100 x with $x = 0.00-0.04$ and (f)-(i) BZ100 y with $y = 0.01-0.04$

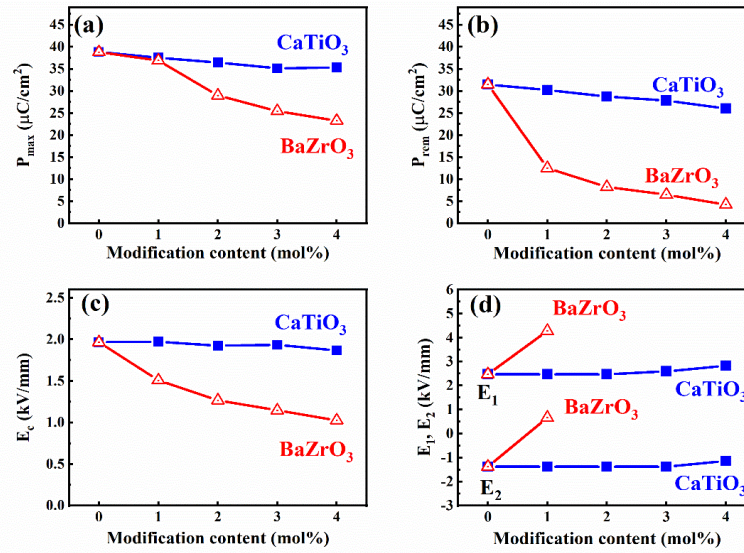


Figure 4.20: Effects of CT- and BZ-modifier content on (a) the maximum polarization, (b) the remnant polarization, (c) the coercive field, and (d) the poling/depolarizing field.

The current versus electric field (I - E) and polarization hysteresis (P - E) loops of the CT- and BZ-modified BNST ceramics measured at 6 kV/mm and room temperature are presented in Figure 4.19. Here, the unmodified BNST ceramic displays a saturated square hysteresis loop indicative of a relatively large remnant polarization and a coercive field. The maximum polarization (P_{max}), remnant polarization (P_{rem}), and coercive field (E_c) of the unmodified BNST are $38.83 \mu\text{C}/\text{cm}^2$, $31.48 \mu\text{C}/\text{cm}^2$, and $1.87 \text{ kV}/\text{mm}$, respectively. Moreover, four current peaks are observed in the I - E curve of the unmodified BNST. The first current peak, E_1 , appears during the loading of a positive field and relates to a domain switching and field-induced phase transitions from a weak polar state to a strong polar state [254, 255]. The field-induced ferroelectric order is irreversible, as evidenced by the absence of a current peak during the unloading, which is characteristic of a non-ergodic relaxor material. The second current peak, E_2 or depolarization field, appears when a negative field is applied which returns the strong polar state to the initial state. The third and fourth current peak to appear during the loading and unloading of the negative electric field share similar functions to those of E_1 and E_2 , respectively.

Significant differences in the effects of the CT and BZ modifiers upon the ferroelectric properties of the BNST ceramics can be observed in the Figure 4.19. Here, the saturated P - E loop is maintained with the addition of CT even up to 4 mol%, whereas the BZ-modified samples display a significant slimming of the loop with increasing BZ concentration. For the CT100x samples, the P_{max} and P_{rem} values decrease slightly as the function of CT modification, while E_c values remain fairly constant. In addition, the charts in Figure 4.20 indicate relatively high P_{max} and P_{rem} values of $35.45 \mu\text{C}/\text{cm}^2$ and $27.51 \mu\text{C}/\text{cm}^2$, respectively, for the

CT4 sample. Furthermore, the CT100 x samples display similar current profiles to that of the unmodified BNST ceramics, thus indicating a relatively weak influence of CT upon the ferroelectric properties of the BNST. By contrast, the addition of 1 mol% BZ is seen to result in a pinching of the P - E loop due to a shift of the depolarization field E_2 to a positive value (0.67 kV/cm), thus indicating a complete reversion of the electric field-induced ferroelectric state to the initial relaxor state. This is accompanied by drastic decreases in the P_{rem} and E_C values from 38.83 $\mu\text{C}/\text{cm}^2$ and 1.87 kV/mm, respectively, for the unmodified sample, to 12.51 $\mu\text{C}/\text{cm}^2$ and 1.51 kV/mm, respectively, for the BZ1 sample. Moreover, significant reductions in all the polarization parameters are observed with increasing BZ content, down to $P_{max} = 23.12 \mu\text{C}/\text{cm}^2$, $P_{rem} = 4.16 \mu\text{C}/\text{cm}^2$, and $E_C = 1.01 \text{ kV}/\text{cm}$ for the BZ4 ceramic, thus resulting in slimmer P - E hysteresis loops. The changes in polarization hysteresis loops and current curves suggest that BZ substitution strongly induces a transition from the non-ergodic relaxor phase to the ergodic relaxor phase in the BNST ceramic, in agreement with previous studies on ABO_3 modified BNT-based ceramics [25, 26, 250, 253, 256].

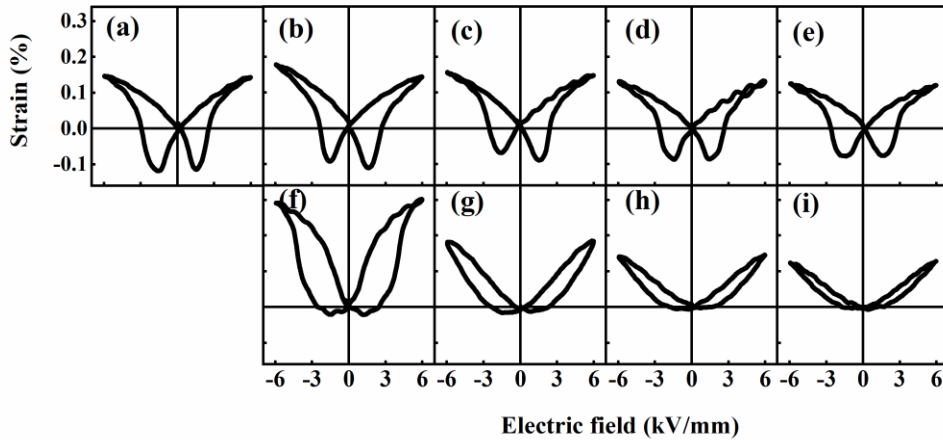


Figure 4.21: Bipolar strain curves at 6 kV/mm for (a)-(e) CT100 x with $x=0.00-0.004$ and (f)-(i) BZ100 y with $y=0.01-0.04$ ceramics.

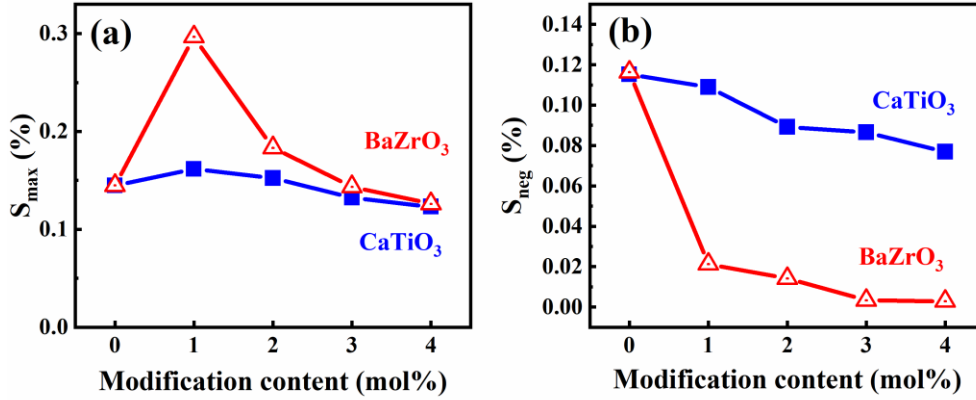


Figure 4.22: Effects of CT- and BZ-doping level on (a) the maximum strain, and (b) the negative strain of the materials.

The relationship between the bipolar strain and the applied electric field (S - E) hysteresis loops of the CT100 x and BZ100 y ceramics at 6 kV/mm is presented in Figure 4.21, while the maximum strain (S_{max}) and negative strain (S_{neg}) values extracted from the S - E curves are plotted as a function of modifier content in Figure 4.22. Thus, the undoped BNST ceramic is seen to exhibit a butterfly-shaped curve (Figure 4.21) with an S_{max} of 0.14% and an S_{neg} of 0.12% (Figure 4.22), as has been typically observed in ferroelectric materials. In addition, a comparison of the S - E curves of CT100 x and BZ100 y ceramics reveals a similar difference to that noted above in the polarization profiles. Thus, the CT-modified samples display no change in the butterfly strain curves with increasing modifier content, along with only slight decreases in the S_{max} and S_{neg} values (to 0.12% and 0.08%, respectively) in the CT4. This retention of the S_{neg} value, which relates to irreversible domain back switching [19, 182, 210, 257], indicates the persistence of ferroelectric phase in the CT100 x system within the doping range examined. By contrast, with the addition of 1 mol% BZ, the bipolar strain curve changes from a butterfly shape to a sprout shape and a drastic reduction in S_{neg} (to 0.02%) is observed, along with a significant increase in S_{max} (to 0.29%). This means that the entire ferroelectric order in the BNST is disrupted upon the addition of BZ, while the development of the ergodic relaxor phase leads to large strain values, as has been reported in previous studies [19, 27, 202, 210, 225, 258, 259]. Moreover, the disappearance of S_{neg} and the reduction in S_{max} with further increases in the BZ content confirm the complete stabilization of the ergodic relaxor state in the BZ100 y ceramics.

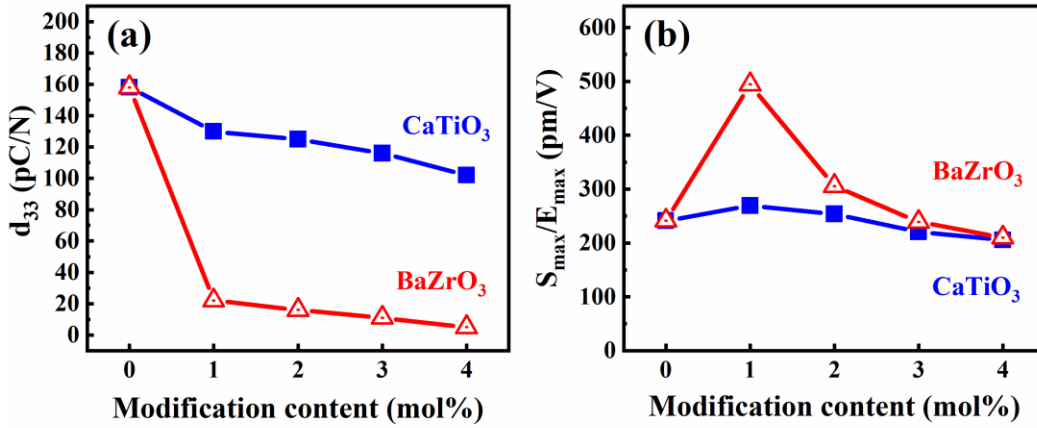


Figure 4.23: (a) Piezoelectric constant (d_{33}) and (b) normalized strain (S_{max}/E_{max}) as the function of CT and BZ content.

The piezoelectric coefficient, d_{33} , and the normalized strain, S_{max}/E_{max} , of the CT- and BZ-modified BNST ceramics are compared in Figure 4.23. Here, the unmodified BNST ceramics displays the maximum d_{33} value of 158 pC/N, with a decrease in d_{33} being observed in the presence of each modifier. However, the level of decrease in d_{33} differs between the two modifiers, with a gradual decrease down to 102 pC/N for the CT4 specimen compared to a severe reduction to around 20 pC/N at only 1 mol% BZ content. The relatively high d_{33} value for the CT100x ceramics can be attributed to the presence of stable electric field-induced ferroelectric domains, a conclusion which is supported by the high P_{rem} and S_{neg} values (Figure 4.19 and Figure 4.21). By contrast, the sharp drop in the d_{33} for the BZ100y ceramics indicates a disruption of the long-range ferroelectric domains, accompanied by an increase in the degree of ergodicity. For the BZ1 sample, the ratio of ferroelectric and ergodic relaxor phases reaches a critical range, thus leading to the maximum S_{max}/E_{max} value of 498 pm/V [114, 259]. The outcomes are consistent with the above analysis results, in which BZ-modification is seen to induce the transition from the non-ergodic phase to the ergodic relaxor phase, whereas CT-modification does not.

It is noted that the results are inconsistent with the present authors' predictions regarding the relationship between the tolerance factor and the ferroelectric-relaxor phase transition [111, 134, 136, 243]. Thus, while the CT100x ceramics retain their ferroelectricity with decreasing t and do not undergo a phase transition within the investigated composition range (0-4 mol%), a rapid transition from ferroelectric to relaxor does occur in the BZ100y solid solutions. Indeed, this phenomenon has been observed in other related works.

For example, in a study by Tran et al. [260], a similar contrast in the phase-transition behavior was obtained for BT- and BZ-modified BNKT ceramics, such that the ferroelectric order of the BNKT-BZ was strongly destabilized but that of the BNKT-BT was little affected [260]. Furthermore, a significant enhancement in the electric field-induced strain relating to the ferroelectric-relaxor transition has previously been revealed with the substitution of 3 mol% CZ into BNKT ceramics [228], which has not been observed in the present work with the CT100x ceramics.

In view of these contrasting results, it is assumed that the FE-RFE phase transition in $A^{2+}B^{4+}O_3$ -modified BNT-based ceramics depends strongly on the isovalent cation substitution for the Ti^{4+} ion on the B-sites, rather than the A-sites. In the unit cell of BNT, the A-sites are randomly occupied by the cations Na^+ and Bi^{3+} , while the Ti^{4+} ions are bonded to six O^{2-} to form TiO_6 octahedra. Recently, it has been reported that the TiO_6 octahedral rotation plays an important role in establishing the relaxor phase in BNT-based materials [261]. When isovalent cations such as Zr^{4+} and Sn^{4+} substitute for Ti^{4+} , they can incorporate into the TiO_6 octahedral lattices. The large ion radius and non-ferroelectric activity of Zr^{4+} eventually cause the displacement of Ti^{4+} and distortion of the TiO_6 octahedra, thus leading to disruption of the long-range ferroelectric order [49, 262-268]. By contrast, the influence of divalent cations such as Ba^{2+} and Ca^{2+} upon the TiO_6 octahedral rotation is thought to be less pronounced. Recently, nuclear magnetic resonance (NMR) analysis has been used to investigate the influence of barium addition upon the local structure of the titanium sites in BNT ceramics [269]. It was found that a strongly disordered local structure resulted from the random occupation of the A-sites by Ba^{2+} , whereas there was no distortion of the oxygen octahedra and no change in the polar displacement of Ti^{4+} [269]. Accordingly, it is concluded that the substitution of a certain amount of divalent ions into the A-sites only, without any Zr^{4+} ions being present on B-sites, could allow the establishment of a long-range ferroelectric order under the application of an electric field.

4.3.4. Summary

The effects of CT- and BZ-modification upon the crystal structure, microstructure, and electromechanical properties of lead-free BNST ceramics were systematically compared in the present work. Each modifier was shown to exert a distinct influence upon the phase transition behavior in terms of the ferroelectric and strain properties. The CT substitution contributed little to the disruption of ferroelectric order in the BNST ceramics, as evidenced by the stable ferroelectricity and relatively high piezoelectric constant ($d_{33} > 100$ pC/N) within the composition range investigated (0-4 mol%). By contrast, the BZ-modification was found to strongly induce a transition from the non-ergodic relaxor state to the ergodic relaxor state, thus resulting in narrow P - E loops, disappearance of the piezoelectric properties, and an abnormal enhancement of the electric field-induced strain with the addition of 1 mol% BZ. These results

suggest that the phase transition is greatly influenced by the substitution of large ions (such as Zr^{4+}) onto B-sites, rather than the A-sites, leading to distortion of the TiO_6 octahedra in the BNST ceramics. The present work is believed to be meaningful in clarifying the effect of ABO_3 modification upon the FE-RFE phase transition behavior and electromechanical properties of the BNST-based ceramics.

Chapter 5: Conclusion and outlook

To improve the strain properties of Bi-based lead-free ceramics at lower electric fields, the ternary phase systems BNT-CT-ST and BNT-ST-BA compositions were fabricated. The selective ternary BNT-ST ceramics revealed a single-phase perovskite structure without any traces of secondary phases. All of the synthesized compositions have well dense microstructure and homogeneously distributed grains. The addition of other ABO_3 endmembers brought an enhanced in electric field-induced strain as well as reduced the poling fields.

In details, by utilizing the BNT-CT-ST ternary ceramics, the field-induced-strain behaviors have been improved upon BNT-ST binary materials. For detailed, BNT-CT-28ST ceramics showed the large d_{33}^* value of 667 pm/V, which is higher than 625 pm/V of BNT-28ST [22]. In fact, the main reason for the relatively enhanced strain of this system is unclear yet. We are assuming that the induced nonergodicities by added CT are responsible for relatively enhancing strain properties of BNT-CT-ST ceramics in comparison to BNT-28ST ceramics. To clarify this assumption, it is obviously needed further study. Therefore, we believe that BNT-CT-100xST ceramics are promising candidates for actuator applications.

In the case of BNT-ST-BA, the highest d_{33}^* value of 707 pm/V observed from BNT-ST-2BA ceramics was obtained at an applied electric field 3 kV/mm. The achievement could be compared with the relaxor/ferroelectric composite approaches which are recently considered as good techniques for obtaining high low-field induced strain properties [190-192]. We suggest that the excellent d_{33}^* value at low driving field for BNT-ST-2BA ceramics originates from the coexistence of NER and ER (more precisely, it seems that nonergodicities are locally spread in the ergodic relaxor).

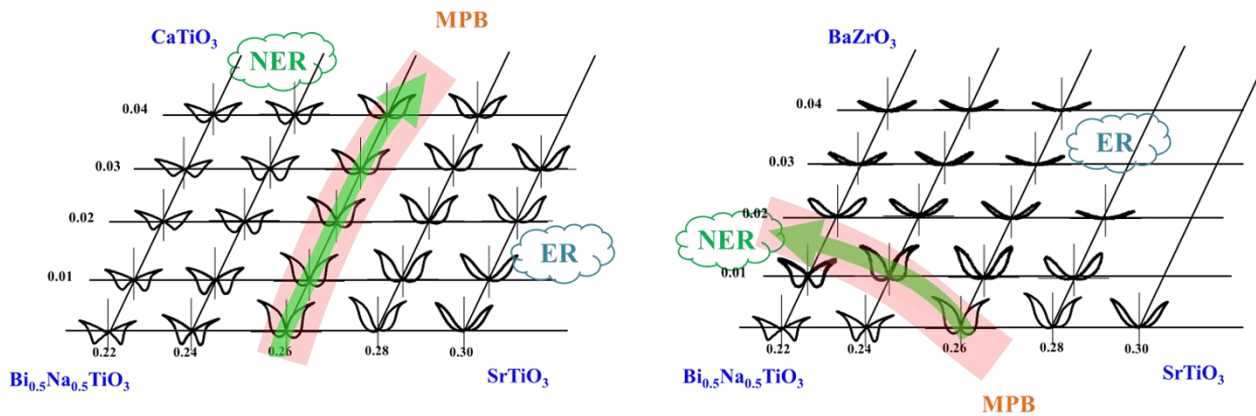


Figure 5.1: The phase diagram of the BNT-ST-CT (left) and BNT-ST-BA (right) ternary system in the range of 0.22-0.30 mol ST content.

Finally, the main finding of the thesis was the investigation of different effects of CT and BZ modifications upon the FE-RFE phase transition in the ternary BNT-ST based ceramics. Both CT and BZ-modified BNST showed relaxor ferroelectric characteristics, however the diffuse transition behavior of BZ-modified specimen was stronger than those modified with CT. With the addition of CT, T_{F-R} decreased slightly from 42 °C for the unmodified ceramic to around 27 °C for the CT4. By contrast, BZ addition had a significant impact upon the T_{F-R} value. With the addition of only 1 mol% BZ, no discernable T_{F-R} was observed, demonstrating that their transition temperature was below room temperature, hence, the ergodic relaxor phase was predominant in the BZ-modified BNT-ST ceramics. The different effects of CT and BZ modification upon the T_{F-R} of the BNT-ST ceramics lead to distinct ferroelectric and strain properties. It was showed that the saturated P-E loop was maintained with the addition of CT even up to 4 mol%, whereas the BZ-modified samples displayed a significant slimming of the loop with increasing BZ concentration.

Furthermore, the phase diagram of BNT-ST-CT and BNT-ST-BZ are presented in Figure 5.1. It is showed that in the case of BNT-ST-BZ, the MPB drastically shifts to the BNT-rich sides. While the MPB in BNT-ST-CT does not change significantly, nearly a vertical line. The differences in electrical properties as well as in the phase diagrams of two systems implies that BZ substitution more strongly induces a transition from the non-ergodic relaxor phase to the ergodic relaxor phase in the BNT-ST ceramic in comparison with CT modification. These results suggest that the phase transition is greatly influenced by the substitution of large ions (such as Zr^{4+}) onto B-sites, rather than the A-sites, leading to distortion of the TiO_6 octahedra in the BNT-ST ceramics.

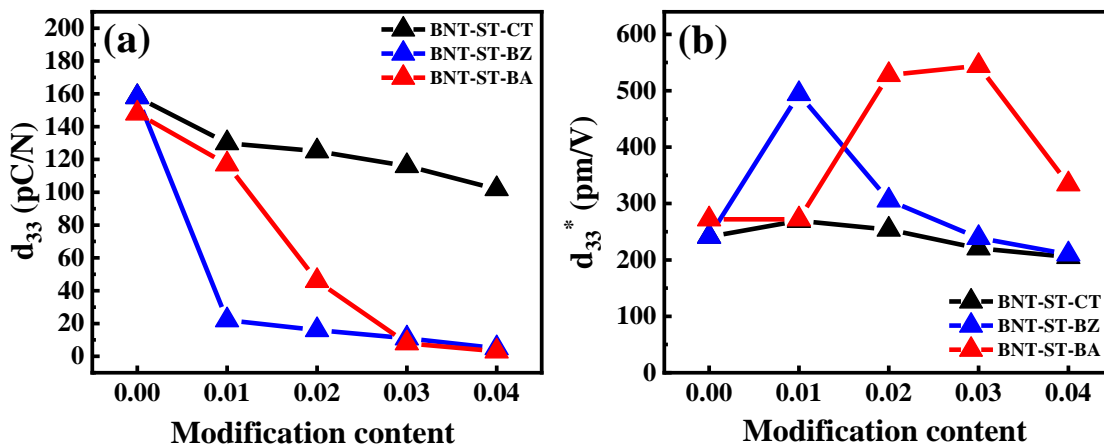


Figure 5.2: Compositional dependence of (a) piezoelectric constant (d_{33}) and (b) normalized strain (d_{33}^*) of BNT-ST-CT, BNT-ST-BZ and BNT-ST-BA ceramics.

It is noted that in our study, beside two ternary BNT-ST-CaTiO₃ and BNT-ST-BaZrO₃ systems, BNT-ST-BiAlO₃ ceramics was been investigated, which also showed a FE-RFE phase transition with the BA modification. However, the degree of relaxor development in BNT-ST-BA is different from in BNT-ST-BZ ceramics. To confirm the difference of phase transition behaviors between BZ and BA-modified BNT-ST ceramics, the summarized data of piezoelectric constants and normalized strains as a function of CT, BZ and BA concentrations are constructed from the polarization and current curves measured at 6 kV/mm for each system, as displayed in Figure 5.2. As we can see, in comparison with BNT-ST-CT, an abnormally high normalized strain d_{33}^* and decrease in piezoelectric constant d_{33} , relating to the disruption of the long-range ferroelectric order, were observed in both BZ and BA-modified samples. However, discernible differences between BZ and BA can be revealed by the changes of slope in d_{33} and d_{33}^* lines. BNT-ST-BZ showed a high slope of d_{33} and a sharp peak in d_{33}^* curve, which means that the degree of stabilization of the ER state in the materials evolved quickly. Meanwhile, we obtained relatively low slope of d_{33} and a broad peak of d_{33}^* in BNT-ST-BA systems. This means that the transition from FE to ER phase is more slowly induced with BA modification compared to BZ-modified ceramics.

The emergence of the FE-RFE phase transition in BNT-ST-BA ceramics could be expected by the existence of the substitution of Al³⁺ ion with Ti⁴⁺ on B-site, leading to the distortion of the octahedral in BNT-ST materials. However, it is not sufficient to explain the slow phase transition in the BNT-ST-BA. It is the fact that in the case of BNT-ST-BA, when Al³⁺ takes position of Ti⁴⁺ on B-site, oxygen vacancies are created to neutralize electric charge; however, these oxygen vacancies are compensated by A-site vacancies due the substitution of Bi³⁺ with (Bi_{0.5}Na_{0.5})²⁺ on A-site. Therefore, theoretically we may assume that there is no charge disorder expected or the charge effect on the phase transition in BNT-ST-BA can be ignored.

Table 5.1: Quantitative evaluation of differences in radii between ion modification and matrix of BaZrO₃ and BiAlO₃ endmembers

| | Ion modification | Difference in radii with ion matrix (Å) | | Average difference (Å) |
|--------------------|------------------|--|------------------|------------------------|
| | | (Bi _{0.5} Na _{0.5}) ²⁺ | Ti ⁴⁺ | |
| | Ti ⁴⁺ | - | 0 | |
| BaZrO ₃ | Ba ²⁺ | 0.235 | - | 0.175 |
| | Zr ⁴⁺ | - | 0.115 | |
| BiAlO ₃ | Bi ³⁺ | 0.015 | - | 0.0425 |
| | Al ³⁺ | - | 0.07 | |

Besides the charge effect, the ion size effect should be also considered in the investigation of relaxor behavior in BNT-ST ceramics. It has been reported that the size difference between a dopant and matrix ions causes a lattice strain, which in turn makes the ferroelectric order unstable [131, 132]. This explanation is strongly supported by study of Hussain et.al, where isovalent Sn doping with a smaller size effect results in the FE-NP transition at a higher doping level than those with larger size differences such as Zr and Hf inducing the transition at lower doping levels of 2-3 mol% [131, 132]. From that, we can suggest that the degree of the distortion of the octahedral in BNT-ST ceramics, which is a driving force for the FE-RFE phase transition, is influenced by the strength of compress or tension strain induced by the substitution of a small or large ion, respectively. The modifications with more size differences compared to the ion matrix will create high compress or tension strain correspondingly on the octahedral; and therefore, a more rapid promotion for FE-RFE phase transition can be observed in those modifications. From this idea, a quantitative evaluation of differences in radii between ion modification and matrix of BZ and BA endmembers is depicted in Table 5.1. In comparison with BZ modification, BA shows a lower average difference between the ion substitution and ion matrix, which results in a slow transition and consistent with our mentioned assumption.

In summary, this work contains dedications to reveal the effects of three various ABO_3 modification: $CaTiO_3$, $BaZrO_3$ and $BiAlO_3$ on the FE-RFE phase transition behavior in ternary BNT-ST system as followings:

1) The CT substitution contributed little to the disruption of ferroelectric order in the BNST ceramics, as evidenced by the stable ferroelectricity and relatively high piezoelectric constant ($d_{33} > 100$ pC/N) within the composition range investigated (0-4 mol%). The delay in development of relaxor state in CT-modified specimens is attributed to the absence of B-site substitution and the less pronounced influence of Ca^{2+} upon the octahedral ration in BNT-ST ceramics.

2) By contrast, the BZ-modification was found to strongly induce a transition from the non-ergodic relaxor state to the ergodic relaxor state, thus resulting in a disappearance of the piezoelectric properties, and an abnormal enhancement of the electric field-induced strain with the addition of 1 mol% BZ. These results suggest that the phase transition is greatly influenced by the substitution of large ions (such as Zr^{4+}) onto B-sites. Such large ion radius and non-ferroelectric activity of Zr^{4+} eventually cause the displacement of Ti^{4+} and distortion of the TiO_6 octahedra, thus leading to disruption of the long-range ferroelectric order

3) In the case of BNT-ST-BA ceramics, it was found that the existence of smaller ion Al^{3+} substitution on Ti-sites also led to a FE-RFE phase transition in BNT-ST ceramics, but the transition occurred more slowly than that of BZ-modified specimens. We believe this phenomenon relates to the size-difference

effect. From that, due to a smaller size difference in BA substitution with respect to A-site and B-site ion matrixes (0.042 Å compared with 0.175 Å in BZ modifier), the induced tension strain in the BNT-ST-BA will be less impacted on the distortion of the TiO_6 octahedral, which do not promote the disruption of the long-range order as strongly as in the case of BNT-ST-BZ ceramics.

References

1. A. Bhalla, R. Guo and R. Roy. *J Materials Research Innovations* **4**, 3 (2000).
2. D.M. Smyth. *Ferroelectrics* **380**, 1 (2009).
3. G.H. Haertling. *J. Am. Ceram. Soc.* **82**, 797 (1999).
4. B. Jaffe and W. Cook: JR. and H. Jaffe, *Piezoelectric Ceramics*, (Academic Press, New York, City, 1971).
5. E. Directive. *Official Journal of the European Union L* **37**, 24 (2002).
6. E. Directive. *Off. J. Eur. Communities* **46**, 19 (2013).
7. J. Rödel, W. Jo, K.T.P. Seifert, E.M. Anton, T. Granzow and D. Damjanovic. *J. Am. Ceram. Soc.* **92**, 1153 (2009).
8. J.-s. YUN and I.-s. PARK. *The adopted Act of* **2**, (2007).
9. Measures for the Administration on Pollution Control of Electronic Information Products, Ministry of Information Industry China Order No. 39, 2006. Available online: : http://www.fdi.gov.cn/1800000121_39_4733_0_7.html.
10. Law for Promotion of Effective Utilization of Resources. Minister of Economy, Trade and Industry, Japan, (2001). <https://www.env.go.jp/en/laws/recycle/06.pdf>
11. P. Baettig, C.F. Schelle, R. LeSar, U.V. Waghmare and N.A. Spaldin. *Chem. Mater.* **17**, 1376 (2005).
12. G. Jones and P. Thomas. *Acta Crystallographica Section B: Structural Science* **58**, 168 (2002).
13. B.N. Rao, R. Datta, S.S. Chandrashekar, D.K. Mishra, V. Sathe, A. Senyshyn and R. Ranjan. *Phys. Rev. B.* **88**, (2013).
14. E. Aksel, J.S. Forrester, J.C. Nino, K. Page, D.P. Shoemaker and J.L. Jones. *Phys. Rev. B.* **87**, (2013).
15. L.E. Cross. *Ferroelectrics* **76**, 241 (1987).
16. I. Chen. *J. Phys. Chem. Solids* **61**, 197 (2000).
17. J. Ravez and A. Simon. *Journal of Solid State Chemistry* **162**, 260 (2001).
18. S.T. Zhang, A.B. Kouniga, E. Aulbach, H. Ehrenberg and J. Rödel. *Appl. Phys. Lett.* **91**, 112906 (2007).
19. W. Jo, R. Dittmer, M. Acosta, J. Zang, C. Groh, E. Sapper, K. Wang and J. Rödel. *J. Electroceram.* **29**, 71 (2012).
20. K. Sakata and Y. Masuda. *Ferroelectrics* **7**, 347 (1974).
21. Y. Hiruma, Y. Imai, Y. Watanabe, H. Nagata and T. Takenaka. *Appl. Phys. Lett.* **92**, 2904 (2008).
22. T.A. Duong, H.S. Han, Y.H. Hong, Y.S. Park, H.T.K. Nguyen, T.H. Dinh and J.S. Lee. *J. Electroceram.* **41**, 73 (2018).
23. J. Koruza, V. Rojas, L. Molina-Luna, U. Kunz, M. Duerschnabel, H.-J. Kleebe and M. Acosta. *J. Eur. Ceram. Soc.* **36**, 1009 (2016).
24. M. Acosta, W. Jo and J. Rödel. *J. Am. Ceram. Soc.* **97**, 1937 (2014).
25. Y. Zhu, Y. Zhang, B. Xie, P. Fan, M.A. Marwat, W. Ma, C. Wang, B. Yang, J. Xiao and H. Zhang. *Ceram. Int.* **44**, 7851 (2018).
26. Y.H. Hong, H.S. Han, G.H. Jeong, Y.S. Park, T.H. Dinh, C.W. Ahn and J.S. Lee. *Ceram. Int.* **44**, 21138 (2018).
27. G. Wang, Y.H. Hong, H.T.K. Nguyen, B.W. Kim, C.W. Ahn, H.S. Han and J.-S. Lee. *Sens. Actuator A-Phys.* **293**, 1 (2019).
28. R. Coelho: *Physics of Dielectrics for the Engineer* (Elsevier, City, 2012).
29. K. Hirota, S. Wakimoto and D.E. Cox. *Journal of the Physical Society of Japan* **75**, 111006 (2006).
30. A.A. Bokov and Z.G. Ye. *Journal of Materials Science* **41**, 31 (2006).
31. G.A. Samara. *J. Phys. Condens. Matter* **15**, R367 (2003).
32. J. Curie and P. Curie. *Bulletin de minéralogie* **3**, 90 (1880).

33. J.F. Nye: Physical properties of crystals: their representation by tensors and matrices (Oxford university press, City, 1985).
34. F. Seitz and D. Turnbull: Solid state physics (Academic Press, City, 1960).
35. Y. Xu: Ferroelectric materials and their applications (Elsevier, City, 2013).
36. V.M. Goldschmidt. *Math.-naturwiss. Kl.* **8**, 5 (1926).
37. R.D. Shannon. *Acta Cryst. A* **32**, 751 (1976).
38. O. Muller, (1974).
39. M.E. Lines and A.M. Glass: Principles and applications of ferroelectrics and related materials (Oxford university press, City, 2001).
40. K. Matsuura, Y. Cho and R. Ramesh. *Appl. Phys. Lett.* **83**, 2650 (2003).
41. C. Kittel. *Physical Review* **82**, 729 (1951).
42. S.-T. Zhang, A.B. Kounga, E. Aulbach, T. Granzow, W. Jo, H.-J. Kleebe and J. Rödel. *J. Appl. Phys.* **103**, 034107 (2008).
43. T. Schäck, M. Muma and A.M. Zoubir. *IEEE Signal Processing Magazine* **34**, 16 (2017).
44. L.E. Cross. *Ferroelectrics* **151**, 305 (1994).
45. Z.G. Ye. *Key Engineering Materials* **155-156**, 81 (1998).
46. G.A. Samara: Ferroelectricity revisited—advances in materials and physics, in Solid State Physics, (Elsevier, City, 2001), pp. 239.
47. A.A. Bokov and Z.-G. Ye. *J. Adv. Dielectr.* **2**, 1241010 (2012).
48. V.V. Shvartsman, D.C. Lupascu and D.J. Green. *J. Am. Ceram. Soc.* **95**, 1 (2012).
49. C.W. Ahn, C.H. Hong, B.Y. Choi, H.P. Kim, H.S. Han, Y. Hwang, W. Jo, K. Wang, J.F. Li and J.S. Lee. *J. Korean Phys. Soc.* **68**, 1481 (2016).
50. T. Egami, E. Mamontov, W. Dmowski and S. Vakhrushev: Temperature dependence of the local structure in Pb containing relaxor ferroelectrics, in AIP Conference Proceedings, (**677**, American Institute of Physics, City, 2003), pp. 48.
51. D. Viehland, S. Jang, L.E. Cross and M. Wuttig. *Phys. Rev. B.* **46**, 8003 (1992).
52. G. Burns and F. Dacol. *Solid State Commun.* **48**, 853 (1983).
53. G. Burns and F. Dacol. *Ferroelectrics* **52**, 103 (1983).
54. P. Bonneau, P. Garnier, G. Calvarin, E. Husson, J. Gavarrri, A. Hewat and A. Morell. *Journal of Solid State Chemistry* **91**, 350 (1991).
55. H. Uwe, K.B. Lyons, H. Carter and P. Fleury. *Phys. Rev. B.* **33**, 6436 (1986).
56. E. Sapper, N. Novak, W. Jo, T. Granzow and J. Rödel. *J. Appl. Phys.* **115**, 194104 (2014).
57. N. Novak, R. Pirc and Z. Kutnjak. *Ferroelectrics* **426**, 31 (2012).
58. O. Noblanc, P. Gaucher and G. Calvarin. *J. Appl. Phys.* **79**, 4291 (1996).
59. M. Algueró, B. Jiménez and L. Pardo. *Appl. Phys. Lett.* **87**, 082910 (2005).
60. R. Sommer, N. Yushin and J. Van der Klink. *Phys. Rev. B.* **48**, 13230 (1993).
61. Z.-G. Ye and H. Schmid. *Ferroelectrics* **145**, 83 (1993).
62. O. Bidault, M. Licheron, E. Husson and A. Morell. *J. Phys. Condens. Matter* **8**, 8017 (1996).
63. R. Farhi, M.E. Marssi, J. Dellis, J. Picot and A. Morell. *Ferroelectrics* **176**, 99 (1996).
64. J. Dellis, M.E. Marssi, P. Tilloloy, R. Farhi and D. Vtfhland. *Ferroelectrics* **201**, 167 (1997).
65. V. Bobnar, Z. Kutnjak, R. Pirc and A. Levstik. *Phys. Rev. B.* **60**, 6420 (1999).
66. E.V. Colla, N.K. Yushin and D. Viehland. *J. Appl. Phys.* **83**, 3298 (1998).
67. M. Davis, D. Damjanovic and N. Setter. *Phys. Rev. B.* **73**, 014115 (2006).
68. J.E. Daniels, W. Jo, J. Rödel and J.L. Jones. *Appl. Phys. Lett.* **95**, 032904 (2009).
69. Y. Ehara, N. Novak, S. Yasui, M. Itoh and K.G. Webber. *Appl. Phys. Lett.* **107**, 262903 (2015).
70. S. Schaab: Influence of charged defects on the polarization dynamics and phase transitions in the relaxor ferroelectric PLZT (VVB Laufersweiler, City, 2011).
71. W. Jo, J.E. Daniels, J.L. Jones, X. Tan, P.A. Thomas, D. Damjanovic and J. Rödel. *J. Appl. Phys.* **109**, 014110 (2011).

72. S. Prosandeev, D. Wang, A. Akbarzadeh, B. Dkhil and L. Bellaiche. *Physical review letters* **110**, 207601 (2013).
73. W. Jo, J. Daniels, D. Damjanovic, W. Kleemann and J. Rödel. *Appl. Phys. Lett.* **102**, 192903 (2013).
74. D.I. Woodward, R. Dittmer, W. Jo, D. Walker, D.S. Keeble, M.W. Dale, J. Rödel and P.A. Thomas. *J. Appl. Phys.* **115**, 114109 (2014).
75. G. Smolensky. *Ferroelectrics* **53**, 129 (1984).
76. V. Kirillov and V. Isupov. *Ferroelectrics* **5**, 3 (1973).
77. A. Bell. *J. Phys. Condens. Matter* **5**, 8773 (1993).
78. V. Westphal, W. Kleemann and M. Glinchuk. *Physical Review Letters* **68**, 847 (1992).
79. M. Glinchuk and R. Farhi. *J. Phys. Condens. Matter* **8**, 6985 (1996).
80. M. Glinchuk, R. Farhi and V. Stephanovich. *Ferroelectrics* **199**, 11 (1997).
81. V. Shvartsman, J. Dec, Z. Xu, J. Banys, P. Keburis and W. Kleemann. *Phase Transitions* **81**, 1013 (2008).
82. V. Shvartsman, J. Zhai and W. Kleemann. *Ferroelectrics* **379**, 77 (2009).
83. C. Laulhé, F. Hippert, J. Kreisel, A. Pasturel, A. Simon, J.-L. Hazemann, R. Bellissent and G. Cuello. *Phase Transitions* **84**, 438 (2011).
84. J. Wu, D. Xiao and J. Zhu. *Chem Rev* **115**, 2559 (2015).
85. B. Jaffe, R. Roth and S. Marzullo. *J. Appl. Phys.* **25**, 809 (1954).
86. D. Damjanovic. *J. Am. Ceram. Soc.* **88**, 2663 (2005).
87. M. Davis, M. Budimir, D. Damjanovic and N. Setter. *J. Appl. Phys.* **101**, (2007).
88. H. Fu and R.E. Cohen. *Nature* **403**, 281 (2000).
89. T. Zheng, J. Wu, D. Xiao and J. Zhu. *Prog. Mater. Sci.* **98**, 552 (2018).
90. G. Shirane, R. Pepinsky and B. Frazer. *Physical Review* **97**, 1179 (1955).
91. S. ROBERTS. *J. Am. Ceram. Soc.* **33**, 63 (1950).
92. E. Sawaguchi. *Journal of the physical society of Japan* **8**, 615 (1953).
93. B. Noheda, J. Gonzalo, L. Cross, R. Guo, S.-E. Park, D. Cox and G. Shirane. *Phys. Rev. B.* **61**, 8687 (2000).
94. W. Cao and L.E. Cross. *Phys. Rev. B.* **47**, 4825 (1993).
95. B. Noheda, D. Cox, G. Shirane, J. Gonzalo, L. Cross and S. Park. *Appl. Phys. Lett.* **74**, 2059 (1999).
96. B. Noheda, D. Cox, G. Shirane, R. Guo, B. Jones and L. Cross. *Phys. Rev. B.* **63**, 014103 (2000).
97. R. Guo, L. Cross, S. Park, B. Noheda, D. Cox and G. Shirane. *Physical Review Letters* **84**, 5423 (2000).
98. D. Damjanovic. *Appl. Phys. Lett.* **97**, 062906 (2010).
99. N. Huang, Z. Liu, Z. Wu, J. Wu, W. Duan, B. Gu and X. Zhang. *arXiv preprint cond-mat/0302462*, (2003).
100. Z. Kutnjak, J. Petzelt and R. Blinc. *Nature* **441**, 956 (2006).
101. S. Ahmad, R. Panda and V. Janas. *Piscataway, NJ: Retguers University*, (2006).
102. G. Jones and P. Thomas, (2002).
103. K. Roleder, J. Suchanicz and A. Kania. *Ferroelectrics* **89**, 1 (1989).
104. J. Suchanicz. *Ferroelectrics* **172**, 455 (1995).
105. K. Yoshii, Y. Hiruma, H. Nagata and T. Takenaka. *Jpn. J. Appl. Phys.* **45**, 4493 (2006).
106. T. Takenaka, H. Nagata and Y. Hiruma. *IEEE transactions on ultrasonics, ferroelectrics, and frequency control* **56**, 1595 (2009).
107. Y. Hiruma, H. Nagata and T. Takenaka. *J. Appl. Phys.* **105**, 084112 (2009).
108. Y. Hiruma, H. Nagata and T. Takenaka. *Appl. Phys. Lett.* **95**, 052903 (2009).
109. C.H. Hong, H.P. Kim, B.Y. Choi, H.S. Han, J.S. Son, C.W. Ahn and W. Jo. *J. Materiomics.* **2**, 1 (2016).
110. S.Y. Cho, E.Y. Kim, S.Y. Kim, T.L. Pham, J.K. Han, D.S. Song, H.K. Jung, J.S. Lee, K.S. An, J. Lim and S.D. Bu. *Energies* **13**, 455 (2020).
111. K.N. Pham, A. Hussain, C.W. Ahn, W. Kim, S.J. Jeong and J.S. Lee. *Mater. Lett.* **64**, 2219 (2010).

112. S. Jo, C.H. Hong, D.S. Kim, H.W. Kang, C.W. Ahn, H.G. Lee, S. Nahm, W. Jo and S.H. Han. *Sens. Actuator A-Phys.* **258**, 201 (2017).
113. Y. Zhang, G. Liang, S. Tang, B. Peng, Q. Zhang, L. Liu and W. Sun. *Ceram. Int.* **46**, 1343 (2020).
114. J. Yin, C. Zhao, Y. Zhang and J. Wu. *Acta Mater.* **147**, 70 (2018).
115. T. Wang, M. Gao, L. Wang, Y. Lu and D. Zhou. *Journal of inorganic materials* **2**, 223 (1987).
116. T. Takenaka, K.I. Maruyama and K. Sakata. *Jpn. J. Appl. Phys.* **30**, 2236 (1991).
117. B.-J. Chu, D.-R. Chen, G.-R. Li and Q.-R. Yin. *J. Eur. Ceram. Soc.* **22**, 2115 (2002).
118. R. Ranjan and A. Dviwedi. *Solid State Commun.* **135**, 394 (2005).
119. C. Xu, D. Lin and K.W. Kwok. *Solid State Sciences* **10**, 934 (2008).
120. J.G. Pettry, S. Said, P. Marchet and J. Mercurio. *J. Eur. Ceram. Soc.* **24**, 1165 (2004).
121. C. Ma and X. Tan. *Solid State Commun.* **150**, 1497 (2010).
122. H. Simons, J. Daniels, W. Jo, R. Dittmer, A. Studer, M. Avdeev, J. Rödel and M. Hoffman. *Appl. Phys. Lett.* **98**, 082901 (2011).
123. B. Parija, T. Badapanda, S. Panigrahi and T. Sinha. *J. Mater. Sci. Mater. Electron.* **24**, 402 (2013).
124. J. Anthoniappen, C.H. Lin, C. Tu, P.Y. Chen, C.S. Chen, S.J. Chiu, H.Y. Lee, S.F. Wang and C.M. Hung. *J. Am. Ceram. Soc.* **97**, 1890 (2014).
125. H. Lidjici, B. Lagoun, M. Berrahal, M. Rguitti, M.A. Hentatti and H. Khemakhem. *J. Alloys Compd.* **618**, 643 (2015).
126. B.-H. Kim, S.-J. Han, J.-H. Kim, J.-H. Lee, B.-K. Ahn and Q. Xu. *Ceram. Int.* **33**, 447 (2007).
127. O. Elkechai, M. Manier and J. Mercurio. *physica status solidi (a)* **157**, 499 (1996).
128. A. Sasaki, T. Chiba, Y. Mamiya and E. Otsuki. *Jpn. J. Appl. Phys.* **38**, 5564 (1999).
129. Z. Yang, B. Liu, L. Wei and Y. Hou. *Materials Research Bulletin* **43**, 81 (2008).
130. Y.R. Zhang, J.F. Li and B.P. Zhang. *J. Am. Ceram. Soc.* **91**, 2716 (2008).
131. A. Hussain, C.W. Ahn, J.S. Lee, A. Ullah and I.W. Kim. *Sens. Actuator A-Phys.* **158**, 84 (2010).
132. A. Hussain, C.W. Ahn, A. Ullah, J.S. Lee and I.W. Kim. *Jpn. J. Appl. Phys.* **49**, 041504 (2010).
133. J.S. Lee, K.N. Pham, H.S. Han, H.B. Lee and V.D.N. Tran. *J. Korean Phys. Soc.* **60**, 212 (2012).
134. N.B. Do, H.B. Lee, C.H. Yoon, J.K. Kang, J.S. Lee and I.-W. Kim. *Trans. Electr. Electron. Mater.* **12**, 64 (2011).
135. K.-N. Pham, H.B. Lee, H.-S. Han, J.K. Kang, J.-S. Lee, A. Ullah, C.-W. Ahn and I.W. Kim. *J. Korean Phys. Soc.* **60**, 207 (2012).
136. H.S. Han, C.W. Ahn, I.W. Kim, A. Hussain and J.S. Lee. *Mater. Lett.* **70**, 98 (2012).
137. T.H. Dinh, M.R. Bafandeh, J.-K. Kang, C.-H. Hong, W. Jo and J.-S. Lee. *Ceram. Int.* **41**, S458 (2015).
138. Y.-R. Zhang, J.-F. Li, B.-P. Zhang and C.-E. Peng. *J. Appl. Phys.* **103**, 074109 (2008).
139. A. Moosavi, M. Bahrevar, A. Aghaei, P. Ramos, M. Algueró and H. Amorín. *J. Phys. D-Appl. Phys.* **47**, 055304 (2014).
140. D. Lin, D. Xiao, J. Zhu and P. Yu. *Appl. Phys. Lett.* **88**, 062901 (2006).
141. Y. Liao, D. Xiao, D. Lin, J. Zhu, P. Yu, L. Wu and X. Wang. *Ceram. Int.* **33**, 1445 (2007).
142. V.-Q. Nguyen, C.-H. Hong, H.-Y. Lee, Y.M. Kong, J.-S. Lee and K.-K. Ahn. *J. Korean Phys. Soc.* **61**, 895 (2012).
143. V.Q. Nguyen, H.S. Han, K.J. Kim, D.D. Dang, K.K. Ahn and J.S. Lee. *J. Alloys Compd.* **511**, 237 (2012).
144. X. Liu and X. Tan. *Adv. Mater.* **28**, 574 (2016).
145. W. Krauss, D. Schütz, F.A. Mautner, A. Feteira and K. Reichmann. *J. Eur. Ceram. Soc.* **30**, 1827 (2010).
146. J. Shi, H. Fan, X. Liu and Q. Li. *J. Eur. Ceram. Soc.* **34**, 3675 (2014).
147. F. Wang, M. Xu, Y. Tang, T. Wang, W. Shi and C.M. Leung. *J. Am. Ceram. Soc.* **95**, 1955 (2012).
148. H.E. Mgbemere, R.P. Fernandes and G.A. Schneider. *J. Eur. Ceram. Soc.* **33**, 3015 (2013).
149. D. Rout, K.-S. Moon, S.-J.L. Kang and I. Kim. *J. Appl. Phys.* **108**, 084102 (2010).
150. J.-K. Lee, K.S. Hong, C.K. Kim and S.-E. Park. *J. Appl. Phys.* **91**, 4538 (2002).

151. S.E. Park and K.S. Hong. *Journal of Materials Research* **12**, 2152 (1997).
152. J.-R. Gomah-Pettry, S. Saïd, P. Marchet and J.-P. Mercurio. *J. Eur. Ceram. Soc.* **24**, 1165 (2004).
153. S.-E. Park and K.S. Hong. *Journal of materials research* **12**, 2152 (1997).
154. B.D. Cullity. *Wesley Mass.* (1978).
155. H.T.K. Nguyen, T.A. Duong, F. Erkinov, H. Kang, B.W. Kim, C.W. Ahn, H.-S. Han and J.-S. Lee. *J. Korean Ceram. Soc.*, (2020).
156. J. Rödel, K.G. Webber, R. Dittmer, W. Jo, M. Kimura and D. Damjanovic. *J. Eur. Ceram. Soc.* **35**, 1659 (2015).
157. A.J. Bell and O. Deubzer. *MRS Bull.* **43**, 581 (2018).
158. J. Rödel and J.F. Li. *MRS Bull.* **43**, 576 (2018).
159. J.K. Kang and J.S. Lee. *J. Korean Inst. Electr. Electron. Mater. Eng.* **27**, 702 (2014).
160. S. Cho, J.H. Yoo and Y.H. Jeong. *Trans. Electr. Electron. Mater.* **20**, 328 (2019).
161. G. Liu, W. Jiang, K. Liu, X. Liu, C. Song, Y. Yan and L. Jin. *J. Electron. Mater.* **46**, 5287 (2017).
162. Y.H. Kwon, D.J. Shin and J.H. Koh. *J. Korean Phys. Soc.* **66**, 1067 (2015).
163. B. Malic, J. Koruza, J. Hrescak, J. Bernard, K. Wang, J.G. Fisher and A. Bencan. *Materials* **8**, 8117 (2015).
164. J.-K. Kang, T.H. Dinh, C.-H. Lee, H.-S. Han, J.-S. Lee and V.D.N. Tran. *Trans. Electr. Electron. Mater.* **18**, 19 (2017).
165. S.-T. Zhang, A.B. Kouna, E. Aulbach, H. Ehrenberg and J. Rödel. *Appl. Phys. Lett.* **91**, 112906 (2007).
166. T.H. Dinh, H.-S. Han, J.-S. Lee, C.-W. Ahn, I.-W. Kim and M.R. Bafandeh. *J. Korean Phys. Soc.* **66**, 1077 (2015).
167. A.R. Paterson, H. Nagata, X. Tan, J.E. Daniels, M. Hinterstein, R. Ranjan, P.B. Groszewicz, W. Jo and J.L. Jones. *MRS Bull.* **43**, 600 (2018).
168. M. Acosta, L.A. Schmitt, L. Molina-Luna, M.C. Scherrer, M. Brilz, K.G. Webber, M. Deluca, H.J. Kleebe, J. Rödel and W. Donner. *J. Am. Ceram. Soc.* **98**, 3405 (2015).
169. H.L. Li, Q. Liu, J.J. Zhou, K. Wang, J.F. Li, H. Liu and J.Z. Fang. *J. Eur. Ceram. Soc.* **36**, 2849 (2016).
170. S.-H. Kim, S.-H. Lee, H.-S. Han and J.-S. Lee. *J. Korean Inst. Electr. Electron. Mater. Eng.* **32**, 35 (2019).
171. Y. Watanabe, Y. Hiruma, H. Nagata and T. Takenaka. *Ceram. Int.* **34**, 761 (2008).
172. W. Bai, L. Li, W. Wang, B. Shen and J. Zhai. *Solid State Commun.* **206**, 22 (2015).
173. Y. Gong, X. He, C. Chen and Z. Yi. *Ceram. Int.* **45**, 7173 (2019).
174. A. Ullah, M. Alam, A. Ullah, C.W. Ahn, J.-S. Lee, S. Cho and I.W. Kim. *RSC Adv.* **6**, 63915 (2016).
175. J. Hao, W. Li, J. Zhai and H. Chen. *Mater. Sci. Eng. R Rep.* **135**, 1 (2019).
176. T. Frömling, S. Steiner, A. Ayrikyan, D. Bremecker, M. Dürrschnabel, L. Molina-Luna, H.-J. Kleebe, H. Hutter, K.G. Webber and M. Acosta. *J. Mater. Chem. C* **6**, 738 (2018).
177. E. Aksel and J.L. Jones. *J. Am. Ceram. Soc.* **93**, 3012 (2010).
178. H. Tagawa, K. Kimura, T. Fujino and K. Ouchi. *Denki Kagaku* **52**, 154 (1984).
179. H.-S. Han, W. Jo, J. Rödel, I.-K. Hong, W.-P. Tai and J.-S. Lee. *J. Phys. Condens. Matter* **24**, 365901 (2012).
180. K. Wang, A. Hussain, W. Jo, J. Rödel and D.D. Viehland. *J. Am. Ceram. Soc.* **95**, 2241 (2012).
181. W. Jo, S. Schaab, E. Sapper, L.A. Schmitt, H.-J. Kleebe, A.J. Bell and J. Rödel. *J. Appl. Phys.* **110**, 074106 (2011).
182. H.S. Han, W. Jo, J.K. Kang, C.W. Ahn, I.W. Kim, K.K. Ahn and J.S. Lee. *J. Appl. Phys.* **113**, 154102 (2013).
183. T.H. Dinh, J.-K. Kang, J.-S. Lee, N.H. Khansur, J. Daniels, H.-Y. Lee, F.-Z. Yao, K. Wang, J.-F. Li and H.-S. Han. *J. Eur. Ceram. Soc.*, (2016).
184. N. Chen, W. Yao, C. Liang, S. Xiao, J. Hao, Z. Xu and R. Chu. *Ceram. Int.* **42**, 9660 (2016).
185. V.D.N. Tran, A. Ullah, T.H. Dinh and J.-S. Lee. *J. Electron. Mater.* **45**, 2627 (2016).

186. M. Chandrasekhar and P. Kumar. *J. Electroceram.* **38**, 111 (2017).
187. M. Tachibana and E. Takayama-Muromachi. *Phys. Rev. B.* **79**, 100104(R) (2009).
188. N. Novak, R. Pirc, M. Wencka and Z. Kutnjak. *Phys. Rev. Lett.* **109**, 037601 (2012).
189. A. Zaman, A. Hussain, R.A. Malik, A. Maqbool, S. Nahm and M.-H. Kim. *J. Phys. D-Appl. Phys.* **49**, 175301 (2016).
190. D.S. Lee, D.H. Lim, M.S. Kim, K.H. Kim and S.J. Jeong. *Appl. Phys. Lett.* **99**, 062906 (2011).
191. T.H. Dinh, J.-K. Kang, H.T.K. Nguyen, T.A. Duong, J.-S. Lee, V.D.N. Tran and K.N. Pham. *J. Korean Phys. Soc.* **68**, 1439 (2016).
192. A. Khaliq, M. Sheeraz, A. Ullah, J.S. Lee, C.W. Ahn and I.W. Kim. *Sens. Actuator A-Phys.* **258**, 174 (2017).
193. H.T.K. Nguyen, T.A. Duong, F. Erkinov, C.W. Ahn, B.W. Kim, H.-S. Han and J.-S. Lee. *J. Electron. Mater.* **49**, 6677 (2020).
194. J. Koruza, A.J. Bell, T. Frömling, K.G. Webber, K. Wang and J. Rödel. *J. Materiomics.* **4**, 13 (2018).
195. C. He, X. Bai, J. Wang, Y. Liu, Y. Lu, X. Liu, Y. Xiang, Z. Xu and Y. Chen. *J. Electron. Mater.* **49**, 4364 (2020).
196. A. Zaman, R.A. Malik, A. Maqbool, A. Hussain, T. Ahmed, T.K. Song, W.J. Kim and M.H. Kim. *J. Electron. Mater.* **47**, 2103 (2017).
197. Y. Sun, Y. Zhao, J. Xu, L. Yang, C. Zhou, G. Rao and H. Wang. *J. Electron. Mater.* **49**, 1131 (2019).
198. H.S. Mohanty, T. Dam, H. Borkar, A. Kumar, K.K. Mishra, S. Sen, B. Behera, B. Sahoo and D.K. Pradhan. *Ferroelectrics* **517**, 25 (2017).
199. H.S. Mohanty, T. Dam, H. Borkar, D.K. Pradhan, K.K. Mishra, A. Kumar, B. Sahoo, P.K. Kulriya, C. Cazorla, J.F. Scott and D.K. Pradhan. *J. Phys. Condens. Matter* **31**, 075401 (2019).
200. H.S. Mohanty, A. Kumar, B. Sahoo, P.K. Kurliya and D.K. Pradhan. *J. Mater. Sci. Mater. Electron.* **29**, 6966 (2018).
201. S.-F. Wang, C.-S. Tu, T.-L. Chang, P.-Y. Chen, C.-S. Chen, V. Hugo Schmidt and J. Anthoniappen. *J. Appl. Phys.* **116**, 154101 (2014).
202. W. Bai, D. Chen, P. Zheng, B. Shen, J. Zhai and Z. Ji. *Dalton Trans.* **45**, 8573 (2016).
203. A. Hussain, J.U. Rahman, A. Zaman, R.A. Malik, J.S. Kim, T.K. Song, W.J. Kim and M.H. Kim. *Mater. Chem. Phys.* **143**, 1282 (2014).
204. C. Groh, D.J. Franzbach, W. Jo, K.G. Webber, J. Kling, L.A. Schmitt, H.J. Kleebe, S.J. Jeong, J.S. Lee and J. Rödel. *Adv. Funct. Mater.* **24**, 356 (2014).
205. R.A. Malik, J.K. Kang, A. Hussain, C.W. Ahn, H.S. Han and J.S. Lee. *Appl. Phys. Express* **7**, 061502 (2014).
206. D.S. Lee, S.J. Jeong, M.S. Kim and J.H. Koh. *J. Appl. Phys.* **112**, 124109 (2012).
207. A. Ullah, C.W. Ahn, A. Hussain, S.Y. Lee, H.J. Lee and I.W. Kim. *Curr. Appl. Phys.* **10**, 1174 (2010).
208. A. Ullah, C.W. Ahn, A. Hussain, S.Y. Lee and I.W. Kim. *J. Am. Ceram. Soc.* **94**, 3915 (2011).
209. W. Bai, D. Chen, Y. Huang, B. Shen, J. Zhai and Z. Ji. *J. Alloys Compd.* **667**, 6 (2016).
210. T.H. Dinh, V.D.N. Tran, T.T. Nguyen, Q.T.N. Hoang, H.S. Han and J.S. Lee. *Ceram. Int.* **43**, 17160 (2017).
211. T.R. Shrout and S.J. Zhang. *J. Electroceram.* **19**, 113 (2007).
212. H. Kungl and M.J. Hoffmann. *J. Appl. Phys.* **107**, 054111 (2010).
213. N.J. Donnelly, T.R. Shrout and C.A. Randall. *J. Am. Ceram. Soc.* **90**, 490 (2007).
214. S.K. Gupta, R. McQuade, B. Gibbons, P. Mardilovich and D.P. Cann. *J. Appl. Phys.* **127**, 074104 (2020).
215. Z.H. Zhao, R.F. Ge and Y. Dai. *J. Adv. Dielectr.* **09**, 1950022 (2019).
216. B. Yan, H. Fan, C. Wang, M. Zhang, A.K. Yadav, X. Zheng, H. Wang and Z. Du. *Ceram. Int.* **46**, 281 (2020).

217. W. Bai, L. Wang, P. Zheng, F. Wen, J. Zhai and Z. Ji. *Ceram. Int.* **44**, 11402 (2018).
218. N.B. Do, H.-B. Lee, D.T. Le, S.-K. Jeong, I.-W. Kim, W.-P. Tai and J.-S. Lee. *Curr. Appl. Phys.* **11**, S134 (2011).
219. I.W. Kim, A. Ullah, S.Y. Lee, H.J. Lee, C.W. Ahn, H.I. Hwang, A. Hussain and J.S. Lee. *J. Korean Phys. Soc.* **57**, 1102 (2010).
220. H.B. Lee, D.J. Heo, R.A. Malik, C.H. Yoon, H.S. Han and J.S. Lee. *Ceram. Int.* **39**, S705 (2013).
221. V.D.N. Tran, A. Ullah, T.H. Dinh and J.-S. Lee. *J. Electron. Mater.* **45**, 2639 (2016).
222. A. Ullah, R.A. Malik, A. Ullah, D.S. Lee, S.J. Jeong, J.S. Lee, I.W. Kim and C.W. Ahn. *J. Eur. Ceram. Soc.* **34**, 29 (2014).
223. M. Habib, M. Munir, S.A. Khan, T.K. Song, M.H. Kim, M.J. Iqbal, I. Qazi and A. Hussain. *J. Phys. Chem. Solids* **138**, 109230 (2020).
224. X. Liu, B. Shen and J. Zhai. *J. Am. Ceram. Soc.* **102**, 6751 (2019).
225. Y. Si, Y. Li, L. Li, H. Li, Z. Zhao and Y. Dai. *J. Am. Ceram. Soc.* **103**, 1765 (2019).
226. P.Y. Chen, C.S. Chen, C.S. Tu, Y.S. Wu, W.S. Chang and S.H. Chen. *J. Alloys Compd.* **737**, 705 (2018).
227. T. Li, C. Liu, X. Ke, X. Liu, L. He, P. Shi, X. Ren, Y. Wang and X. Lou. *Acta Mater.* **182**, 39 (2020).
228. I.K. Hong, H.S. Han, C.H. Yoon, H.N. Ji, W.P. Tai and J.S. Lee. *J. Intell. Mater. Syst. Struct.* **24**, 1343 (2012).
229. Q. Wei, M. Zhu, M. Zheng and Y. Hou. *J. Alloys Compd.* **782**, 611 (2019).
230. T. Takenaka, H. Nagata and Y. Hiruma. *Jpn. J. Appl. Phys.* **47**, 3787 (2008).
231. L. Li, J. Hao, Z. Xu, W. Li and R. Chu. *J. Electron. Mater.* **47**, 1512 (2017).
232. P. Fan, Y. Zhang, Y. Zhu, W. Ma, K. Liu, X. He, M.A. Marwat, B. Xie, M. Li and H. Zhang. *J. Am. Ceram. Soc.* **102**, 4113 (2019).
233. H. Zhang, C. Groh, Q. Zhang, W. Jo, K.G. Webber and J. Rödel. *Adv. Electron. Mater.* **1**, 1500018 (2015).
234. Y. Zhang, P. Fan, H. Fan, B. Ye, G. Zhang, S. Jiang and H. Zhang. *J. Electroceram.* **44**, 32 (2020).
235. M. Sheeraz, A. Khaliq, A. Ullah, H.S. Han, A. Khan, A. Ullah, I.W. Kim, T.H. Kim and C.W. Ahn. *J. Eur. Ceram. Soc.* **39**, 4688 (2019).
236. H.S. Han, T.A. Duong, C.W. Ahn, W. Jo and J.S. Lee. *Ceramist* **23**, 89 (2020).
237. H.T.K. Nguyen, T.A. Duong, S.S. Lee, C.W. Ahn, H.-S. Han and J.-S. Lee. *Journal of Materials Research*, 1 (2020).
238. G.A. Smolenskii. *Sov. Phys.-Solid State* **2**, 2651 (1961).
239. H. He, X. Lu, M. Li, Y. Wang, Z. Li, Z. Lu and L. Lu. *J. Mater. Chem. C* **8**, 2411 (2020).
240. R. Cheng, Z. Xu, R. Chu, J. Hao, J. Du and G. Li. *J. Eur. Ceram. Soc.* **36**, 489 (2016).
241. C. Wang, T. Xia and X. Lou. *Ceram. Int.* **44**, 7378 (2018).
242. D.S. Yin, Z.H. Zhao, Y.J. Dai, Z. Zhao, X.W. Zhang, S.H. Wang and S. Zhang. *J. Am. Ceram. Soc.* **99**, 2354 (2016).
243. H.S. Han, N.B. Do, K.N. Pham, H.D. Jang, V.D.N. Tran, W.P. Tai and J.S. Lee. *Ferroelectrics* **421**, 88 (2011).
244. C.W. Tai, S.H. Choy and H.L.W. Chan. *J. Am. Ceram. Soc.* **91**, 3335 (2008).
245. C. Ciomaga, M. Viviani, M.T. Buscaglia, V. Buscaglia, L. Mitoseriu, A. Stancu and P. Nanni. *J. Eur. Ceram. Soc.* **27**, 4061 (2007).
246. S. Zixiong, P. Yongping and L. Yuwen. *J. Electron. Mater.* **43**, 1466 (2014).
247. T. Badapanda, S.K. Rout, L.S. Cavalcante, J.C. Sczancoski, S. Panigrahi, T.P. Sinha and E. Longo. *Mater. Chem. Phys.* **121**, 147 (2010).
248. F. Guo, W. Cai, R. Gao, C. Fu, G. Chen, X. Deng, Z. Wang and Q. Zhang. *J. Electron. Mater.* **48**, 3239 (2019).
249. H.L. Du, X. Du and H.L. Li. *Adv. Appl. Ceram.* **112**, 277 (2013).

250. J.U. Rahman, A. Hussain, A. Maqbool, T.K. Song, W.J. Kim, S.S. Kim and M.H. Kim. *Curr. Appl. Phys.* **14**, 331 (2014).
251. L. Gao, Y. Huang, Y. Hu and H. Du. *Ceram. Int.* **33**, 1041 (2007).
252. J.U. Rahman, A. Hussain, A. Maqbool, G.H. Ryu, T.K. Song, W.-J. Kim and M.H. Kim. *J. Alloys Compd.* **593**, 97 (2014).
253. A. Maqbool, A. Hussain, J. Ur Rahman, T. Kwon Song, W.-J. Kim, J. Lee and M.-H. Kim. *Ceram. Int.* **40**, 11905 (2014).
254. F. Li, R. Zuo, D. Zheng, L. Li and D. Viehland. *J. Am. Ceram. Soc.* **98**, 811 (2015).
255. S. Huband and P.A. Thomas. *J. Appl. Phys.* **121**, 184105 (2017).
256. M. Ullah, H. Ullah Khan, A. Ullah, A. Ullah, I.W. Kim, I. Qazi and I. Ahmad. *Ceram. Int.* **44**, 556 (2018).
257. W. Jo, T. Granzow, E. Aulbach, J. Rödel and D. Damjanovic. *J. Appl. Phys.* **105**, 094102 (2009).
258. N. Mostovych, S.S. Won, I.W. Kim, S.H. Kim and A.I. Kingon. *AIP Adv.* **10**, 045033 (2020).
259. N. Ullah Khan, A. Ullah, A. Ullah, M.Y. Khan, T.H. Kim, I.W. Kim and C.W. Ahn. *Sens. Actuator A-Phys.* **291**, 156 (2019).
260. V.D.N. Tran, A. Hussain, H.S. Han, T.H. Dinh, J.S. Lee, C.W. Ahn and I.W. Kim. *Jpn. J. Appl. Phys.* **51**, 09MD02 (2012).
261. K. Hao, W. Ge, Z. Ren, X. Liu, L. Luo, X. Li, H. Luo and D. Viehland. *J. Am. Ceram. Soc.* **103**, 3349 (2020).
262. C. Laulhé, A. Pasturel, F. Hippert and J. Kreisel. *Phys. Rev. B.* **82**, 132102 (2010).
263. I.K. Jeong, C.Y. Park, J.S. Ahn, S. Park and D.J. Kim. *Phys. Rev. B.* **81**, 214119 (2010).
264. M. Shen, W. Li, M.Y. Li, H. Liu, J. Xu, S. Qiu, G. Zhang, Z. Lu, H. Li and S. Jiang. *J. Eur. Ceram. Soc.* **39**, 1810 (2019).
265. J. Glaum, H. Simons, M. Acosta, M. Hoffman and A. Feteira. *J. Am. Ceram. Soc.* **96**, 2881 (2013).
266. P.-Y. Chen, C.-S. Chen, C.-S. Tu and T.-L. Chang. *J. Eur. Ceram. Soc.* **34**, 4223 (2014).
267. J. Glaum, M. Zakhosheva, M. Acosta, E. Aksel, H.-J. Kleebe, M. Hoffman, L.A. Schmitt and W. Jo. *J. Am. Ceram. Soc.* **99**, 2801 (2016).
268. A. Ullah, M. Ullah, A. Ullah, A. Ullah, G. Saddiq, B. Ullah, A. Zeb, S. Ullah Jan and I.W. Kim. *J. Korean Phys. Soc.* **74**, 589 (2019).
269. P.B. Groszewicz, H. Breitzke, W. Jo, J. Rödel and G. Buntkowsky. *J. Appl. Phys.* **121**, 114104 (2017).

List of Publications

Oral Presentations

- 1) 웬 호앙 티엔 코이, 딘 치 힌, 즈영 짱 안, 정광휘, 홍영환, 김일원, 이재신, “*Large low-field strain properties of $Bi_{0.5}Na_{0.5}TiO_3$ - $SrTiO_3$ ceramics with heterogeneity compositions*”, AMEC-10, 2016.12.04~12.07, GISTAPEI TECH Convention Center, Taiwan.
- 2) 웬 호앙 티엔 코이, 딘 치 힌, 즈영 짱 안, 정광휘, 홍영환, 김일원, 이재신, “*Effect of microscale heterogeneity on electromechanical strain properties of lead-free $(Bi_{1/2}Na_{1/2})TiO_3$ - $SrTiO_3$ ceramic composites*”, ICMFM 2017, 2017.05.08~05.10, Army Hotel, Vietnam.
- 3) 웬 호앙 티엔 코이, 이재신, 한형수, 김성현, 즈영짱 안, 에르키노프 파루크, “ *$(Bi,Na)TiO_3$ - $(Bi,K)TiO_3$ 계 강유전체 / 완화형 강유전체 복합세라믹스의 저전계 변형특성에 관한 연구*”, 2018 한국전기전자재료학회 하계학술대회, 2018.06.20~06.22, 대명 델피노리조트, 강원도 고성군.
- 4) 웬 호앙 티엔 코이, 이재신, 한형수, 김성현, 즈영짱 안, 에르키노프 파루크, “ *$(Bi,Na)TiO_3$ - $(Bi,K)TiO_3$ 계 강유전체 / 완화형 강유전체 복합세라믹스의 저전계 변형특성에 관한 연구*”, 2018 한국전기전자재료학회 하계학술대회, 2018.06.20~06.22, 대명 델피노리조트, 강원도 고성군.
- 5) 웬 호앙 티엔 코이, 즈영짱 안, 에르키노프 파루크, 이상훈, 한형수, 이재신, “*Effects of $CaTiO_3$ -modification on the dielectric and piezoelectric properties of the lead-free $(Bi_{1/2}Na_{1/2})TiO_3$ - $SrTiO_3$ piezoelectric ceramics*”, ICAE 2019, 2019.11.05~11.08, 라마다프라자 제주호텔, 제주도.

Journal Papers:

- 1) Guo Wang, Young Hwan Hong, **Hoang Thien Khoi Nguyen**, Byeong Woo Kim, Chang Won Ahn, Hyoung-Su Han, and Jae-Shin Lee, “*High electromechanical strain properties in $SrTiO_3$ -modified*

Bi_{1/2}Na_{1/2}TiO₃ lead-free piezoelectric ceramics under low electric field", Sensor and Actuators A: Physical, **293**, 1-6 (2019).

- 2) Trang An Duong, Hyoung-Su Han, Young-Hwan Hong, **Hoang Thien Khoi Nguyen**, Thi Hinh Dinh, and Jae-Shin Lee, "*Dielectric and piezoelectric properties of Bi_{1/2}Na_{1/2}TiO₃-SrTiO₃ lead-free ceramics*", Journal of Electroceramics, **41**, 73-79 (2018).
- 3) Thi Hinh Dinh, Jin-Kyu Kang, **Hoang Thien Khoi Nguyen**, Trang An Duong, Jae-Shin Lee, Vu Diem Ngoc Tran, and Ky Nam Pham, "*Giant strain in lead-free relaxor/ferroelectric piezocomposite ceramics*", Journal of the Korean Physical Society, **68** 1439-1444 (2016).
- 4) Sang-Hun Lee, Seong-Hyun Kim, Farrukh Erkinov, **Hoang Thien Khoi Nguyen**, Trang An Duong, Hyoung-Su Han, Jae-Shin Lee, "*Dielectric and piezoelectric properties of microwave sintered BNT-ST ceramics*," Journal of the Korean Institute of Electrical and Electronic Material Engineers, Vol. 33(1), 37-44 (2020).
- 5) **Hoang Thien Khoi Nguyen**, Trang An Duong, Farrukh Erkinov, Hyungwon Kang, Byeong Woo Kim, Chang Won Ahn, Hyoung-Su Han, and Jae-Shin Lee, "*Effect of SrTiO₃ modification on dielectric, phase transition and piezoelectric properties of lead-free Bi_{0.5}Na_{0.5}TiO₃-CaTiO₃-SrTiO₃ piezoelectric ceramics*", Journal of the Korean Ceramic Society, Vol. 57, 570-577 (2020).
- 6) **Hoang Thien Khoi Nguyen**, Trang An Duong, Farrukh Erkinov, Chang Won Ahn, Byeong Woo Kim, Hyoung-Su Han, Jae-Shin Lee, "*Large Electric Field-Induced Strain Response Under a Low Electric Field in Lead-Free Bi_{1/2}Na_{1/2}TiO₃-SrTiO₃-BiAlO₃ Ternary Piezoelectric Ceramics*" Journal of Electronic Materials, Vol. 49(11), 6677-6685 (2020).
- 7) **Hoang Thien Khoi Nguyen**, Trang An Duong, Sang Sub Lee, Chang Won Ahn, Hyoung-Su Han, Jae-Shin Lee, "*Comparing the electromechanical properties of CaTiO₃-and BaZrO₃-modified Bi_{0.5}Na_{0.5}TiO₃-SrTiO₃ ceramics*," Journal of Materials Research, Online published 2020.

Patents

- 1) Lead-free piezoelectric ceramic ternary compositions with high strains, Kor. Patent Application No. 10-2017-0064310 (2017).
- 2) Production method of lead-free piezoelectric ceramics with high strains, Kor. Patent Application No. 10-2016-0082892 (2016)

Awards

- 1) **The International Conference on Materials Engineering and Functional Materials (ICMFM), Best presentations, May 8-10, 2017**
- 2) **KIEEME Annual Summer Conference 2020, 우수 논문상, July 8-10, 2020**